"I firmly believe that in any man's finest hour, the greatest fulfillment of all that he holds dear, is the moment when he has worked his heart out in a good cause and lies exhausted on the field of battle-victorious."

Vince Lombardi

University of Alberta

Development and Characterization of Interfacial Chemistry for Biomolecule Immobilization in Surface Plasmon Resonance (SPR) Imaging Studies

by

Christopher Francis Grant

A thesis submitted to the Faculty of Graduate Studies and Research
in partial fulfillment of the requirements for the degree of

Doctor of Philosophy

Department of Chemistry

Fall 2009
Edmonton, Alberta

Examining Committee

Dr. Mark T. McDermott, Chemistry

Dr. D. Jed Harrison, Chemistry

Dr. Dennis G. Hall, Chemistry

Dr. Robert E. Campbell, Chemistry

Dr. Warren J. Gallin, Biological Sciences

Dr. C. Roger MacKenzie, External Examiner, Department of Environmental Biology, University of Guelph and Institute for Biological Sciences, National Research Council

Abstract

Surface immobilization of probe molecules in surface based assays is a key area of research in the continued development of immunoassay microarrays. Interest continues to grow in microarray based immunoassays given their potential as a high throughput technique for immunodiagnostics. Therefore, it is important to thoroughly study and understand the implications of interfacial chemistry and immobilization conditions on the performance of the assay. This thesis presents a body of work that examines the impact of probe density, interfacial chemistry, and enhancement factors for arrays read with surface plasmon resonance (SPR) imaging.

An array of structurally similar Salmonella disaccharides was immobilized at varying densities and the interface formed was thoroughly investigated to determine the properties of the interface. The arrays were then used with SPR imaging to evaluate the binding of an antibody specific for one disaccharide of the three stereoisomers on the array. A dilute disaccharide surface was found to provide optimal antibody binding. Higher densities result in steric hindrance of antibody binding by not allowing the disaccharide to insert into the antibody binding pocket.

The role of interfacial chemistry in antibody attachment was studied to determine optimum conditions. The study examined physical adsorption, covalent attachment, and affinity capture. It was found that covalent attachment provided the most stable attachment and resulted in the lowest levels of antigen detection. Both the physical adsorption and affinity capture provided larger

antigen binding capacity and therefore more sensitive antigen detection. The covalent attachment was chosen to evaluate an enhanced assay with the incorporation of gold nanoparticles. These particles provided detection limits that were an order of magnitude improved over those excluding the nanoparticles.

A novel surface chemistry for antibody immobilization in SPR imaging studies was evaluated. This involved the electrochemical driven formation of mono- to multilayers of diazonium benzoic acid films. The studies showed the ability to control the thickness of the films formed and also the ability of the antibody chips to capture antigen from solution.

Table of Contents

Chapter 1: Introduction

Chapter 2: Optimization of Immobilized Bacterial Disaccharides for Surface Plasmon Resonance (SPR) Imaging Measurements of Antibody Binding

Chapter 3: Tailoring Interfacial Chemistry for Antibody Immobilization in Surface Plasmon Resonance (SPR) Imaging Immunoassays

Chapter 4: Enhanced Surface Plasmon Resonance (SPR) Imaging using Modified Gold Nanoparticles and a Sandwich Immunoassay

Chapter 5: Mono- and Multilayered Aryl Films for Surface Plasmon Resonance (SPR) Imaging Studies

Chapter 6: Conclusions and Future Work

List of Tables

List of Figures

List of Abbreviations

ACSES	Alberta Center for Surface and Engineering Sciences
AET	2-Aminoethanethiol
AFM	Atomic Force Microscopy
a-bIgG	Anti-bovine Immunoglobulin G
a-gIgG	Anti-goat Immunoglobulin G
a-rIgG	Anti-rabbit Immunoglobulin G
AUT	11-Amino-1-undecanethiol
bIgG	Bovine Immunoglobulin G
BSA	Bovine Serum Albumin
Bu_4NBF_4	Tetrabutylammonium Tetrafluoroborate
CDRs	Complimentary Determining Regions
CV	Cyclic Voltammogram
DSNB	5,5’-Dithiobis(succinimidyl-2-nitrobenzoate)
dzBA	Benzoic Acid Diazonium Salt
EDC	N-(3-dimethylaminopropyl)-N’-ethylcarbodiimide hydrochloride
EIA	Enzyme Immunoassay
ELISA	Enzyme Linked Immunosorbent Assay
EQCM	Electrochemical Quartz Crystal Microbalance
FAT	Fixed Analyser Transmission
FDA	Food and Drug Administration

gIgG	Goat Immunoglobulin G
HIV	Human Immunodeficiency Virus
ICP-MS	Inductively Coupled Plasma – Mass Spectrometry
Ig	Immunoglobulin
IRRAS	Infrared Reflection Absorption Spectroscopy
LAT	Latex Agglutination Test
LOD	Limit of Detection
LPS	Lipopolysaccharide
MAQC	Microarray Quality Control
4-MBA	4-Mercaptobenzoic acid
MUA	11-Mercapto-undecanoic acid
MUO	11-Mercaptoundecanol
NHS	N-hydroxysuccinimide
NP(s)	Nanoparticle(s)
NTA	Nitriliotriacetic
PBS	Phosphate Buffered Saline
PBST	Phosphate Buffered Saline + Tween
PDMS	Poly(dimethylsiloxane)
PE	Pass Energy
PEG	Polyethylene Glycol
PWHM	Peak Width at Half Maximum
RBC	Red Blood Cell
Rh	Rhesus Factor

rIgG	Rabbit Immunoglobulin G
RU	Resonance Units
SAM	Self-Assembled Monolayer
SEM	Scanning Electron Microscopy
SFM	Scanning Force Microscopy
SPM	Scanning Probe Microscopy
SPR	Surface Plasmon Resonance
STM	Scanning Tunneling Microscopy
WHO	World Health Organization
XPS	X-ray Photoelectron Spectroscopy

List of Symbols

c	Speed of light in a vacuum
%R	Percent reflectivity
$\Delta\%R$	Change in percent reflectivity
$\Delta\%R_{min}$	Asymptotic minimum change in percent reflectivity
$\Delta\%R_{max}$	Asymptotic maximum change in percent reflectivity
b	Hill coefficient
K_a	Association constant
K_d	Dissociation constant
K_{ADS}	Adsorption constant
eV	Electron Volts
W	Watts
R^2	Correlation coefficient
$E_{p,c}$	Cathodic peak potential
$\nu_{C=O}$	Carbonyl stretch
$\nu_{a,CH2}$	Asymmetric methylene stretch
χ	Mole fraction
σ	Standard deviation
θ	Fraction coverage
ω	Angular frequency
ε_m	Dielectric constant of the metal
ε_d	Dielectric constant of the dielectric material

ε_p	Dielectric constant of the prism
k_{photon}	Wave vector of a photon
k_{ATR}	Wave vector of a photon of light totally internally reflected
k_{sp}	Wave vector of a surface plasmon wave

Chapter 1:

Introduction

1.1 SOLID-PHASE ASSAYS

Initially met with resistance from those involved in the more traditional field of solution-based assays, the extension of immunoassays to a heterogeneous format and the incorporation of a solid-phase has gained significant acceptance over the last 40 years. The development of a solid phase assay was partially born out of necessity when an immunosorbent surface was used in enzyme immunoassays (EIA). The surface immobilization of an analyte allowed the incorporation of wash steps required to separate bound from unbound enzyme label, allowing for specific detection.[1-3]

A common challenge when developing surface assays is not the mere adsorption of an antibody or antigen to a surface, as proteins are intrinsically surface-active molecules.[4-8] The challenge is to control the adsorption such that structural integrity and binding activity is retained. Surface adsorption can be viewed as a collection of events, including diffusion to the interface followed by adsorption and potentially structural rearrangement. The structural rearrangement may range from partial to complete denaturing of the protein.[4,7,9] The process is depicted in Figure 1.01. Immunoassays involve the use of an antibody as an analytical reagent to quantitate the presence of antigen. The term antibody refers to a family of blood plasma proteins called immunoglobulins (Ig) and consists of IgG, IgM, IgA, IgE, and IgD. Of these proteins IgG, shown in Figure 1.02, is the most abundant of circulating antibodies and is composed of two 50 kDa heavy chains consisting of four homologous domains and two 25 kDa light chains consisting of two homologous domains. The base of the antibody, known as the fragment crystallizable (F_c), is constant for all antibodies of a given class. The antigen binding fragments (F_{ab}) are composed of a constant heavy and constant light domain, as well as a variable heavy and variable light domain. The variable fragments (F_v) are located at the N-terminal domains of the heavy and light chains, the domains at the outermost part of the arms of the antibody. These variable domains provide antigenic specificity with antigen binding occurring in the complementary determining regions (CDRs). The CDRs are formed from six hypervariable loops that form a single surface at the terminus of each arm. The regions are composed equally of 3 hypervariable loops from the variable heavy and light chains present in both arms of the antibody.[10,11]

The second most common protein used in this work is bovine serum albumin (BSA). BSA is one of the most abundant blood plasma proteins. It is a 66 kDa protein composed of a single polypeptide chain, 583 amino acids in length. BSA has been described as a heart shaped molecule, with an approximate size of 8 x 8 x 3.8 nm.[12,13] BSA is a commonly used protein with applications as a nutrient in cell and microbial cultures, as a stabilizer for enzymes during DNA digestion, and as a blocking agent.[14] The prominent use of this protein is related to its stability, minimal interference in biochemical reactions, and low cost to produce, as it may be extracted from bovine serum, a by product of the cattle industry. In this work BSA will be used as a surface passivation or blocking agent to minimize and monitor the non-specific adsorption of IgG molecules.

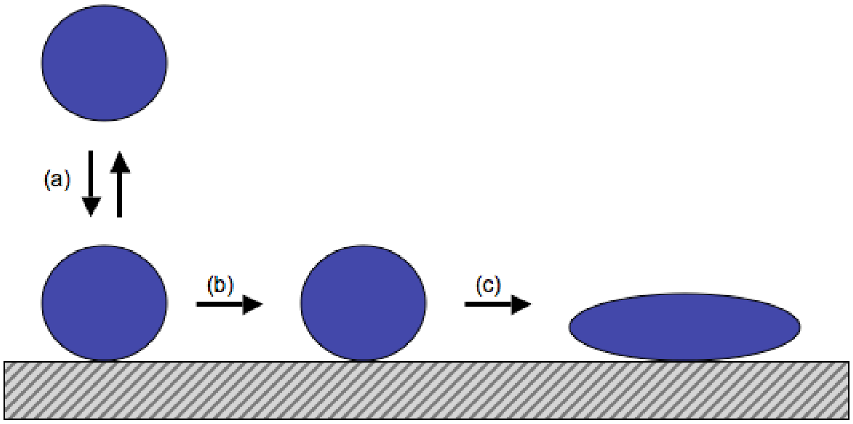

Figure 1.01. Schematic of the proposed mechanism for the surface adsorption of proteins including (a) reversible adsorption, (b) irreversible adsorption, (c) structural rearrangement.

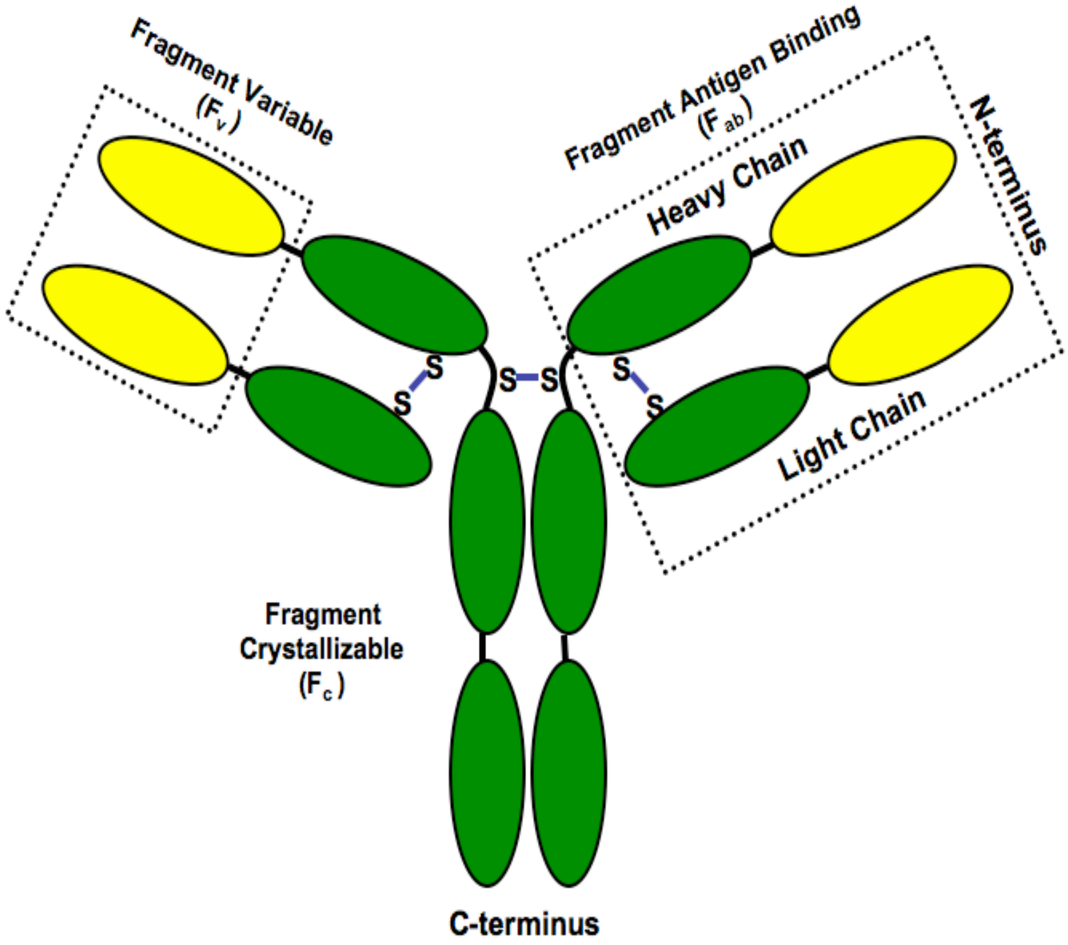

Figure 1.02. Structure for an Immunoglobulin G molecule showing the twelve domains of the structure. The constant domains are presented in green and the variable domains are shown in yellow. The four chains of the IgG are attached through the sulfide bonds (S-S).

1.2 INTERFACIAL CHEMISTRY

The modification of a gold surface with an alkanethiolate can be summarized by reaction 1 below. The first published report for the self-assembly of a monomolecular film on a metal surface dates back over 60 years.[15] However, the potential of this work was not realized until some 40 years later by Nuzzo and Allara who published the first of many papers on the self-assembly of alkanethiolates on gold.[16] Since that time there have been great research efforts examining this substrate-adsorbate system.[16-25]

$$R\text{-}(CH_2)_n\text{-}SH + Au \longrightarrow R\text{-}(CH_2)_n\text{-}S^-Au^+ + \tfrac{1}{2} H_2 \qquad (1)$$

The adsorption of alkanethiolates has been shown to proceed by two distinct steps, as presented in Figure 1.03.[17,18] The first is diffusion limited Langmuir adsorption governed by the surface-head group interaction. This produces a disorganized layer with a surface coverage near 80-90% of its final value and is complete in about 1 minute for 10^{-3} M solutions. The second step, known as surface crystallization, is a slower step taking several hours. In this step, the alkanethiolate chains move from a disordered state into organized unit cells forming two-dimensional crystals. For adsorbates with alkyl chains of $n>9$ the structure of the resulting monolayer has been shown to be crystalline, while shorter chains tend to form a more liquid like layer, due to limited Van der Waals interactions that drive the surface crystallization reaction.[24] The spontaneous nature of these two processes leads to the term self-assembled monolayer (SAM), the commonly used abbreviation associated with this adsorbate-substrate combination.

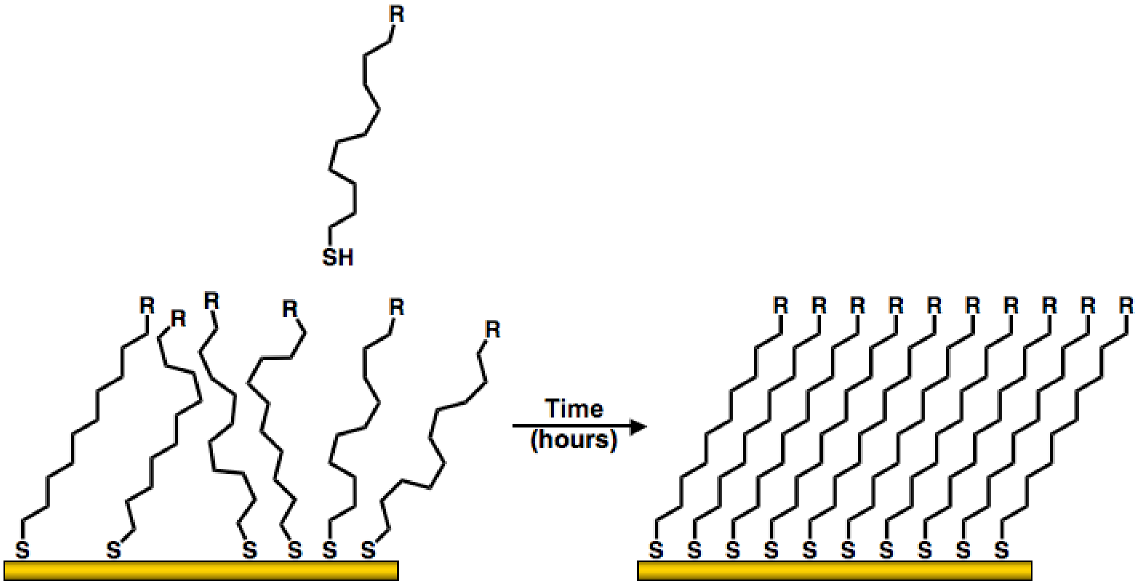

Figure 1.03. Self-assembly of an alkanethiolate monolayer on a gold surface showing initial adsorption followed by the reorganization and crystallization of the SAM.

The self-assembly of alkanethiolates on gold has been widely used to manipulate interfacial chemistry owing to the well studied and characterized monolayer produced by this adsorbate-substrate combination.[16,19-21,23-26] The availability of alkanethiolates with numerous terminal functional groups permits the formation of well-ordered interfaces with a defined chemistry that has been used to study the interfacial chemistry of protein adsorption.[27,28] In addition to monomolecular SAMs, the composition and structure of two-component mixed monolayers derived from thiols on gold have been explored in a number of studies.[26,29-34] The systems studied have been primarily a mixture of two n-alkanethiols of different length[26,29,32] and an n-alkanethiol mixed with an alkyl thiol terminated in a simple functional group (e.g., -CH_2OH, COOH, -CH_2Br, -CH_2CN).[31,35] It has been shown that the mole fraction of one component on the surface is related to its mole fraction in solution.[31,33,35] The trends have followed both linear and non-linear profiles and in general, the composition of the monolayer is not equivalent to the composition in solution. The formation of mixed SAMs provides greater flexibility in tuning interfacial chemistry, and they have been used to control the density of surface attached molecules.[36]

While SAMs of alkanethiolates on gold have proven useful, they are typically limited to a monolayer of coverage. Applications such as the fabrication of sensor surfaces may benefit from a multilayered surface presenting a larger number of functional groups to the interface. Provided these additional functional groups are accessible to biomolecules in solution, these multilayered surfaces may immobilize greater densities of target, increasing the binding capacity of the surface. Other potential benefits of alternatives to SAMs, include the advantage of possibly stronger adsorbate-substrate interactions, producing a more stable surface modification.

The electrochemical reduction of diazonium salts has been shown to form stronger adsorbate-substrate structures relative to SAMs of alkanethiolates.[37-40] The chemistry involves the reductive adsorption of diazonium salts in a one-electron reduction of the diazonium, producing an aryl radical.[41,42] This radical is then chemically grafted to the electrode surface. Under appropriate conditions it is believed that the radical may further attack the aromatic ring of other aryl molecules, producing a multilayered structure. The process is represented in Figure 1.04.

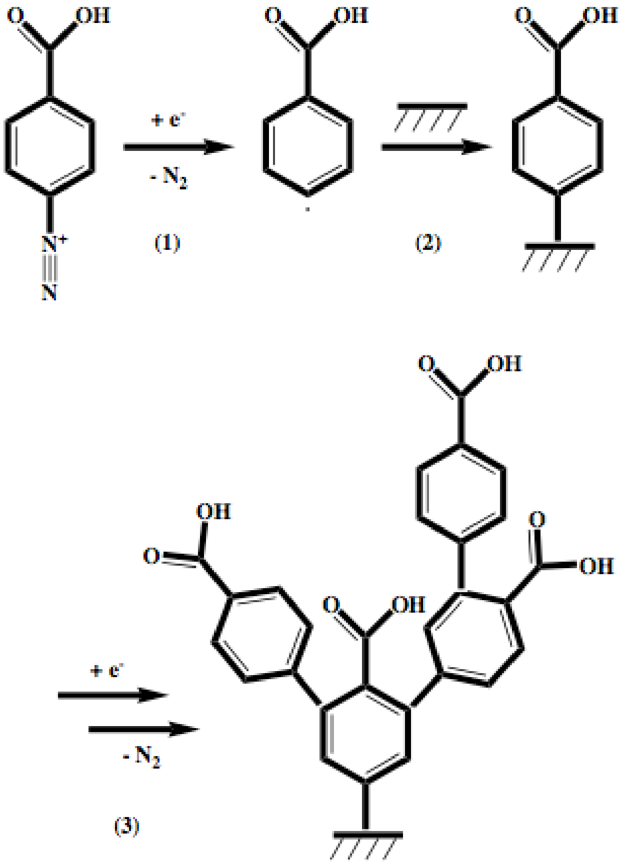

Figure 1.04. Electrochemical reduction of an aryl diazonium salt (1) followed by grafting to the electrode surface (2) and further reaction of the aryl radicals with surface bound molecules to produce multilayered surfaces (3).

1.3 MICROARRAYS

A microarray describes an ordered array of spots on a micro scale, where spots are typically several hundred microns in diameter or smaller.[43] These arrays may be composed of tens of thousands of spots where each spot contains a specific molecule of interest. The first microarrays began to appear in the early to mid-1990's in conjunction with the push to reveal the human genome.[44] The reasonable success of this tool to simultaneously analyze thousands of interactions with minimal sample consumption led to researchers expanding this technique to other applications, specifically proteomics.[45-47] The extreme growth is witnessed by a simple search of an electronic database, which provides 26,307 hits for research articles involving microarray technology.[48]

The ability to create these arrays requires the ability to produce a pattern of biomolecules on the surface. In the high-throughput arrays mentioned above this would involve the robotic spotting of molecules on an activated surface. The substrate contains an 'activated' chemistry to promote immobilization of the spotted molecule. Common examples include amine or aldehyde 'activated' surfaces. While robotic spotters have proven useful for the production of high-density arrays they are typically employed only for the immobilization of a probe molecule to an unpatterned 'activated' surface. For the work presented herein, it was necessary to pattern both surface chemistry and biomolecules.

The methods used to pattern thiols on gold include microcontact printing,[49] optical lithography,[50] microfluidics,[51,52] and more recently a pipet method. The methods employed for this work involve the use of microfluidics and the development of a pipet method. Microfluidic channels are fabricated by casting polydimethylsiloxane against a negative relief master containing raised rectangular features that define the dimensions of the fluidic channels. The PDMS is removed and sealed by conformal contact to the array surface, creating the fourth wall of the channel. As shown in Figure 1.05, the solutions may then be drawn through under vacuum and allowed to incubate with the surface. A distinct advantage of this technique, relative to the robotic spotters mentioned above, is the ability to reduce the stress on the biomolecules by limiting the drying of the proteins and exposure to the liquid-air interface. Of note, there has also been considerable progress made with the development of PDMS microfluidic spotters that are capable of producing higher density arrays than those initially available.[53]

Another method used in my work employs a common laboratory handheld micropipette to pattern the surface. To achieve patterning the surface must first be modified such that there are both hydrophobic and hydrophilic regions. The solutions are spotted in the hydrophilic regions and remain confined due to the unwillingness of the droplet to expand into the hydrophobic region. Creation of an array composed of hydrophobic and hydrophilic regions for this purpose has been achieved through microcontact printing of methyl terminated alkanethiolates on gold, leaving unpatterned patches of hydrophilic gold.[54,55] Shown in Figure 1.06 is a second approach to surface patterning, that I was involved in developing in our lab. This method involves the creation of an array of gold spots on a modified glass surface. Thin film deposition of the metal layer is performed through a shadow mask producing a pattern of gold spots. The glass is then rendered hydrophobic with a fluorinated silane, which provides the ability to confine solutions to the gold spots. Surfaces have been made consisting of nine, nineteen, and forty-one spots with diameters as small as 500 μm.

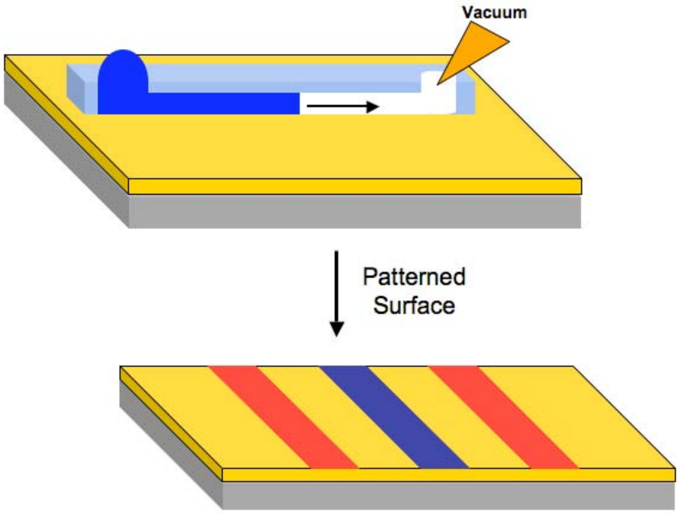

Figure 1.05. Surface patterning using PDMS microfluidic channels. The top image is a cut-away showing a vertical cross-section through a microfluidic channel in the PDMS. The solutions are delivered via pipette to the inlet hole and then drawn through the channel by applying a vacuum to the outlet port. Bottom image represents a typical patterned surface, with colors representing different surface chemistry or target molecules.

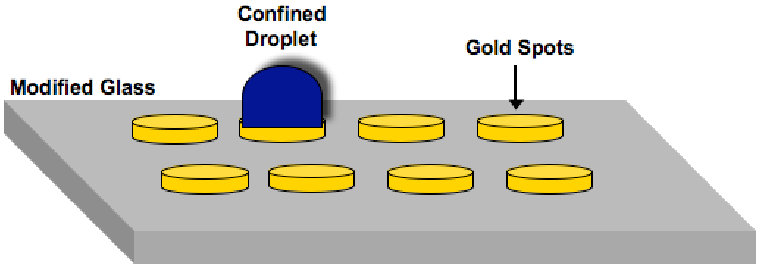

Figure 1.06. An SPR chip with an array of gold spots separated by glass that has been rendered hydrophobic by reaction with a fluorinated silane. Solutions are delivered to the spots using a handheld micropipette.

1.4 SURFACE PLASMON RESONANCE (SPR) IMAGING

Detection in immunoassays has relied heavily on the incorporation of labeled reagents. The first immunoassay, developed in 1959 by Berson and Yalow, involved the use of radio-labeled insulin in a competitive immunoassay.[56] The hazardous nature of these labels resulted in a shift towards enzymes, and more recently fluorescent tags. Today fluorescence remains the dominant method of detection for high-throughput arrays due to its ability to provide sensitive detection. However, interest continues to grow as progress is made developing technology capable of providing sensitive detection while alleviating the requirement of labeled reagents.

The label-free format of SPR has resulted in its significant growth as a tool for monitoring biomolecular interactions occurring at a metal-dielectric interface.[51,57-69] A surface plasmon is a quasi-free longitudinal electron density that propagates along a metal-dielectric interface and decays exponentially into the adjacent medium.[70] The excitation of this surface wave requires the wave vector of a photon of light to be lengthened to satisfy momentum-matching conditions. This may be accomplished by using prism-coupling or a grating. Today, the most common technique is the use of prism-coupling in what is referred to as the Kretschmann configuration. In this set-up a thin metal film is placed in contact with a prism and p-polarized light is directed through the prism and attenuated total reflection occurs at the prism/metal interface. Equations 2-4 below represent the wave vectors of a photon of light (k_{photon}), a surface plasmon wave (k_{SP}), and a photon of light totally internally reflected at the prism/metal interface (k_{ATR}). Here ω is the angular frequency, c is the speed of light in a vacuum, θ is the angle of incidence and ε_m, ε_d, and ε_p are the dielectric constants of the metal, dielectric, and prism respectively.[64]

$$k_{photon} = \frac{\omega}{c} \tag{2}$$

$$k_{sp} = \frac{\omega}{c}\sqrt{\frac{\varepsilon_m \varepsilon_d}{\varepsilon_m + \varepsilon_d}} \tag{3}$$

$$k_{ATR} = \frac{\omega}{c}\sin\theta\sqrt{\varepsilon_p} \tag{4}$$

The wave vector equation of the totally internally reflected photon (k_{ATR}) may be tuned to match that of the surface plasmon by adjusting the wavelength or angle of incident light. When conditions are such that $k_{ATR} = k_{SP}$ they are in resonance, which may be observed as a minimum in reflected intensity of the incident photons. This is represented graphically in Figure 1.07 where the reflected intensity is shown as a function of the angle of incident light. When conditions are such that resonance occurs there is a minimum in reflected intensity, known as the SPR angle.

SPR as a detection technology relies on the relation between the propagation constant of the wave vector of the surface plasmon and the dielectric constant of the adjacent medium (ε_d). As mentioned briefly above, the surface plasmons are evanescent waves that decay exponentially into the dielectric medium several hundred nanometers, with the absolute penetration depth depending on the wavelength of light used.[69,70] Therefore, changes in the refractive index of the dielectric medium directly adjacent to the metal film alter k_{SP} and the conditions required to generate resonance. There have been several approaches to monitor these changes and they include scanning angle, scanning wavelength, and imaging (constant wavelength and angle) instruments. As the name suggests, in the scanning systems the angle or wavelength of the incident light is scanned to determine the conditions required to restore resonance and determine the SPR angle. In an imaging system the incident wavelength and angle are fixed and the change in reflected intensity is observed. Figure 1.07 demonstrates an initial SPR curve (blue) and that following surface adsorption (green). As material adsorbs to the surface the SPR curve shifts to the right and an increase in reflected intensity is observed as the resonance between the surface plasmon and the incident light are reduced.

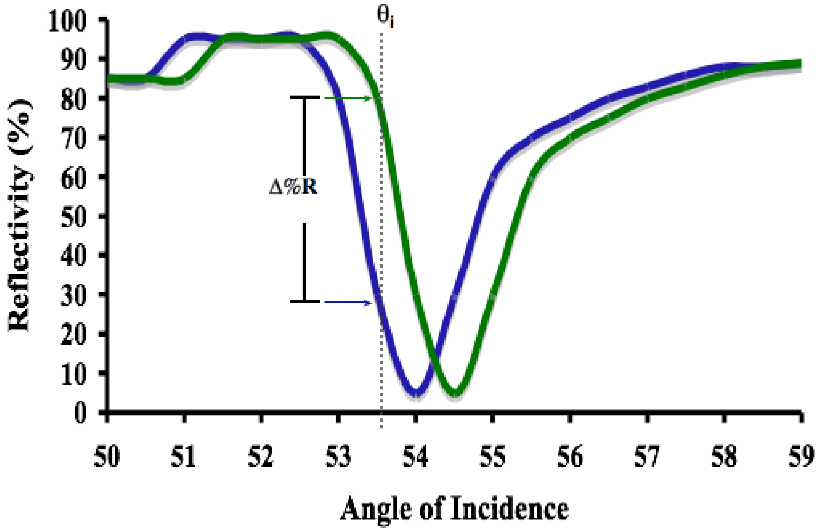

Figure 1.07. A reflectivity plot showing the change in observed reflectivity from a prism/metal interface for a p-polarized light source as a function of angle of incidence. The blue trace represents an initial SPR curve, and the green trace shows the shift following adsorption at the metal surface.

The experimental set-up for the SPR imaging system used in this work is shown in Figure 1.08. Here collimated white light is passed through a polarizer and then reflected from a prism/metal interface. The reflected light is passed through a narrow band-pass filter and the change in intensity of light at 814 nm is detected with a CCD detector.

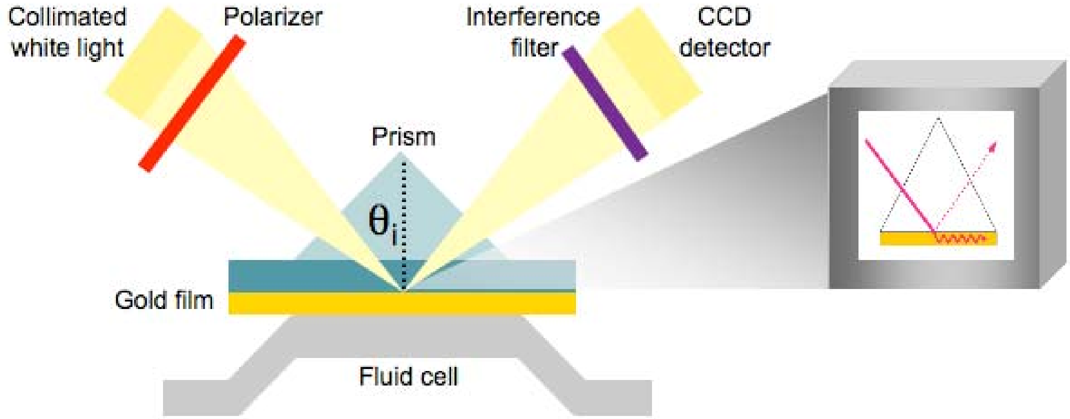

Figure 1.08. Instrumental layout for an SPR imaging system with the highlight to the right showing the resonance between the incident light and the surface plasmons.

1.5 RESEARCH OBJECTIVES

The main objective of this work was to improve performance of surface based immunoassays, including SPR imaging studies. The overall objective may subdivided into several related projects. The behavior of antibodies at the solid-liquid interface is an important aspect that determines the performance of the assay. The first half of the work, presented in Chapters 2 and 3, was designed to examine the role of interfacial chemistry on antibody binding. The variables studied included the role of target density on antibody binding, as well as the impact of surface chemistry on antibody immobilization, and assay performance. The objective of the second half of the work, Chapters 4 and 5, focused on enhancing the detection limits of SPR immunoasssys. The enhancements examined included, the use of a sandwich immunoassay, incorporation of dense gold nanoparticles, and the evaluation of a new surface chemistry for SPR imaging.

1.6 REFERENCES

(1) Van Weemen, B. K.; Schuurs, A. H. *FEBS Letters* **1971**, *15*, 232-236.

(2) Engvall, E.; Perlman, P. *Immunochemistry* **1971**, *8*, 871-874.

(3) Wide, L.; Porath, J. *Biochem. Biophys. Acta.* **1966**, *30*, 257.

(4) Gray, J. J. *Curr. Opin. Struct. Biol.* **2004**, *14*, 110-115.

(5) Losche, M. *Curr. Opin. Biotechnol.* **1997**, *2*, 546-556.

(6) Hlady, V.; Buijs, J. *Curr. Opin. Biotechnol.* **1996**, *7*, 72-77.

(7) Ramsden, J. J. *Chem. Soc. Rev.* **1995**, *24*, 73-78.

(8) Haynes, C. A.; Norde, W. *Colloids and Surfaces B: Biointerfaces* **1994**, *2*, 517-566.

(9) Fang, F.; Szleifer, I. *Biophys. J.* **2001**, *80*, 2568-2589.

(10) Huber, R.; Deisenhofer, J.; Colman, P. M.; Matsushima, M.; Palm, W. *Nature* **1976**, *264*, 415-420.

(11) Amzel, L. M.; Poljak, R. J. *Annu. Rev. Biochem.* **1979**, *48*, 961-997.

(12) Putnam, F. W. *The Plasma Proteins: Structure, Function and Genetic Control*; Second ed.; Academic Press: New York, 1975.

(13) Yampolskaya, G.; Platikanov, D. *Adv. Colloid Interface Sci.* **2006**, *128*, 159-183.

(14) Sigma Product Information **2000**.

(15) Bigelow, W. C.; Pickett, D. L.; Zisman, W. A. *J. Colloid Interface Sci.* **1946**, *1*, 513.

(16) Nuzzo, R. G.; Allara, D. L. *J. Am. Chem. Soc.* **1983**, *105*, 4481-4483.

(17) Ulman, A. *Chem. Rev.* **1996**, *96*, 1533-1554.

(18) Dubois, L. H.; Nuzzo, R. G. *Annu. Rev. Phys. Chem.* **1992**, *43*, 437-463.

(19) Nuzzo, R. G.; Dubois, L. H.; Allara, D. L. *J. Am. Chem. Soc.* **1990**, *112*, 558-569.

(20) Bain, C. D.; Whitesides, G. M. *Langmuir* **1989**, *5*, 1370-1378.

(21) Bain, C. D.; Troughton, E. B.; Tao, Y. T.; Evall, J.; Whitesides, G. M.; Nuzzo, R. G. *J. Am. Chem. Soc.* **1989**, *111*, 321-335.

(22) Bain, C. D.; Biebuyck, H. A.; Whitesides, G. M. *Langmuir* **1989**, *5.*

(23) Bain, C. D.; Whitesides, G. M. *J. Am. Chem. Soc.* **1988**, *110*, 3665-3666.

(24) Porter, M. D.; Bright, T. B.; Allara, D. L.; Chidsey, C. E. D. *J. Am. Chem. Soc.* **1987**, *109*, 3559-3568.

(25) Nuzzo, R. G.; Fusco, F. A.; Allara, D. L. *J. Am. Chem. Soc.* **1987**, *109*, 2358-2368.

(26) Bain, C. D.; Whitesides, G. M. *J. Am. Chem. Soc.* **1989**, *111*, 7164-7175.

(27) Ta, T. C.; McDermott, M. T. *Anal. Chem.* **2000**, *72*, 2627-2634.

(28) Prime, K. L.; Whitesides, G. M. *Science* **1991**, *252*, 1164-1167.

(29) Stranick, S. J.; Parikh, A. N.; Tao, Y.-T.; Allara, D. L.; Weiss, P. S. *J. Phys. Chem.* **1994**, *98*, 7636-7646.

(30) Spinke, J.; Liley, M.; Guder, H. J.; Angermaier, L.; Knoll, W. *Langmuir* **1993**, *9*, 1821-1825.

(31) Bertilsson, L.; Liedberg, B. *Langmuir* **1993**, *9*, 141-149.

(32) Laibinis, P. E.; Nuzzo, R. G.; Whitesides, G. M. *J. Phys. Chem.* **1992**, *96*, 5097-5105.

(33) Folkers, J. P.; Laibinis, P. E.; Whitesides, G. M. *Langmuir* **1992**, *8*, 1330-1341.

(34) Ulman, A.; Evans, S. D.; Shnidman, Y.; Sharma, R.; Eilers, J. E.; Chang, J. C. *J. Am. Chem. Soc.* **1991**, *113*, 1499-1506.

(35) Bain, C. D.; Evall, J.; Whitesides, G. M. *J. Am. Chem. Soc.* **1989**, *111*, 7155-7164.

(36) Houseman, B. T.; Mrksich, M. *Chem. Biol.* **2002**, *9*, 443-454.

(37) Laforgue, A.; Addou, T.; Belanger, D. *Langmuir* **2005**, *21*, 6855-6865.

(38) Brooksby, P. A.; Downard, A. J. *J. Phys. Chem. B* **2005**, *109*, 8791-8798.

(39) Anariba, F.; DuVall, S. H.; McCreery, R. L. *Anal. Chem.* **2003**, *75*, 3837-3844.

(40) Kariuki, J. K.; McDermott, M. T. *Langmuir* **2001**, *17*, 5947-5951.

(41) Allongue, P.; Delamar, M.; Desbat, B.; Fagebaume, O.; Hitmi, R.; Pinson, J.; Saveant, J. M. *J. Am. Chem. Soc.* **1997**, *119*, 201-207.

(42) Delamar, M.; Hitmi, R.; Pinson, J.; Saveant, J. M. *J. Am. Chem. Soc.* **1992**, *114*, 5883-5884.

(43) Schena, M. *Microarray Analysis*; Wiley-Liss: Hoboken, 2003.

(44) Schena, M.; Shalon, D.; Davis, R. W.; Brown, P. O. *Science* **1995**, *270*, 467.

(45) Krska, R.; Janotta, M. *Anal. Bioanal. Chem.* **2004**, *379*, 338-340.

(46) Zu, Q.; Lam, K. S. *J. Biomed. Biotechnol.* **2003**, *5*, 257-266.

(47) Templin, M. F.; Stoll, D.; Schrenk, M.; Traub, P. C.; Vohringer, C.; Joos, T. O. *Drug Discov. Today* **2002**.

(48) 11/02/2008, Web of Science

(49) Wilbur, J. L.; Kumar, A.; Kim, E.; Whitesides, G. M. *Adv. Mater.* **1994**, *6*, 600-604.

(50) Jordan, C. E.; Corn, R. M. *Anal. Chem.* **1997**, *69*, 1449-1456.

(51) Kanda, V.; Kariuki, J. K.; Harrison, D. J.; McDermott, M. T. *Anal. Chem.* **2004**, *76*, 7257-7262.

(52) Lee, H. J.; Goodrich, T. T.; Corn, R. M. *Anal. Chem.* **2001**, *73*, 5525-5531.

(53) Flaim, E. PhD, University of Alberta, 2008.

(54) Narayanan, R.; Lipert, R. J.; Porter, M. D. *Anal. Chem.* **2008**, *80*, 2265-2271.

(55) Driskell, J. D.; Kwarta, K. M.; Lipert, R. J.; Porter, M. D.; Neill, J. D.; Ridpath, J. F. *Anal. Chem.* **2005**, *77*, 6147-6154.

(56) Yaslow, R. S.; Berson, S. A. *Nature* **1959**, *184*, 1648-1649.

(57) Wang, J. L.; Lv, R. J.; Xu, J. J.; Xu, D. K.; Chen, H. Y. *Anal. Bioanal. Chem.* **2008**, *390*, 1059-1065.

(58) Taylor, A. D.; Ladd, J.; Etheridge, S.; Deeds, J.; Hall, S.; Jiang, S. Y. *Sensors Actuator B Chem.* **2008**, *130*, 120-128.

(59) Shang, H. PhD, University of Alberta, 2008.

(60) Martin, V. S.; Sullivan, B. A.; Walker, K.; Hawk, H.; Sullivan, B. P.; Noe, L. J. *Appl. Spectros.* **2006**, *60*, 994-1003.

(61) Kanda, V.; Kitov, P.; Bundle, D. R.; McDermott, M. T. *Anal. Chem.* **2005**, *77*, 7497-7504.

(62) Steiner, G. *Anal. Bioanal. Chem.* **2004**, *379*, 328-331.

(63) Smith, E. A.; Thomas, W. D.; Kiessling, L. L.; Corn, R. M. *J. Am. Chem. Soc.* **2003**, *125*, 6140-6148.

(64) Smith, E. A.; Corn, R. M. *Appl. Spectros.* **2003**, *57,* 320A-332A.

(65) Homola, J. *Anal. Bioanal. Chem.* **2003**, *377*, 528-539.

(66) Duverger, E.; Frison, N.; Roche, A. C.; Monsigny, M. *Biochimie* **2003**, *85*, 167-179.

(67) Green, R. J.; Frazier, R. A.; Shakesheff, K. M.; Davies, M. C.; Roberts, C. J.; Tendler, S. J. B. *Biomaterials* **2000**, *21*, 1823-1835.

(68) Brockman, J. M.; Nelson, B. P.; Corn, R. M. *Annu. Rev. Phys. Chem.* **2000**, *51,* 41-63.

(69) Nelson, B. P.; Frutos, A. G.; Brockman, J. M.; Corn, R. M. *Anal. Chem.* **1999**, *71,* 3928-3934.

(70) Knoll, W. *Annu. Rev. Phys. Chem.* **1998**, *49*, 569-638.

Chapter 2:

Optimization of Immobilized Bacterial Disaccharides for Surface Plasmon Resonance (SPR) Imaging Measurements of Antibody Binding

2.1 INTRODUCTION

The technology to fabricate and read biological arrays has progressed rapidly over the last decade. Improvements in the technology have resulted in high-density chips comprised of DNA,[1] proteins,[2] and more recently carbohydrates.[3] The development of arrays of immobilized carbohydrates presents unique and complex problems not encountered with previously developed biochips.[4,5] The source of this complexity rests in the multiple branching points, stereoisomers, and linkage forms present in carbohydrates. Despite these complexities researchers have begun to make great strides in the development of carbohydrate microarrays.[6-13] Motivation for development in this area was a consequence of the biologically significant role that carbohydrates play on the cellular level.

Carbohydrates are present on a cell's surface in varying densities.[14] These surface molecules play a pivotal role in cell signaling and adhesion, pathogen identification, and the immune response.[15-17] In particular, the study of carbohydrates in relation to bacterial interactions/infections is an area of growing concern as the number of drug resistant bacteria increases. According to the world

A version of this chapter has been published. Grant 2008. *Langmuir*. 24: 14125-14131

health organization (WHO), since the 1990s strains of *Salmonella* which are resistant to a range of microbials have emerged and are threatening to become a serious public health problem.[18]

Salmonella is a gram-negative enterobacteria with strains responsible for typhoid fever, paratyphoid fever, and food borne illness. The main division of these *Salmonella* strains is based on variations in the somatic O-antigen. The O-antigen is part of the lipopolysaccharide (LPS) present on the bacteria's cell surface. There are approximately 9×10^6 molecules of LPS on the bacteria surface, each composed of a lipid core, and O-antigen. Located at the terminus of the LPS, the O-antigen is a long carbohydrate chain, up to 40 sugars in length, composed of tri-, tetra-, or pentasaccharide subunits.[19] For example, the O-antigen of *Salmonella* serotypes A, B, and D_1 are each composed of a 4 unit repeating tetrasaccharide. The subunit is composed of a three-sugar backbone with a branched dideoxyhexose. The stereochemistry of the branched dideoxyhexose provides the variation between the three serogroups and is significant enough to provide antigenic specificity. Substitution studies have confirmed the importance of stereochemistry in antibody binding. When the abequose dideoxyhexose (serotype B) was substituted with tyvelose (serotype D_1) or paratose (serotype A) inactive compounds resulted.[20]

Chips containing arrays of relevant carbohydrates can potentially be used as diagnostic tools to detect antibodies specific for the infecting species of bacteria present in a patient. In this work, surface plasmon resonance (SPR) imaging[21,22] is used as the detection platform to optimize the fabrication of array chips for the study of antibody binding to a family of structurally related *Salmonella* disaccharide epitopes. Previous work examining antibody binding to similar epitopes used a solid phase enzyme immunoassay or microcalorimetry.[23,24] These studies, while effective, required numerous steps and significant quantities of samples. SPR has been used in numerous carbohydrate binding studies,[25-32] and there have been several reports on the use of SPR imaging as a label-free detection platform for carbohydrate arrays.[30,33-36] Relevant to the present work, SPR imaging was used to screen serum antibody binding to an array of natural glycans. The glycans were covalently immobilized to an epoxide modified chip.[35] Here, an array of the disaccharide epitopes is used to probe the effect of stereochemistry and surface density on antibody binding. The disaccharide probes were synthetically modified to contain an alky thiol linker that allows the self-assembly of monolayers terminating in the disaccharide. The density of disaccharide in each array spot was varied in an effort to optimize the array surface chemistry. We find that both the amount of antibody bound and the binding constant depends greatly on probe density. The composition of the microarray surface was thoroughly characterized with infrared reflection absorption spectroscopy (IRRAS), x-ray photoelectron spectroscopy (XPS), and scanning force microscopy (SFM).

2.2 EXPERIMENTAL

Materials and Methods. Chemicals were obtained from the following sources: 11-mercaptoundecanol (MUO) was obtained from Sigma and used as received. The Tris buffer used (pH 8.0) was composed of 50 mM Tris-HCl (Sigma), and 150 mM NaCl (EMD Chemicals, Inc.) and 0.02% NaN_3 (EMD Chemicals, Inc.). All components of the buffer were used as received. The alkyl-thiol modified disaccharides, abequose (3,6-dideoxy-D-*xylo*-hexose) SMA 17, paratose (3,6-dideoxy-D-*ribo*-hexose) SMA 27, and tyvelose (3,6-dideoxy-D-*arabino*-hexose) SMA 9 were synthesized as described previously.[37] The antibody Se155-4 used belongs to the IgG1(λ) subclass[24] and precipitated the polysaccharide antigen from serogroup B Salmonella. Stock solutions of the antibody (41 μM) were dissolved in 50 mM Tris buffer (pH 8.0). All water used was demineralized (18 MΩ) in a Nanopure water purification system (Barnstead). All ethanol used was anhydrous ethanol from Commercial Alcohols Inc., Ontario.

Immobilization of Disaccharide Probes on SPR Chips. Equal molar stock solutions of disaccharide and 11-mercaptoundecanol (MUO) were prepared in ethanol. Aliquot volumes were manipulated to create different solution mole fractions of disaccharide and MUO with a total thiol concentration of 0.1 mM. 500 μL of the ethanolic thiol mixture was diluted with 500 μL of demineralized water, resulting in a solution of 0.05 mM total thiol concentration in 50/50 ethanol/water. The water was necessary to allow for spot confinement on the Spotready™ chips. Solutions were incubated overnight at 4°C to allow for adsorption to an ozone cleaned gold surface. Samples were rinsed with ethanol and water and used immediately.

Surface Plasmon Resonance (SPR) Imaging Assays. Commercial SPR chips, Spotready™, were used for all experiments. The chips consist of 17 gold spots, 1 mm in diameter on a 1.8 cm × 1.8 cm glass (SF-10) substrate. The SPR images were collected with a GWC Technologies (Madison, WI) SPR Imager II. The instrument set-up has been described elsewhere.[38] All images were collected in Tris buffer. Images were collected and analyzed using V^{++} software. Raw values were converted to $\Delta\%R$ values using an equation set out by the manufacturer. Replicate data was averaged and corrected for bulk changes in refractive index and non-specific adsorption using the MUO spot from the same column.

Infrared Reflection Absorption Spectroscopy (IRRAS). Substrates for IRRAS analysis were Bev-l-edge micro slides (Proper Manufacturing Co., Inc., Germany) and were cleaned in piranha solution (75% H_2SO_4: 25% H_2O_2) prior to metal deposition. Thin films of chromium (10 nm) and gold (300 nm) were deposited using a thermal evaporation system (Torr International, Inc.). Monolayers and mixed monolayers were prepared by immersing the entire gold-coated substrate in 50/50 ethanol/water solutions of various compositions of disaccharide and MUO overnight at 4^{o}C. Spectra were collected using a Matson Infinity FT-IR equipped with a low-noise mercury-cadmium-tellurium detector cooled with liquid N_2 to 77K. Spectra were collected from 1000 scans at a resolution of 2 cm^{-1}. The incoming IR light was p-polarized and incident on the sample at a glancing angle of approximately 80^{o}. A self-assembled deuterated octadecanethiol monolayer or an ozone cleaned Cr/Au coated slide were used as the background.

AFM Measurements. Substrates used consisted of a 300 nm gold film thermally evaporated onto 3 cm diameter circular piece of Tempax glass (Berliner Glass). These substrates were annealed in an H_2-flame in order to provide large Au(111) crystallites.[39] Monolayers and mixed monolayers were prepared by immersing the entire gold-coated substrate in 50/50 ethanol/water solutions of various compositions of disaccharide and MUO overnight at 4^{o}C. Images were collected with a Digital Instruments Nanoscope IIIa (Veeco, Santa Barbara) using triangular Si_3N_4 cantilevers (Nanoprobes, Digital Instruments) with a spring constant of 0.12 N/m. Height and lateral force (friction) images were collected simultaneously. Friction loops were collected over a 50 nm line scan at varying set-point voltages on atomically flat Au(111) terraces.[39] For friction analysis all samples were probed with the same cantilever/tip.

X-ray Photoelectron Spectroscopy (XPS). The XPS measurements were performed on AXIS Ultra spectrometer (Kratos Analytical) at the Alberta Centre for Surface Engineering and Science (ACSES). The base pressure in the analytical chamber was lower than 4×10^{-8} Pa. The resolution function of the instrument for Al-mono source, hybrid lens mode has been determined to be 0.55 eV for Ag 3d and 0.70 eV for Au 4f peaks. Monochromated Al Kα source ($h\nu = 1486.6$ eV) was used at power of 210 W. Fixed analyser transmission (FAT) mode was applied with analysis spot set at 700 x 400 um. Charge neutralization during the measurements was not required. All survey scans spanned from 1100 to 0 eV binding energy and were collected with analyzer pass energy (PE) of 160 eV at a step of 0.3 eV. For the high-resolution spectra the pass-energy was 20 eV with a step of 0.1 eV. The number of scans varied from 2 for Au 4f to 40 for N1s.

2.3 RESULTS AND DISCUSSION

SPR Imaging of Disaccharide Arrays. SPR imaging has been used in a number of studies for the parallel, label-free detection of multiple biological interactions in an array format. It is well recognized that assays featuring arrays of immobilized probes enable the simultaneous detection of numerous targets. In addition to this high throughput advantage, arrays can also be used to optimize the design of an assay by exploring various probe immobilization schemes on a single chip. Previous SPR imaging studies of protein binding to immobilized carbohydrates have shown that the amount of lectin and toxin protein binding depend on the surface density of immobilized carbohydrates. We thus employed a 17-spot array to detect antibody interactions with the three disaccharides shown in Figure 2.01, as well as probe the effect of the surface density of each carbohydrate. The three disaccharide probes studied here represent the immunodominant sugars from serogroups A, B, and D_1 of *Salmonella.*[40] The disaccharides have been modified with an alkane-thiol tail as shown in Figure 2.01 to enable self-assembly on a gold surface.[41-45] Forming mixed monolayers, containing the probe and a diluent species, controlled the surface density of each disaccharide probe. Mercaptoundecanol (MUO, Figure 2.01) was chosen as a diluent as –OH terminated monolayers have been shown to resist non-specific protein adsorption.[46,47]

We and others have previously utilized polydimethylsiloxane (PDMS) microfluidic networks to pattern gold surfaces for SPR imaging experiments. Here the substrate for the array is a glass chip patterned with 17 gold spots designed for spotting with a hand held micropipet. The glass background is modified, rendering it hydrophobic, to ensure the droplets are contained on the 1 mm diameter gold spot. A micropipet was used to deliver 600 nL ethanol/water solutions of disaccharide/MUO mixtures. The mole fraction of the disaccharide vs. MUO in the solution was varied as a means of generating mixed monolayers of varying disaccharide density (*vide infra*). A spot of only MUO was also prepared as a control. Following droplet delivery, storing the chip in a humid environment enables the assembly of the probe molecules on the gold surface overnight.

The results of an experiment probing the antibody binding to a chip containing the three functionalized immunodominant *Salmonella* disaccharides spotted from various solution mixtures is shown in Figure 2.02. Each row of the chip contained a different disaccharide, except the last two rows, where SMA 27 was spotted twice. Each column represents a different solution mole fraction of SMA mixed with MUO used to adsorb the monolayer on each spot. The lower right spot contains only a monolayer of MUO. Figure 2.02(A) is an SPR difference image following incubation of the chip in a 600 nM solution of Se155-4 monoclonal antibody. An increase in signal is only observed at the spots containing SMA 17. The ability of the antibody to differentiate between the three stereoisomers and selectively bind to the immunodominant sugar from serogroup

B, SMA 17, is shown more quantitatively in Figure 2.02(B). The bar graph of Figure 2.02(B) presents the responses for the right-most column of spots (denoted "B") as well as the response at the MUO control spot. Significant antibody binding is observed on the SMA 17 spot, with undetectable binding observed at the other disaccharides or the MUO control.

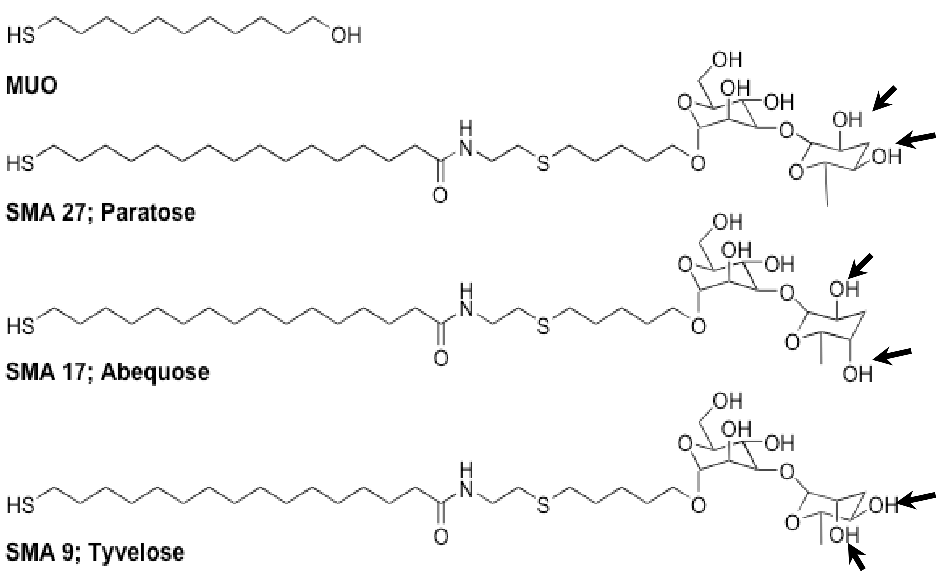

Figure 2.01. Structures of alkyl thiol disaccharide probes used to form monolayers in this work. The stereochemistry of the –OH groups indicated by the arrows defines the structural differences in the probes.

The binding of the monoclonal antibody Se155-4 to the abequose trisaccharide has been characterized both structurally[24] and thermodynamically.[48,49] The results in Figure 2.02 show that the Se155-4 antibody can also selectively recognize the modified disaccharide epitope immobilized on a surface. This opens pathways for the sensitive and rapid measurement of binding data for these types of systems.

The effect of the density of probes on the array surface is also revealed in Figure 2.02. Figure 2.02(C) is a bar graph of the SPR signals along the row of SMA 17 spots. There have been a number of reports that show that the surface density of a specific adsorbed thiolate can be controlled in a mixed monolayer by varying its solution mole fraction with respect to a diluent thiol.[44,50,51] In this case, surface density of probe disaccharide in each spot scales with its mole fraction in the solution used to prepare the spot (*vide infra*). At high surface densities antibody binding is minimal. However, as the density of disaccharide was reduced by dilution with MUO, a significant increase in antibody binding was observed.

Antibody binding curves were obtained for several surface densities of SMA 17 disaccharide to further quantify the effect of disaccharide surface density. The data for the binding curves was obtained from a chip that exploited the ability of array assays to generate replicate measurements. Each solution mole fraction of SMA 17 was spotted at three different array addresses. The array also contained five MUO control spots. The chip was exposed and analyzed following introduction of increasing antibody concentrations, from 2 nM to 600 nM. An SPR image of the chip following binding from a 600 nM solution of Se155-4 monoclonal antibody is shown in Figure 2.03(A). The average Δ%R values (3 spots) for the two surface densities that provided measurable binding are plotted vs. antibody concentration in Figure 2.03(B). The signals observed at the MUO control spots are also plotted in Figure 2.03(B).

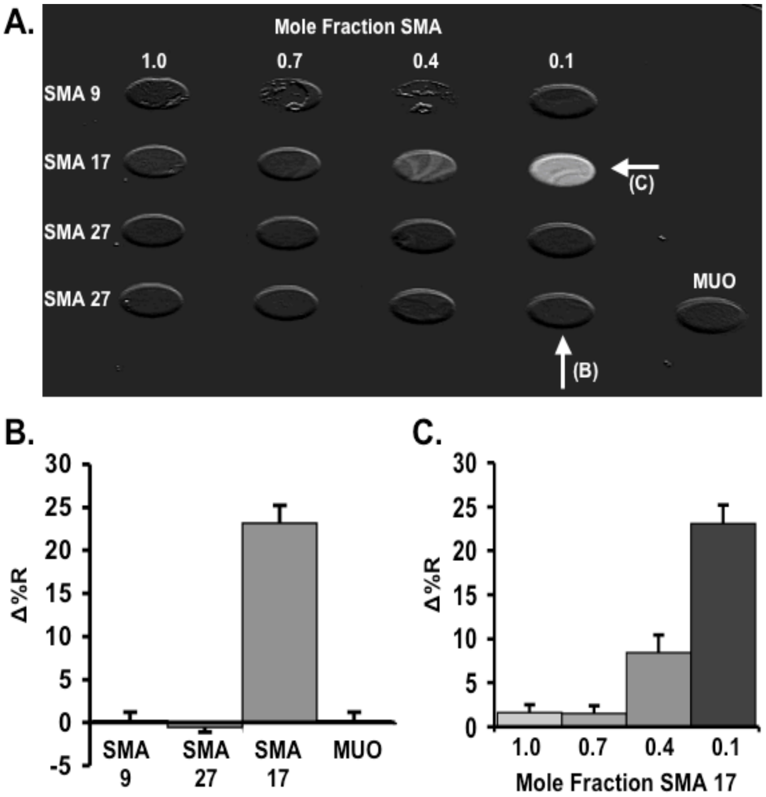

Figure 2.02. A. SPR difference image of an SMA array following incubation in 600 nM Se155-4 monoclonal antibody (10 min). Image collected in antibody free Tris buffer (pH 8.0). B. Bar graph of the signals along the rightmost column (denoted with the arrow B). C. Bar graph of the signals for the SMA 17 row (denoted with the arrow C). Error bars represent the standard deviation of the mean for replicate spots on a single chip.

The data in Figure 2.03(B) was fit with a four-parameter logistical equation of the following form:

$$\Delta\%R = \Delta\%R_{\min} + \frac{\Delta\%R_{\max} - \Delta\%R_{\min}}{1 + \left(\frac{[A]}{K_d}\right)^{b}} \qquad (1)$$

The least squares solution of this equation has been widely used to analyze binding curves and is one of the most reliable and flexible curve fitting techniques for immunoassays.[52,53] The $\Delta\%R_{max}$ and $\Delta\%R_{min}$ are asymptotic values obtained from the regression analysis, [A] is the concentration of antibody in solution, and K_d is the dissociation constant. As K_a and K_d values are typically ascribed to solution based measurements will we refer to these values as K_{ADS} and K_{ADS}^{-1}, a more physically correct nomenclature for surface based bioassays.[30] In this study, the reciprocal of the K_d value obtained from the regression analysis will be reported as K_{ADS} (where $K_{ADS} = 1/K_d$). The value b in equation (1) is the Hill coefficient and represents the slope of the curve at the inflection point. Note that when b is equal to unity, equation (1) reduces to the Langmuir isotherm. Proposed interpretations for deviations from $b = -1$ include inhomogeneity in binding affinities or negative cooperativity for $b > -1$ and positive cooperativity for $b < -1$.[53] Although inferences based on deviations of b from unity remain somewhat speculative, a Hill coefficient of -2 would be expected for binding of a 2-site antibody.[54]

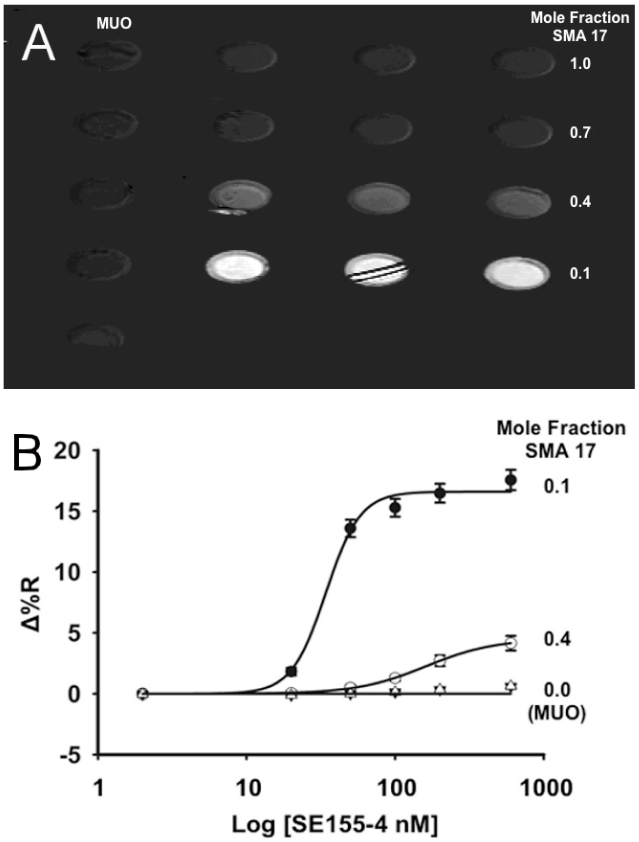

Figure 2.03. A. SPR difference image of an SMA 17 array following antibody binding. Binding curves collected at different spots on the array in A. The points represent the average signal from three similar spots and the error bars are the standard deviation. The line through the points is the least squares fit of the four parameter logistical equation (see text).

Table 2.1 presents the fitting parameters obtained from the least squares analysis for antibody binding at the spots prepared from solutions containing mole fractions of 0.1 and 0.4 SMA 17. These values quantify the impact of disaccharide surface density on the amount of antibody bound ($\Delta\%R_{max}$) and the strength of the disaccharide-antibody interaction (K_{ADS}). It is apparent from both the plot in Figure 2.03(B) and from Table 2.1, that the saturation amount of antibody bound to the array ($\Delta\%R_{max}$) greatly depends on the surface density of immobilized SMA 17, with the lowest surface density, from a $\chi = 0.1$ solution of SMA 17, yielding the highest amount of bound antibody. Surprisingly, a non-diluted monolayer of SMA 17 binds very little antibody. Also, negligible adsorption of the antibody is observed on the MUO control spots, indicating that all observed signals are due to the specific interaction of the Se155-4 monoclonal antibody with the immobilized SMA 17. The four-parameter fits of the binding data also show a dependence of surface density on the strength of the interaction. Comparison of the K_{ADS} values in Table 2.1 reveals that the antibody binds slightly more than 20× tighter to the $\chi = 0.1$ surface than to the $\chi = 0.4$ surface. The values for the Hill coefficients in Table 2.1 are both < -1, which is expected for a multi-site antibody bound to surface immobilized antigens.

Table 2.1. Curve fitting parameters for antibody binding curves for two of the mixed monolayers. Error values are the uncertainties derived from the fit.

Mole fraction of SMA 17	**R^2**	**K_{ADS} (M^{-1})**	**Min.**	**Max.**	**b**
0.1	0.9932	$2.92 \pm 0.94 \times 10^7$	0 ± 1	16.6 ± 0.6	-3.8 ± 0.9
0.4	0.9996	$6.25 \pm 0.04 \times 10^6$	0.00 ± 0.04	4.5 ± 0.1	-1.9 ± 0.1

Calorimetry experiments have reported an association constant (K_a) of 2.4 ± 0.2 x 10^4 M^{-1} for the binding of abequose-mannose, the disaccharide at the terminus of SMA 17, with the Se155-4 antibody.[24] This value is three orders of magnitude lower than the one observed on a dilute surface of SMA 17 ($\chi_{soln} = 0.1$). Previous studies examining the effect of lectin binding to a carbohydrate surface compared binding constant values from a surface based assay using SPR imaging with solution based values. The study found that the surface based analysis consistently provided values three orders of magnitude larger than the solution measurement.[30] The difference between K_{ADS} values measured here and K_a values from microcalorimetry are consistent with the previous report.

There have been several published reports on the effect of probe density on target binding.[30-32,36,50,55] Mixed alkanethiolate monolayers have been used to control carbohydrate surface density and these studies have shown lower lectin binding at high carbohydrate surface density.[30,32] This has been attributed to tight tailgroup packing in this monolayer system, resulting in limited access of the ligands to the protein binding pockets or lateral interactions between the ligands. Another study examined the incorporation of an enzyme into varying densities of surface immobilized carbohydrate and reported reduced binding under high and low carbohydrate surface density, with maximal enzyme binding on a ~ 70% carbohydrate surface. The observation was attributed to steric crowding of carbohydrate ligands at the interface, thus inhibiting protein binding.[50] While this is a plausible explanation for the trend we observe here, knowledge of the density and arrangement of carbohydrate groups in the mixed monolayers of SMA 17 and MUO is required to fully explain our trends. Furthermore, the large difference in antibody binding we observe, from complete inhibition at an undiluted disaccharide surface to significant binding at a very dilute surface, has not been observed previously. Therefore, a thorough analysis of the structure of the mixed monolayers formed under the different dilutions was undertaken to provide information on the interface formed by the self-assembly of these mixed monolayer systems.

Chain Structure of Mixed SMA 17/MUO Monolayers. The two-dimensional packing of the alkane chains in the mixed monolayers will impact the presentation of the disaccharide to the interface. Infrared reflection absorption spectroscopy (IRRAS) has been used extensively to probe the chain structure of monolayers formed by alkanethiols on gold.[42,45,56] This usage stems from the work of Snyder and co-workers, who have shown that the infrared signature of methylene C-H stretches are diagnostic of chain packing in condensed phase n-alkane systems.[57,58] The position and width of the asymmetric methylene stretch ($\nu_{a,CH2}$) is sensitive to the chain environment in monolayer systems. A position for $\nu_{a,CH2}$ of 2918 ± 1cm^{-1} is characteristic of a monolayer consisting of alkyl groups that "on average" experience a crystalline-like environment, with the methylene groups in an all-trans conformation.[42] Partial disruption or alterations of these lateral interactions leads to minor gauche defects, which are observed as a blue shift of the band and peak broadening.

IRRAS spectra were collected on monolayer samples prepared from SMA 17/MUO solution compositions similar to those used for spotting SPR chips to evaluate antibody binding. Table 2.2 presents the results of the spectral analysis and lists peak position, intensity, and peak width for the asymmetric methylene vibration. The position of the band ranges from 2917 cm^{-1} to 2920 cm^{-1}, and considering the spectral resolution of 2 cm^{-1}, there are no significant deviations in peak position. However, the peak width at half maximum (PWHM) and intensity do show a dependence on the solution composition used for adsorption. As the mole fraction of the disaccharide is decreased the intensity and width of the vibration is reduced. The variation in intensity observed is due to the greater number of CH_2 groups in the disaccharide probe molecules relative to the MUO diluent (Figure 2.01). The trend is evidence that the solution composition is influencing surface composition. This will be reinforced in studies described below. We attribute the increase in peak width and the band asymmetry for monolayers prepared from solutions with high SMA 17 content to more disordered packing in the top-most portion of the layer. This disorder is likely due to the bulky disaccharide terminal group as well as the amide and sulfide functionalities in the tether (Figure 2.01). Based on these findings we conclude that the mixed monolayers formed from solutions of SMA 17 and MUO exhibit reasonably well ordered chain structure at the innermost portion of the monolayer (the first 10 to 11 CH_2 units) and are presenting the carbohydrate moiety at the solid-solution interface.

Table 2.2. IRRAS data for the asymmetric methylene CH stretch for the various monolayers and mixed monolayers. Error values are standard deviations from at least three measurements. Spectral resolution was 2 cm^{-1}.

χ_{soln} SMA 17	$\nu_{a,CH2}$ (cm^{-1})	Absorbance (×10^3)	PWHM (cm^{-1})
1.0	2919	1.38 ± 0.04	27.5 ± 0.5
0.7	2920	1.37 ± 0.04	24 ± 2
0.4	2918	1.28 ± 0.06	23 ± 3
0.1	2917	0.64 ± 0.09	19.6 ± 0.4
0.0	2918	0.69 ± 0.01	19 ± 1

Composition of Mixed SMA 17/MUO Monolayers. The composition and structure of two-component mixed monolayers derived from thiols on gold have been explored in a number of studies.[44,56,59-63] The systems studied have been primarily a mixture of two n-alkanethiols of different length[60,62,63] and an n-alkanethiol mixed with an alkyl thiol terminated in a simple functional group (e.g., -CH_2OH, COOH, -CH_2Br, -CH_2CN).[44,56] It has been shown that the mole fraction of one component on the surface is related to its mole fraction in solution.[44,56,61] The trends have followed both linear and non-linear profiles and in general, the composition of the monolayer is not equivalent to the composition in solution. Mixed monolayers consisting of an alkyl thiol with a relatively small terminal group (-CH_2OH) and an alkyl thiol with a bulky sugar group are not as well characterized. We thus employed a variety of techniques to characterize the relationship between surface composition and solution composition for the SMA 17/MUO mixed monolayer studied here.

Characterization comes in part from the SPR signals observed for the initial chip containing spots produced from the different solution mixtures of SMA 17 and MUO. For a chip similar to that used in Figure 2.03, the initial percent reflectivity (%R) values of this array collected in Tris buffer were analyzed and the results are listed in Table 2.3. The initial %R measured at each spot on the chip is a measure of the refractive index of the different monolayers on the spots. Thus, %R-values should track the molecular weight of the components in the monolayer. As shown in Table 2.3, %R-values track the mole fraction of SMA 17 in the solution used for spotting. The molecular weight of the SMA 17 is over three times larger than the MUO diluent. Therefore, as the amount of immobilized disaccharide decreases and is replaced with MUO, the total mass of material on the spots decreases resulting in a decrease in the index of refraction and a decrease in %R. Similar trends have previously been reported with SPR imaging when examining initial reflectivity values for probe molecules of different sizes.[36]

IRRAS provides another means to probe the surface composition of mixed monolayers.[56] Figure 2.04 presents IRRAS spectra in the region between 1450 and 1650 cm^{-1} obtained for the SMA 17/MUO mixed monolayers. The spectra contain a peak centered at 1555 cm^{-1} resulting from the NH bending vibration of the secondary amine group present in the disaccharide backbone (Figure 2.01). The amide bond is not present in the diluent MUO and therefore, the intensity of this band may be used to directly track the surface concentration of SMA 17. The peak intensities measured are listed in Table 2.3, which shows a decrease in intensity of the amide II band as the solution percentage of disaccharide is decreased. We note that the amide band for monolayers formed from a solution containing a disaccharide mole fraction of 0.1 are below the detection limit of the IRRAS measurement. The results from the IRRAS analysis agree with the SPR data presented above, and reinforce that changing the mole fraction of disaccharide in solution is an effective way to control the composition of the monolayer formed.

XPS has been a common surface characterization technique used in studies examining mixed monolayers of thiols on gold.[56,60,64] The atomic composition data provides relative surface coverage values for the components in a mixed monolayer. Here the nitrogen 1s peak from the amide bond in the backbone of the disaccharide was used to quantify the relative amounts of disaccharide on the surface. Figure 2.05 contains the high-resolution XPS spectra of the various film compositions with the peak at 400.5 eV corresponding to the N1s photoelectrons. The intensity of N1s peak collected for the mixed monolayers are also listed in Table 2.3. The N1s intensities were corrected for the inelastic scattering of photoelectrons caused by variations in film thickness through referencing to the Au 4f peak area.[65] As the mole fraction of disaccharide in solution decreases the N1s peak area also decreases, confirming the surface dilution of disaccharide molecules with MUO diluent.

The three characterizations presented above provide evidence that the amount of SMA 17 on the surface tracks its percentage in solution. Based on previous reports on the spontaneous adsorption of thiol derived mixed monolayers, this is not an unexpected result.[44,56,60-62] However, it is important to establish a complete picture of the structure of the SMA 17/MUO system to understand the observed antibody binding behavior. A more direct relationship between the surface density of SMA 17 and solution mole fraction is established by normalizing the signals from each characterization technique by the signal for the pure SMA 17 monolayer. The normalized values for each analysis are shown in Table 2.4. The average fractional values from the three analyses can be considered a semi-quantitative measurement of the mole fraction of SMA 17 on the surface. Figure 2.06 is a plot of the mole fraction on the surface vs. the solution mole fraction. A linear least squares analysis provides a reasonably good fit to the data, indicating a linear relationship between solution composition and surface composition for SMA 17/MUO monolayers. However, the non-unity slope of 0.82 shows that the surface composition is not equivalent to the solution composition. Specifically, lower solution mole fractions of SMA 17 (e.g., 0.1) result in a monolayer with a higher surface mole fraction (e.g., 0.25). This agrees with earlier studies that show longer alkyl chain thiols preferentially adsorb over shorter chains, consistent with thermodynamic control over the adsorption process.[60,62] Considering the antibody binding data in Figure 2.03(B), it appears that a surface consisting of ~25% of a monolayer of SMA 17 diluted with MUO provides an optimal substrate for antibody screening. Although not shown here, work by a previous student has demonstrated reduced antibody binding when χ_{soln} of SMA 17 is reduced below 0.1.[52]

Table 2.3. Results from the three characterizations of mixed SMA 17/MUO monolayers. Error values are either the standard deviation from multiple measurements or the experimental uncertainty.

χ_{soln} SMA 17	SPR imaging %R	IRRAS Amide II Absorbance ($\times10^3$)	XPS N1s ($\times10^2$)
1.0	46.0 ± 0.4	1.09 ± 0.04	1.78 ± 0.09
0.7	42.6 ± 0.5	0.70 ± 0.04	1.21 ± 0.06
0.4	40 ± 1	0.57 ± 0.04	0.65 ± 0.03
0.1	37.3 ± 0.4	-	0.47 ± 0.02
0.0	34.6 ± 0.3	-	-

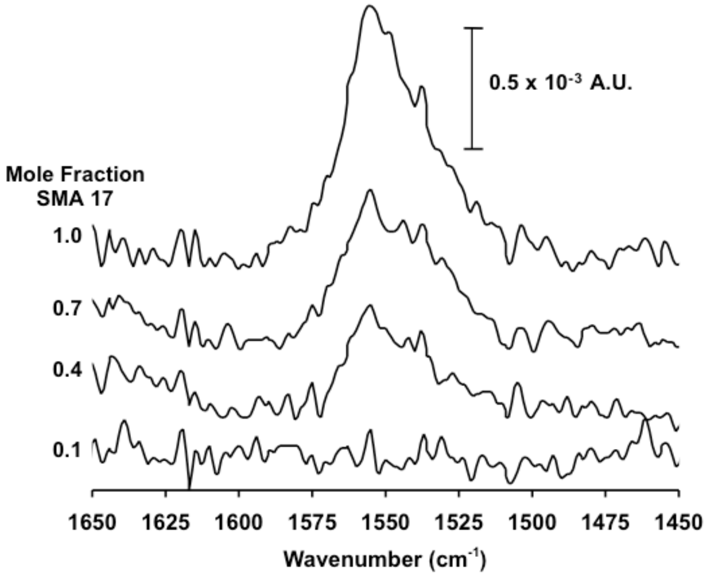

Figure 2.04. IRRAS spectra for single component and mixed monolayers of SMA 17 and MUO. Band at 1555 cm^{-1} is assigned as the amide II band.

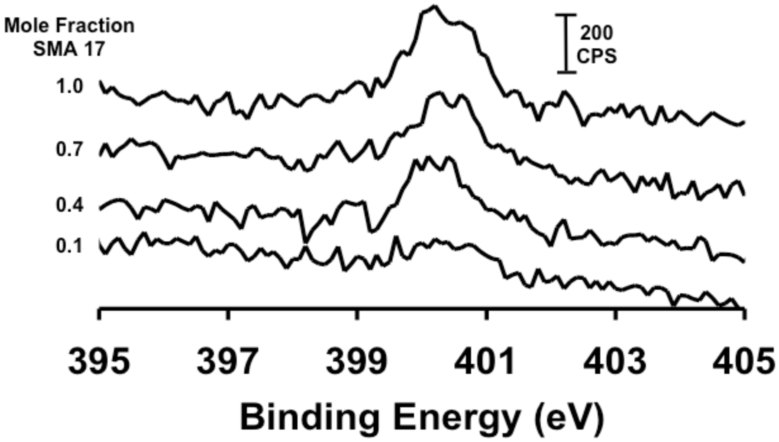

Figure 2.05. High resolution XPS spectra in He N1s region for single component and mixed monolayers of SMA 17 and MUO.

Table 2.4. Normalized values from the various characterizations of the SMA 17/MUO mixed monolayers from Table 2.3. Error values are propagated uncertainties.

χ_{soln} SMA 17	SPR[a]	IRRAS	XPS	Average
1.0	1.00 ± 0.01	1.00 ± 0.05	1.00 ± 0.07	1.0 ± 0.1
0.7	0.70 ± 0.01	0.64 ± 0.04	0.68 ± 0.05	0.67 ± 0.09
0.4	0.47 ± 0.01	0.52 ± 0.04	0.36 ± 0.02	0.45 ± 0.09
0.1	0.237 ± 0.003	-	0.26 ± 0.02	0.25 ± 0.03

a. SPR data was normalized by first subtracting the signal for the pure MUO monolayer then dividing all values by the signal for the pure SMA 17 monolayer.

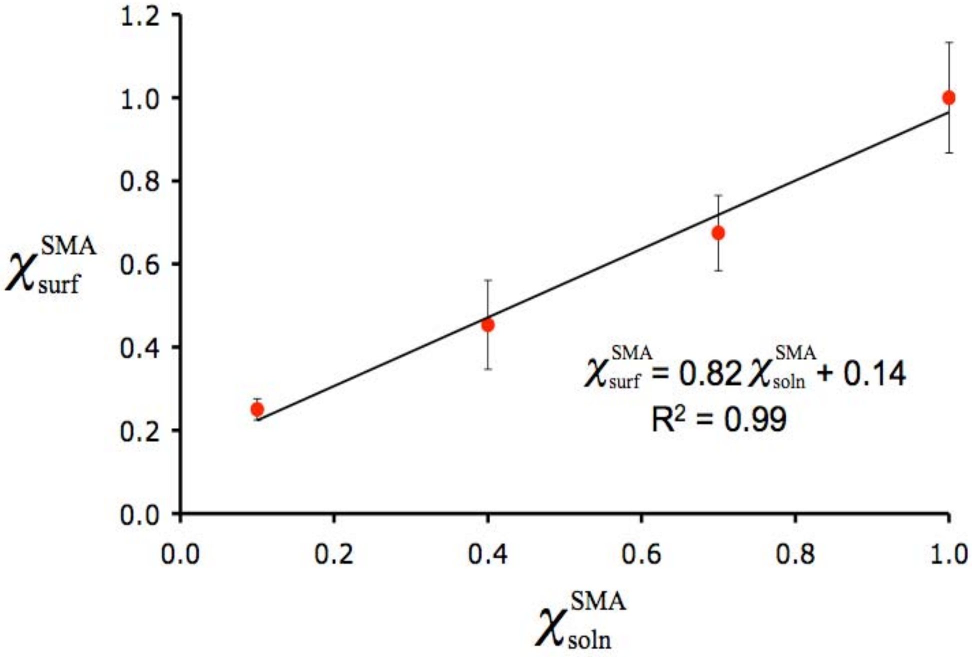

Figure 2.06. Plot of the surface mole fraction of SMA 17 in mixed monolayers vs the mole fraction in solution. The surface mole fractions values are the average values from the three characterizations in Table 2.4. Error bars represent the propagated uncertainties listed in Table 2.4.

Spatial arrangement of mixed SMA 17/MUO monolayers. The majority of published reports suggest that the components of mixed thiol derived monolayers on gold are homogeneously mixed.[44,56,60-62] A scanning tunneling microscopy (STM) investigation provided some evidence for phase segregation in a mixed monolayer system consisting of an n-alkanethiol and an ester-terminated alkyl thiol. The observed nanometer scale domains were found to vary in shape with time.[63] The spatial arrangement of the SMA 17 molecules in the mixed monolayers investigated here is expected to have a large impact on antibody binding. The dependence of the amount of antibody bound and the binding constant on surface composition implies that the SMA 17 molecules are homogeneously distributed in the MUO layer. To confirm this hypothesis, we employed scanning force microscopy (SFM) to map the 2-dimensional arrangement of surface chemistry in these mixed monolayers.

It is well established that nanoscale friction measured by SFM is sensitive to the interfacial surface chemistry of thiol derived monolayers on gold.[39,67-69] To exploit this utility of SFM here we initially characterized the frictional response of the monolayer compositions of interest here in a semi-quantitative fashion. Figure 2.07 contains plots of the friction signal as a function of the normal force between the tip and each monolayer. Each point was collected by monitoring the lateral deflection of the cantilever during a back and forth scan along a single, 50 nm line (i.e., a friction loop[39]). Figure 2.07 shows that the SFM measured friction tracks the normal force between the tip and sample for all monolayers examined, consistent with observations at other terminally functionalized thiol derived monolayers on gold.[39] It is also apparent from Figure 2.07 that each surface composition yields a different frictional response. The highest tip-sample friction for all normal forces is measured at the monolayer prepared from pure SMA 17 ($\chi_{surf} = 1.0$). This is likely due to a large adhesive force between the disaccharide terminal groups and the Si_3N_4 tip. The lowest friction is measured at the pure MUO monolayer with intermediate values that scale with the mole fraction of SMA for the mixed monolayers. The intermediate friction observed is consistent with homogeneously mixed layers. The frictional signal was uniform across the 50 nm line scan during the course of the measurement for these samples.

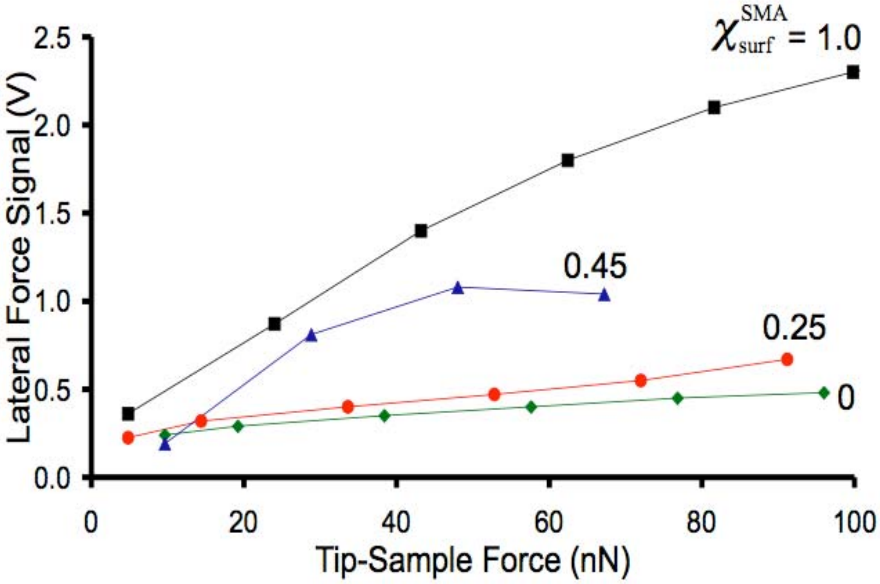

Figure 2.07. Plots of the SFM measured lateral (friction) force signal (in V) vs the tip-sample normal force for pure SMA 17/MUO monolayers and mixed monolayers. All plots were collected with the same tip/cantilever. The points are the raw data while the line connecting the points is simply a guide to the eye.

It is clear from Figure 2.07 that the frictional signature of the pure SMA layers is easily distinguished from the MUO. Thus, phase segregated domains of each of these components will be easily discernable in a friction force image. Both the pure component and mixed monolayers were imaged in friction force mode on a variety of length scales. Figure 2.08 contains representative images of several of the samples examined. Each image in Figure 2.08 is 400 × 400 nm collected on a Au(111) terrace. The contrast in all images is uniform with little variation in the friction. In all images collected we did not observed any evidence of localized variations in friction at any length scale that would indicate phase segregated domain formation. This provides compelling evidence that the SMA 17 is uniformly mixed within the MUO.

We can now conclude that the monolayer that provided the highest level of antibody binding (Figure 2.04) consists of ~25% SMA 17 and 75% MUO and that these components are homogeneously mixed. The greater chain length of the modified disaccharide relative to the MUO diluent permits the epitope to extend into the solution. This sensing surface has the optimal structure and distribution of disaccharides to allow for complete access to the antibody for bivalent binding. This situation is depicted in Figure 2.09. A layer consisting of closely packed disaccharides can lead to enthalpically diminished binding.[70] Under moderate surface densities ($\chi_{surf} = 0.45$) the initial binding of one antibody-binding site causes shifting/aggregation of the disaccharides at the interface close to where the primary binding occurred thus, interfering with the next binding event. The second binding event can only occur following further rearrangement of the disaccharide surface. The energy barrier for reorganization would be reflected in a lower binding constant as is observed here ($\chi_{so\ln} = 0.4$). Under extreme cases of high surface density of disaccharide ($\chi_{so\ln} = 0.7$ and 1.0) the binding is so enthalpically and sterically hindered that minimal binding occurs.

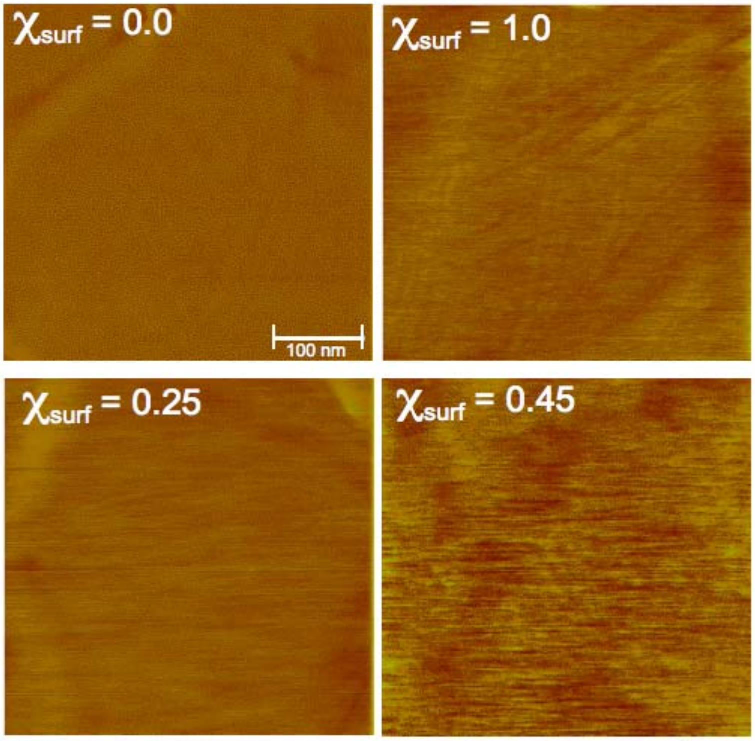

Figure 2.08. 400 × 400 nm friction force images of SMA 17/MUO monolayers and mixed monolayers. Z-scale for all images is 1.5 V. All images were collected with the same tip/cantilever at a normal force of ~50 nN.

Crystallographic findings for the Se155-4/abequose trisaccharide binding show that carbohydrate binding occurs near the twofold axis of the V_L-V_H interface of the antibody, in a pocket approximately 8 Å deep and 7 Å wide. Complete binding of the carbohydrate requires the abequose sugar be totally buried in the antibody binding pocket while the other saccharide units lie on the protein surface.[20] Due to its smaller size, the complete insertion and orientation of disaccharide is critical to ensure binding of significant strength. The dilution of the SMA 17 in a mixed monolayer with MUO allows for this complete insertion. This finding is consistent with others that demonstrated a dilute carbohydrate layer yields optimal interactions with enzymes,[50] lectins,[30] and protein toxins.[36]

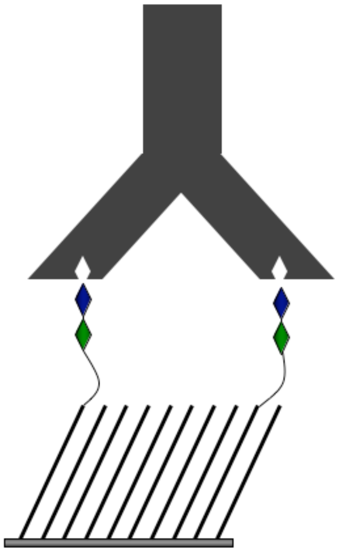

Figure 2.09. Illustration of the optimized disaccharide surface for antibody binding.

2.4 CONCLUSIONS

The current study represents the characterization and optimization of a label-free carbohydrate immunoassay. Characterization of the microarray surface confirmed the ability to control the surface density of disaccharide by altering the solution composition used for self-assembly. The variations in surface chemistry affected the amount of antibody bound as well as the strength of the interaction. Both the binding affinity and capacity is maximized on a surface consisting of

~25% carbohydrates in a micro- and macroscopically homogenous mixed monolayer. The lower surface density of carbohydrates in the mixed monolayer permits complete insertion of the epitope into the antibody binding pocket. The benefits of the SPR imaging platform for carbohydrate microarrays have been previously noted[30,34,35] and include label-free, sensitive detection in a parallel format. Here, SPR imaging is used for the sensitive and rapid parallel determination of binding constants for the three *Salmonella* serotypes. Applications for these arrays may include antibiotic screening to treat ever-growing number of antibiotic resistant salmonella. Patients who have contracted salmonellosis would present antibodies specific for the infecting species of bacteria present. The type of array presented here could yield information on the status of the infection including the strain and serogroup of the bacteria. This information would provide rapid and specific information to the health care professional and permit specific prescription of antibiotics if required.

2.5 REFERENCES

(1) Bulyk, M. L. *Curr. Opin. Biotechnol.* **2006**, *17*, 422-430.

(2) Hu, Y.; Uttamchandani, M.; Yao, S. Q. *Comb. Chem. High Throughput Screening* **2006**, *9*, 203-212.

(3) de Paz, J. L.; Seeberger, P. H. *QSAR Comb. Sci.* **2006**, *25*, 1027-1032.

(4) Khan, I.; Desai, D. V.; Kumar, A. *J. Biosci. Bioeng.* **2004**, *98*, 331-337.

(5) Bertozzi, C. R.; Kiessling, L. L. *Science* **2001**, *291*, 2357-2364.

(6) Fukui, S.; Feizi, T.; Galustian, C.; Lawson, A. M.; Chai, W. G. *Nat. Biotechnol.* **2002**, *20*, 1011-1017.

(7) Horlacher, T.; Seeberger, P. H. *Chem. Soc. Rev.* **2008**, *37*, 1414-1422.

(8) Houseman, B. T.; Mrksich, M. *Chem. Biol.* **2002**, *9*, 443-454.

(9) Love, K. R.; Seeberger, P. H. *Angew. Chem., Int. Ed.* **2002**, *41*, 3583-3586.

(10) Park, S.; Lee, M. R.; Pyo, S. J.; Shin, I. *J. Am. Chem. Soc.* **2004**, *126*, 4812-4819.

(11) Shin, I.; Park, S.; Lee, M. R. *Chem.-Eur. J.* **2005**, *11*, 2894-2901.

(12) Sun, Z. C.; Wei, Z.; Wei, K. M. *Prog. Biochem. Biophys.* **2008**, *35*, 598-601.

(13) Tetala, K. K. R.; Giesbers, M.; Visser, G. M.; Sudholter, E. J. R.; van Beek, T. A. *Nat. Prod. Commun.* **2007**, *2*, 391-394.

(14) Osborn, H. M. I.; Evans, P. G.; Gemmell, N.; Osborne, S. D. *J. Pharm. Pharmacol.* **2004**, *56*, 691-702.

(15) Mann, D. A.; Kanai, M.; Maly, D. J.; Kiessling, L. L. *J. Am. Chem. Soc.* **1998**, *120*, 10575-10582.

(16) Varki, A. *Glycobiology* **1993**, *3*, 97-130.

(17) Drickamer, K.; Taylor, M. E. *Annu. Rev. Cell Biol.* **1993**, *9*, 237-264.

(18) WHO 2005.

(19) Neidhardt, F. C.; Ingraham, J. L.; Schaechter, M. *Physiology of the bacterial cell: A molecular approach*; Sinauer Associates, Inc.: Sunderland, 1990.

(20) Cygler, M.; Rose, D. R.; Bundle, D. R. *Science* **1991**, *253*, 442-445.

(21) Brockman, J. M.; Nelson, B. P.; Corn, R. M. *Annu. Rev. Phys. Chem.* **2000**, *51*, 41-63.

(22) Homola, J. *Anal. Bioanal. Chem.* **2003**, *377*, 528-539.

(23) Meikle, P. J.; Bundle, D. R. *Glycoconjugate J.* **1990**, *7*, 207-218.

(24) Bundle, D. R.; Eichler, E.; Gidney, M. A. J.; Meldal, M.; Ragauskas, A.; Sigurskjold, B. W.; Sinnott, B.; Watson, D. C.; Yaguchi, M.; Young, N. M. *Biochemistry* **1994**, *33*, 5172-5182.

(25) Otamiri, M.; Nilsson, K. G. I. *Int. J. Biol. Macromol.* **1999**, *26*, 263-268.

(26) MacKenzie, C. R.; Hirama, T.; Deng, S. J.; Bundle, D. R.; Narang, S. A.; Young, N. M. *J. Biol. Chem.* **1996**, *271*, 1527-1533.

(27) Yonzon, C. R.; Jeoungf, E.; Zou, S. L.; Schatz, G. C.; Mrksich, M.; Van Duyne, R. P. *J. Am. Chem. Soc.* **2004**, *126*, 12669-12676.

(28) Blanco, J. L. J.; Haseley, S. R.; Kamerling, J. P.; Vliegenthart, J. F. G. *Biochimie* **2001**, *83*, 653-658.

(29) Duverger, E.; Frison, N.; Roche, A. C.; Monsigny, M. *Biochimie* **2003**, *85*, 167-179.

(30) Smith, E. A.; Thomas, W. D.; Kiessling, L. L.; Corn, R. M. *J. Am. Chem. Soc.* **2003**, *125*, 6140-6148.

(31) Suda, Y.; Arano, A.; Fukui, Y.; Koshida, S.; Wakao, M.; Nishimura, T.; Kusumoto, S.; Sobel, M. *Bioconjugate Chem.* **2006**, *17*, 1125-1135.

(32) Horan, N.; Yan, L.; Isobe, H.; Whitesides, G. M.; Kahne, D. *Proc. Natl. Acad. Sci. U.S.A.* **1999**, *96*, 11782-11786.

(33) Wakao, M.; Saito, A.; Ohishi, K.; Kishimoto, Y.; Nishimura, T.; Sobel, M.; Suda, Y. *Bioorg. Med. Chem. Lett.* **2008**, *18*, 2499-2504.

(34) Karamanska, R.; Clarke, J.; Blixt, O.; MacRae, J. I.; Zhang, J. Q.; Crocker, P. R.; Laurent, N.; Wright, A.; Flitsch, S. L.; Russell, D. A.; Field, R. A. *Glycoconjugate J* **2008**, *25*, 69-74.

(35) de Boer, A. R.; Hokke, C. H.; Deelder, A. M.; Wuhrer, M. *Glycoconjugate J* **2008**, *25*, 75-84.

(36) Kanda, V.; Kitov, P.; Bundle, D. R.; McDermott, M. T. *Anal. Chem.* **2005**, *77*, 7497-7504.

(37) Yu, H. N.; Ling, C. C.; Bundle, D. R. *Can. J. Chem.* **2002**, *80*, 1131-1140.

(38) Nelson, B. P.; Frutos, A. G.; Brockman, J. M.; Corn, R. M. *Anal. Chem.* **1999**, *71*, 3928-3934.

(39) Green, J. B. D.; McDermott, M. T.; Porter, M. D.; Siperko, L. M. *J. Phys. Chem.* **1995**, *99*, 10960-10965.

(40) Verma, N.; Reeves, P. *J. Bacteriol.* **1989**, *171*, 5694-5701.

(41) Nuzzo, R. G.; Allara, D. L. *J. Am. Chem. Soc.* **1983**, *105*, 4481-4483.

(42) Porter, M. D.; Bright, T. B.; Allara, D. L.; Chidsey, C. E. D. *J. Am. Chem. Soc.* **1987**, *109*, 3559-3568.

(43) Bain, C. D.; Troughton, E. B.; Tao, Y. T.; Evall, J.; Whitesides, G. M.; Nuzzo, R. G. *J. Am. Chem. Soc.* **1989**, *111*, 321-335.

(44) Bain, C. D.; Evall, J.; Whitesides, G. M. *J. Am. Chem. Soc.* **1989**, *111*, 7155-7164.

(45) Nuzzo, R. G.; Dubois, L. H.; Allara, D. L. *J. Am. Chem. Soc.* **1990**, *112*, 558-569.

(46) Barrett, D. A.; Power, G. M.; Hussain, M. A.; Pitfield, I. D.; Shaw, P. N.; Davies, M. C. *J. Sep. Sci.* **2005**, *28*, 483-491.

(47) Andrade, J.; Hlady, V. In *Biopolymers/Non-Exclusion HPLC* 1986, p 1-63.

(48) Sigurskjold, B. W.; Altman, E.; Bundle, D. R. *Eur. J. Biochem.* **1991**, *197*, 239-246.

(49) Sigurskjold, B. W.; Bundle, D. R. *J. Biol. Chem.* **1992**, *267*, 8371-8376.

(50) Houseman, B. T.; Mrksich, M. *Angew. Chem., Int. Ed.* **1999**, *38*, 782-785.

(51) Prime, K. L.; Whitesides, G. M. *J. Am. Chem. Soc.* **1993**, *115*, 10714-10721.

(52) Kanda, V. K., PhD, University of Alberta, 2004.

(53) Rodbard, D.; Hutt, D. M. *Radioimmunoassay and Related Procedures in Medicine*; IAEA: Vienna, 1974; Vol. 1.

(54) Danson, R. E. a. M. J. *Enzyme Assays: A Practical Approach*; 2nd ed. New York, 1993.

(55) Spinke, J.; Liley, M.; Guder, H. J.; Angermaier, L.; Knoll, W. *Langmuir* **1993**, *9*, 1821-1825.

(56) Bertilsson, L.; Liedberg, B. *Langmuir* **1993**, *9*, 141-149.

(57) Snyder, R. G.; Maroncelli, M.; Strauss, H. L.; Hallmark, V. M. *J. Phys. Chem.* **1986**, *90*, 5623-5630.

(58) Snyder, R. G.; Strauss, H. L.; Elliger, C. A. *J. Phys. Chem.* **1982**, *86*, 5145-5150.

(59) Bain, C. D.; Biebuyck, H. A.; Whitesides, G. M. *Langmuir* **1989**, *5*.

(60) Bain, C. D.; Whitesides, G. M. *J. Am. Chem. Soc.* **1989**, *111*, 7164-7175.

(61) Folkers, J. P.; Laibinis, P. E.; Whitesides, G. M. *Langmuir* **1992**, *8*, 1330-1341.

(62) Laibinis, P. E.; Nuzzo, R. G.; Whitesides, G. M. *J. Phys. Chem.* **1992**, *96*, 5097-5105.

(63) Stranick, S. J.; Parikh, A. N.; Tao, Y.-T.; Allara, D. L.; Weiss, P. S. *J. Phys. Chem.* **1994**, *98*, 7636-7646.

(64) Bain, C. D.; Whitesides, G. M. *J. Am. Chem. Soc.* **1988**, *110*, 3665-3666.

(65) Brigss, D.; Seah, M. P. *Practical Surface Analysis*; Wiley: Chichester, 1983.

(66) Kanda, V. K. PhD, University of Alberta, 2004.

(67) Frisbie, C. D.; Rozsnyai, L. F.; Noy, A.; Wrighton, M. S.; Lieber, C. M. *Science* **1994**, *265*, 2071-2074.

(68) Noy, A.; Frisbie, C. D.; Rozsnyai, L. F.; Wrighton, M. S.; Lieber, C. M. *J. Am. Chem. Soc.* **1995**, *117*, 7943-7951.

(69) Noy, A.; Vezenov, D. V.; Lieber, C. M. *Annu. Rev. Mater. Sci.* **1997**, *27*, 381-421.

(70) Mammen, M.; Choi, S. K.; Whitesides, G. M. *Angew. Chem., Int. Ed.* **1998**, *37*, 2755-2794.

Chapter 3:

Tailoring Interfacial Chemistry for Antibody Immobilization in Surface Plasmon Resonance (SPR) Immunoassays

3.1 INTRODUCTION

The high specificity and improved ability to generate antibodies against a vast number of antigens has resulted in a continuous growth in their conjugation to surfaces and use as an interfacial recognition layer. Applications for these devices include environmental testing,[1] medical diagnostics,[2,3] and national defense.[4] A literature survey of the first eight months of 2008 revealed studies employing surface plasmon resonance (SPR) for development of immunoassay based arrays against narcotics,[5] small molecules,[6,7] protein-DNA interactions in nuclear extracts,[8] protein kinase activity in cell lysates,[9] and human IgE and aptamers.[10] A vital aspect in the development of these solid-phase assays is the linkage of an antibody to a solid support. This linkage should provide a stable attachment while retaining the biological activity of the antibody. Generally speaking the surface attachment of an antibody may be divided into three groups consisting of physical adsorption, covalent attachment, and affinity capture.

The physical adsorption of an antibody provides a straightforward and facile means to modify a solid support for bio-sensing applications. In this method a solution containing antibody is placed in contact with a surface to promote surface adsorption. The adsorption is the result of various interactions between the surface, protein, and solvent.[11,12] The process is believed to involve both protein binding and unfolding with the extent of each dictated by the interfacial properties of the adsorbing layer.[13]

Concerns over the stability of a physically adsorbed antibody layer have resulted in the investigation of covalent attachment schemes.[14-17] These potentially provide a more stable surface attachment by increasing the strength of the interaction between the surface and the antibody. Methods exist to facilitate either random or orientated antibody layers. Orientation of the antibody typically requires additional steps to modify the antibody. Modifications include the oxidation of carbohydrate groups for binding to a hydrazine surface, or enzymatic cleavage to expose thiol groups in the hinge region for binding to a maleimide surface.[18] A simplified alternative, which produces a random orientation, alleviates any modification steps by directly bonding the antibody to an activated surface. This method was used in this work and involves the formation of an amide bond between free amines in the antibody and an activated succinimydl ester functionality on the surface. In this reaction the primary amine in the antibody reacts via nucleophilic displacement of the N-hydroxysuccinimide (NHS) ester, forming a covalent amide bond.[18]

Affinity capture of an antibody results in the specific orientation of the molecule through selective binding. The specificity is based on a high affinity or selective interaction between a surface bound species and an antibody. The attachments involve both modified and unmodified antibodies with examples such as the attachment of biotinylated modified antibody to a streptavidin surface and binding of unmodified antibody to a layer of protein G. Protein G is a 65 kDa bacterial cell wall protein from group G streptococci that preferentially binds the constant portion (F_c) of the antibody, directing the paratopes away from the surface.[19-24]

Given the vital nature of the surface attachment processes mentioned above, it is not surprising that there are a great number of papers in this area.[11-14,17,25-49] SPR in particular has been used to examine the implications of interfacial chemistry on antibody immobilization and assay performance.[14,28,31,39] While these studies provided valuable insight into aspects of the implications of the antibody immobilization chemistry on assay performance, they did not incorporate examples from all three antibody attachment groups and little was done to optimize the conditions prior to comparison.

In this chapter, self-assembled monolayers (SAMs) of alkanethiolates on gold will be used to tailor interfacial chemistry and examine the impact of surface chemistry on antibody immobilization. The self-assembly of alkanethiolates on gold has been widely used to manipulate interfacial chemistry owing to the well studied and characterized monolayer produced by this adsorbate-substrate combination.[50-56] The availability of alkanethiolates with numerous terminal functional groups permits the formation of well-ordered interfaces with a defined chemistry that has been used to study the interfacial chemistry of protein adsorption.[57,58]

Physical adsorption will be examined on carboxylic acid, methyl, and amine terminated surfaces. Covalent attachment will be evaluated on surfaces formed by the self-assembly of an NHS terminated thiol and also by activating an

11-mercapto-undecanoic acid (MUA) surface using N-(3-dimethylaminopropyl)-N'-ethylcarbodiimide hydrochloride (EDC) and NHS. Affinity capture will be investigated by covalently immobilizing protein G at different pH values and examining the impact of antigen binding following antibody-protein G complex formation. The optimum conditions within each type of attachment chemistry will be selected for further comparisons on retained binding activity and stability of the antibody following surface adsorption.

3.2 EXPERIMENTAL

Material and Methods. Chemicals were obtained from the following sources: N-(3-dimethylaminopropyl)-N'-ethylcarbodiimide hydrochloride (EDC), N-hydroxysuccinimide (NHS), 11-mercapto-undecanoic acid, 1-undecanethiol, ethanolamine, bovine serum albumin (BSA), and protein G were purchased from Aldrich (St. Louis, MO). Hydrogen peroxide and sodium phosphate monobasic monohydrate were purchased from Fisher (Fair Lawn, NJ). Sodium phosphate dibasic heptahydrate, and sodium chloride were purchased from EMD Chemicals Inc. (Darmstadt, Germany). All IgG molecules used in this work were polyclonal. The anti-rabbit IgG (a-rIgG) and rabbit IgG (rIgG) were raised in goat, and anti-goat IgG (a-gIgG) and goat IgG (gIgG) was raised in rabbit. These IgGs were purchased from MP Biomedicals (Solon, OH). Hexanes and sulfuric acid were purchased from Caledon Laboratories Ltd. (Georgetown, Ont.). 11-Amino-1-undecanethiol (AUT), hydrochloride was purchased from Dojindo Laboratories (Japan). N-hydroxysuccinimidyl 12-mercaptododecanoate was purchased from

ProChimia Surfaces (Poland). 1-(mercaptoundec-11-yl)tri(ethylene glycol) methyl ether was synthesized by a previous group member[59] using a published method.[60] Tridecafluoro-1,1,2,2-tetrahydrooctyl-1-trichlorosilane (United Chemical Technologies, Inc.). Anhydrous ethyl alcohol was purchased from Commercial Alcohols (Brampton, Ont.). Water used was 18 MΩ deionized water using a Nanopure filtration system. Polydimethylsiloxane (PDMS) was made using a Sylgard 184 Silicone Elastomer Kit from Dow Corning (Midland, MI).

Surface Modification. Prior to use SPR chips were rinsed with 18 MΩ water and anhydrous ethanol and dried under argon gas, placed in a UVO-cleaner (Jelight Company, California) for five minutes, followed by another water and ethanol rinse and drying under argon gas. The surfaces were then immersed in 1 mM alkanethiolate solutions from overnight to several days to allow the formation of well ordered SAMs. Proteins were then patterned using poly(dimethylsiloxane) (PDMS) microfluidic devices or with a hand-held micropipet.

PDMS microfluidic channels were fabricated using previously established methods.[61] The procedure involved the photolithographic creation of a relief pattern in photoresist on a silicon wafer. The prepolymer and cross-linker (10:1 by weight) were cured against the relief structure producing a negative of the relief within the PDMS. Solution inlet and outlet holes were punctured through the PDMS and the solutions were drawn through by application of a vacuum line to the solution outlet port (Figure 3.01). Following incubation with protein solution the channels were rinsed with buffer, the PDMS device removed, and the surface of the array was rinsed with 18 M MΩ deionized water.

A hand-held micropipet was used to deliver 600 nL of protein solution to an array of gold spots (d = 1mm). The glass between the spots has been rendered hydrophobic by reaction with a fluorinated trichlorosilane (Tridecafluoro-1,1,2,2-tetrahydrooctyl-1-trichlorosilane) under vacuum overnight. This permits the localization of the aqueous based solutions on the gold spots.

Surface Plasmon Resonance (SPR) Imaging. Experiments were carried out using a SPR Imager II, a commercially available system from GWC technologies (Madison, WI). The instrumentation was interfaced and controlled with V++ software. The substrates used used were 1.8 cm x 1.8 cm squares of SF-10 glass (Schott, Ont. Canada) modified with a 1nm chromium adhesion layer and 45 nm of gold. Data analysis involved the averaging of 100 images and correction for non-specific adsorption. Images shown were difference images, which were obtained by subtraction of the initial image in buffer from the image taken following incubation with a protein solution and rinsing with buffer.

3.3 RESULTS AND DISCUSSION

Physical Adsorption. A goal of this portion of the work was to examine the impact of interfacial surface chemistry on the orientation and activity of a physically adsorbed antibody layer. These factors were probed indirectly by monitoring antigen binding to antibodies adsorbed on surfaces functionalized with SAMs of alkanethiolates presenting amine ($HS-(CH_2)_{10}-NH_2$), carboxylic acid

($HS-(CH_2)_{10}-COOH$), and methyl ($HS-(CH_2)_{10}-CH_3$) terminal groups. These surface chemistries were chosen as they represent a range of common interfacial chemistries used in surface assays, from hydrophilic to hydrophobic surfaces with varying degrees of charge.

The gold surfaces were first modified with the alkanethiolates followed by adsorption and patterning of two antibodies, anti-rabbit IgG (a-rIgG) along with anti-goat IgG (a-gIgG), which served as a negative control. The antibodies were patterned for one hour within a PDMS microfluidic network, which was then removed. The remaining surface was then blocked with BSA. This procedure is represented in Figure 3.01. At this point the chip was placed into the SPR imaging instrument and the binding from solutions containing 1300 to 1600 nM rabbit IgG (rIgG) was measured. These solution concentrations were chosen as they have been shown to result in saturation coverage.[59] Figure 3.02 presents the SPR difference images (A) and quantitative binding data (B) for the three surfaces.

Antigen (rIgG) binding to the control line (a-gIgG) was used to provide a measure of the non-specific binding occurring on the antibody modified surfaces. These values are presented in Figure 3.02(B) and show that negligible non-specific adsorption occurred to the surface pre-functionalized with an amine terminal group with increased non-specific binding occurring on the carboxylic acid and methyl surfaces. The varying degrees of non-specific binding observed here may be related to surface chemistry dependant conformational changes that occurred to the antibodies upon adsorption.

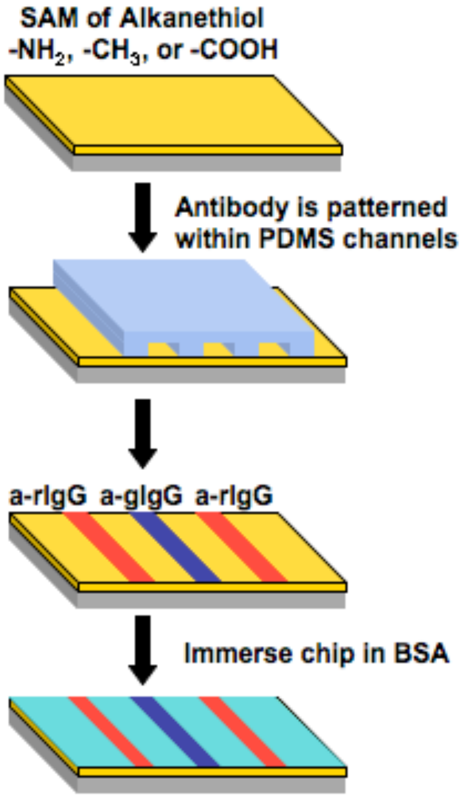

Figure 3.01. Representation of the steps involved with preparation of the surface and antibody adsorption. The process begins with modification of the gold surface using 1 mM alkanthiolate solutions followed by surface patterning of a 3.3 μM specific and control antibody and lastly the blocking of the remaining surface with a 0.1% BSA solution in PBS.

Previous work has shown that interfacial chemistry impacts the degree of protein unfolding, with proteins retaining more structure on neutral hydrophilic surfaces than hydrophobic or charged surfaces.[13] In this study, hydrophilic surfaces were produced upon surface modification with the amine and carboxylic acid terminated SAMs and a neutral hydrophobic surface from the methyl SAM. The extent of ionization on the hydrophilic SAMs can be determined by reviewing the surface pKa values for the ionizable groups present. The pKa for carboxylic acid SAMs has been consistently reported between a pH value of 7-8[40,62-65] and the pKa for amine SAMs has been reported between 4-6.5.[62,66,67] Therefore, under the conditions used in these experiments (PBS pH 7.4) the carboxylic acid surface would exhibit a greater degree of ionization and a net negative surface charge. In relation to the non-specific adsorption data, the least charged hydrophilic surface (-NH_2) provided the smallest amount of non-specific adsorption. This surface likely produced the least unfolding and was able to reduce the non-specific interactions. The carboxyl and methyl terminated surfaces resulted in greater degrees of antibody unfolding/denaturation causing increases in the measured non-specific binding.

The extent of specific antigen binding was determined by subtracting the antigen binding occurring on the control line (a-gIgG) from that occurring on the a-rIgG lines. These values are presented in Figure 3.02(B) and show the amine surface exhibits the greatest amount of specific binding followed closely by the methyl surface and lastly the carboxylic acid surface. These trends are consistent with a previous study examining similar antibody immobilization schemes.[31] In that work, the authors attributed the differences in antigen binding to variations in the orientation of the antibody on the different surfaces. The range of orientations may be represented as in Figure 3.03 where the amine surface preferentially adsorbs the constant portion of the antibody (a), the methyl surface results in a mixture of the antibody lying down and adsorbed through the F_c region (b), and the carboxyl surface favors adsorption of the F_{ab} fragments resulting in a significant reduction in the ability to capture antigen.

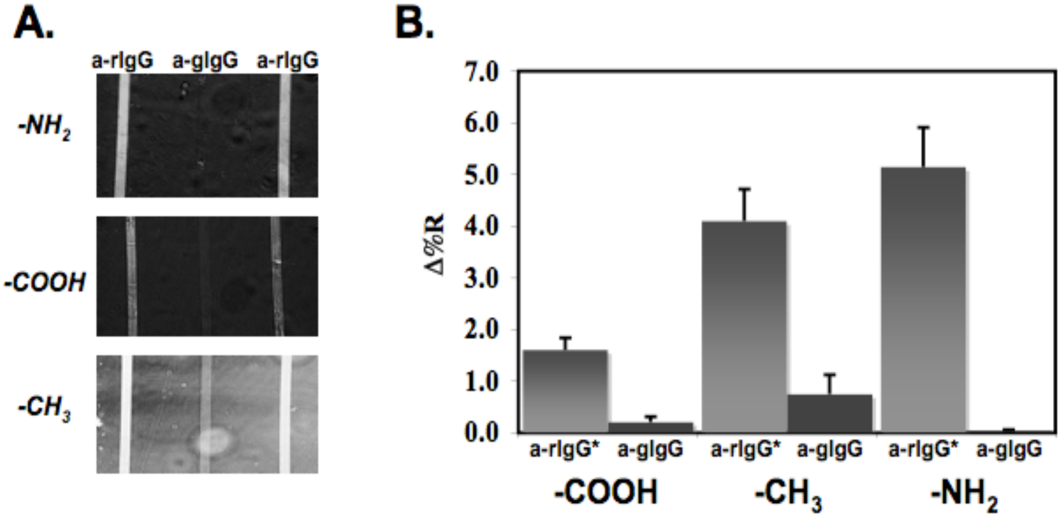

Figure 3.02. (A). The SPR difference images obtained upon incubation with a 1350 nM rIgG solution ($-NH_2$ and -COOH terminated SAMs) or 1650 nM rIgG solution ($-CH_3$ terminated SAM). (B) The Δ%R values obtained from the SPR difference images in (A) from the a-gIgG lines and the a-rIgG. The a-rIgG lines were corrected for non-specific adsorption by subtracting the values from the a-gIgG control line. Error bars represent the standard deviation of the average.

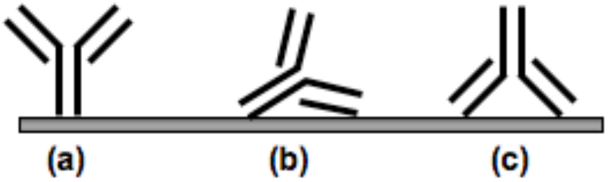

Figure 3.03. Representation of the possible orientations of antibody immobilized on a surface. They represent active (a), partially active (b), and inactive (c) antibodies

In summary, consistent with previous work, our experiments indicate the optimal surface chemistry for physical adsorption of an antibody is an amine-terminated surface. This surface was optimal likely because it results in favorable antibody orientation and presents the least non-specific adsorption. This attachment chemistry was selected for further comparison.

Covalent Attachment. The stability of an adsorbed antibody layer plays a vital role in its performance as a bio-sensing element. While the non-covalent, physical adsorption of an antibody provides a feasible means of surface immobilization, the potential for solvent-mediated desorption exists. Studies have shown that covalently immobilized immunoglobulin demonstrates an increased operational stability.[15-17,68]

A common method employed for the covalent linkage of an antibody to a surface involves the formation of an amide bond between primary amines naturally present in the antibody and a surface bound active ester (e.g., N-hydroxysuccinimide). The methods to create an NHS terminated surface on gold have been well documented and involve two approaches, which are depicted in

Figure 3.04. Perhaps the most common and economical method involves the initial formation of a carboxylic acid terminated SAM, followed by a surface activation reaction using EDC and NHS.[17,48,69] The second approach eliminates the surface activation step by directly assembling an NHS terminated alkanethiolate on the gold surface.[32,49] While these methods have been in practice since the early 1990's there has been no work directly comparing the two methods. Motivated by observations showing that surface reactions result in less than 100% yields, [70,41] we have decided to evaluate the possible implications for incomplete conversion of the carboxylic acid terminal groups.

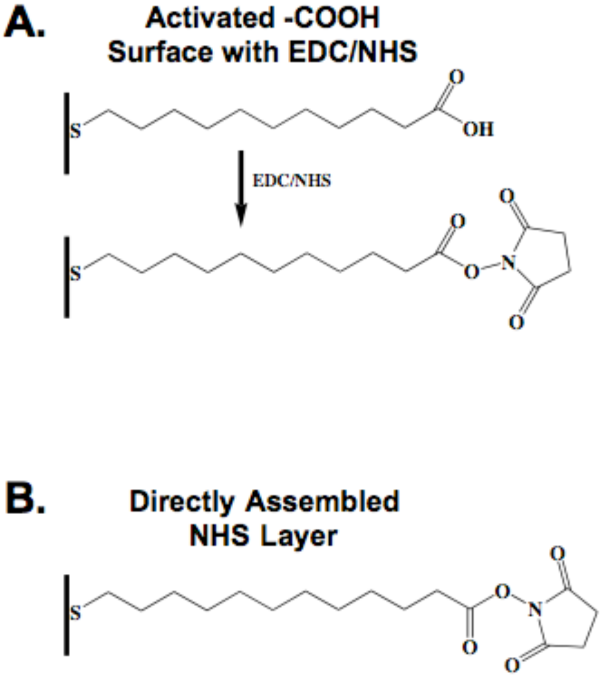

Figure 3.04. Representation for (A) the activation of a carboxylic acid surface using EDC/NHS and (B) direct assembly of an NHS surface.

The protein capacity of both surfaces was determined by monitoring the binding of a 3.3 μM solution of rIgG to the NHS surfaces. The substrates used in this work consisted of a fluorinated SF-10 glass surface with 19 gold spots (diameter = 1 mm). Monolayers were formed by immersion in 1 mM solutions of either MUA or N-hydroxysuccinimidyl 12-mercaptododecanoate. Prior to protein immobilization the MUA surface was activated for 30 minutes by immersion in an aqueous solution of EDC/NHS. A control protein (BSA) was spotted to block 8 spots of the array. Shown in Figure 3.05 is a representative SPR difference image following protein binding and a bar graph presenting the quantitative results from the two surfaces. The activated MUA surface produced a signal over 2.5x smaller than the directly assembled NHS layer. The reduced signal indicates a lower protein capacity possibly due to incomplete conversion of the carboxylic acid groups to NHS. This observation is consistent with results by Frey et al., who examined binding of poly(L-lysine) to an EDC/NHS activated MUA monolayer.[41] The findings indicated that 20% of the initial MUA layer remained unreactive to EDC/NHS conversion.

To further probe possible implications of an inefficient surface reaction, the stability and antigen detection limits for both surfaces were evaluated. Monolayers were prepared as mentioned above, with BSA and a-rIgG solutions spotted on the NHS surfaces. Prior to introduction of antigen, the surfaces were deactivated with 100 mM Tris buffer followed by equilibration for 30 minutes with PBS buffer. The detection limits of the surfaces were then probed by monitoring the binding of pM levels of rIgG.

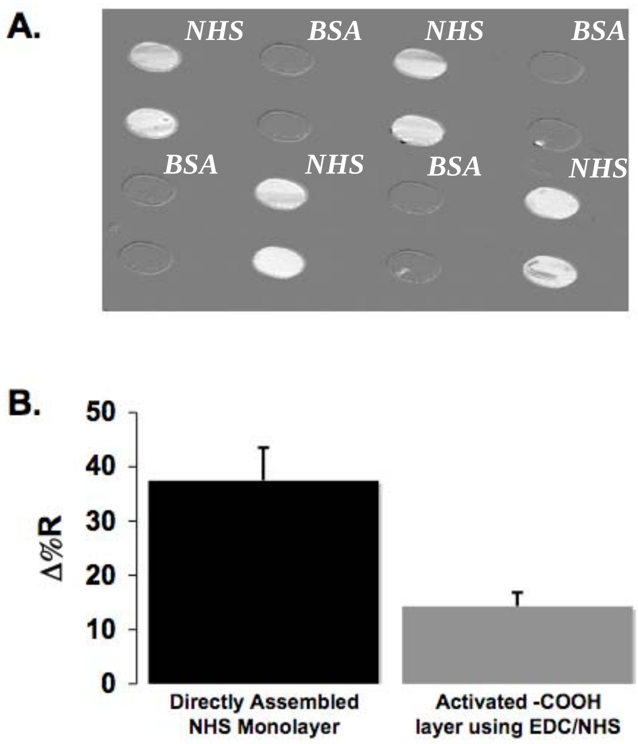

Figure 3.05. A) Representative SPR difference image following adsorption of 6.7 μM rIgG to a directly assembled NHS surface. BSA was used as a control to block 8 spots. B) The Δ%R values from the SPR difference images where the error bars represent the standard deviation for the average values.

The values obtained for antigen binding to the antibody spots were corrected for changes in bulk refractive index and non-specific binding using the BSA control spots. These corrected values are plotted in Figure 3.06 for the activated MUA layer (A) and the directly assembled NHS layer (B). The error bars represent the standard deviation of the mean signal values. The mean values were determined by reproducing the experiment on separate SPR chips on different days. The data was then fit using a linear least squares analysis. The lowest antigen concentration tested (2 or 20 pM) was treated as a blank. The

Δ%R values for the lowest three concentrations tested on an activated –COOH layer are shown in Table 3.1. These values show that increasing the concentration from 20 pM to 50 pM did not statistically increase the observed signal. Therefore, it was assumed that the solution containing the lowest antigen concentration was suitable to be treated as blank. The Δ%R values obtained following incubation with the lowest antigen concentration were used in equation 1 to determine the limit of detection (LOD) for both surfaces tested. The value obtained from equation 1 was converted to a concentration using the linear fit obtained from least squares analysis, shown in Figure 3.06.

$$LOD = 3\sigma_{blank} + blank \qquad (1)$$

Table 3.1. The Δ%R values obtained following incubation with pM levels of antigen with a covalently immobilized antibody layer.

[rIgG] in pM	Δ%R
20	0.09 ± 0.02
50	0.10 ± 0.01
100	0.14 ± 0.01

The LOD for the activated surface was found to be 135 ± 38 pM and the directly assembled NHS surface was a factor of two lower and found to be 77 ± 22 pM. The error was determined by propagating the error associated with the blank measurement through the calculations. Again the requirement of a surface activation step has reduced the performance of the surface assay, with comparable reductions to both the protein capacity and the detection limit. Previous work has shown a relation between the amount of surface bound antibody and/or IgG and the observed signal upon binding of a complementary antigen and/or protein,[71] with larger amounts of surface bound probe capturing more target from solution. In this case the directly assembled surface is able to immobilize more antibody and therefore is able to capture more antigen, providing more sensitive detection. Of note, both detection limits obtained in this work are an order of magnitude lower than any previously reported value of 1-2 nM using SPR detection to directly monitor the label-free binding of an anti-IgG – IgG system.[72]

Further evidence of the differences in the two NHS layers is witnessed when examining the slope of the linear fits in Figure 3.09. The slope of the directly assembled layer is 2x larger than the activated MUA layer. The increased slope results in more sensitive antigen detection. The cause of the increased sensitivity is again likely the increased amount of antibody immobilized to the NHS surface.

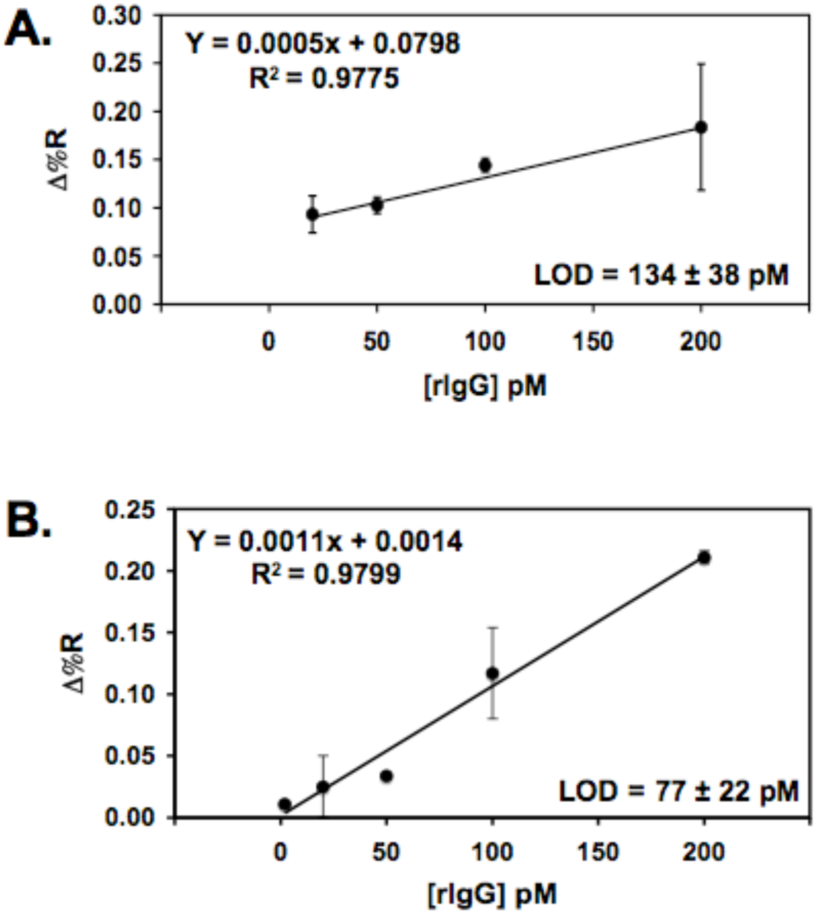

Figure 3.06. Plots of SPR response following incubation with pM levels of rIgG for antibody bound to (A) an activated -COOH surface using EDC/NHS or (B) a directly assembled NHS layer. The error bars represent the standard deviation of the average.

Affinity Capture with Protein G. A critical aspect of immunoassay performance is the orientation and retained biological activity of the antibody sensing layer. Protein G is a bacterial cell wall protein isolated from group G streptococci that has been found to preferentially bind the F_c portion of many IgG's.[20-24] This feature has been used by researchers to obtain an active and orientated antibody layer, with the antigen binding sites directed away from the surface.[28,39,73-76] In my work, Protein G was covalently bound to a directly assembled NHS surface. The pH of the Protein G immobilization buffer was varied to optimize attachment of Protein G and the subsequent performance of the antibody-Protein G surface assay.

The surfaces were modified and patterned as in the previous section and involved modification with a 1 mM solution of NHS terminated thiol. The surface was rinsed and a BSA control and protein G solutions with pH values from 4 to 6.5 were spotted on the SPR chip and left for 1 hour. The saturation of the protein G layer with a-rIgG was determined by incubating the protein G surface with increasing amounts of antibody. It was important to ensure the protein G layer was saturated with antibody because the antigen used in this work is also an IgG, and therefore may bind to protein G. Figure 3.07 plots the fractional coverage (θ) versus the concentration of the antibody. The values for θ were determined from Δ%R values using least squares analysis and a Langmuir model (equation 2). The values were then normalized using the θ_{max} value from the solution to the least squares analysis. Figure 3.07 shows that antibody concentrations above 600 nM saturate the Protein G layer. An antibody concentration of 1300 nM was used for further optimization experiments.

$$\theta = \frac{\theta_{\max}\left[A\right]}{(K_d + [A])} \tag{2}$$

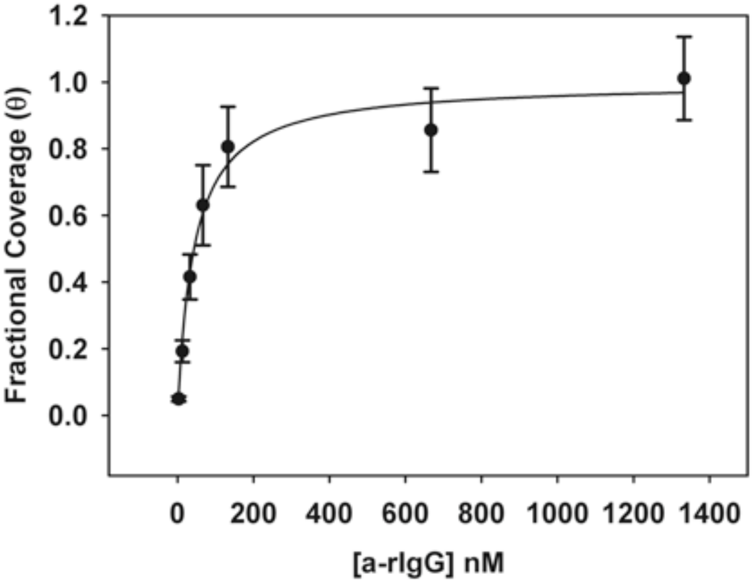

Figure 3.07. Binding curve showing the saturation of a protein G layer with a-rIgG. The solid line represents the line of best fit from the linear regression using equation 2. Error bars represent the standard deviation of the average value reported for each spot of the array surface.

The effect of pH on the conjugation of Protein G to the surface was examined to optimize this immobilization scheme. Performance was monitored by measuring antigen (rIgG) binding to an antibody layer immobilized to Protein G. The Protein G was immobilized at various pH. Figure 3.08 contains SPR signals for antigen binding from a 1650 nM solution. Immobilization of Protein G at pH 4.0 showed the greatest response for antigen binding with a reduced response observed for all other pH values tested. Similar trends have been reported when examining the impact of pH on the amount of protein A bound to an activated carboxymethyldextran surface.[48] This was attributed to more favorable electrostatic attraction between the carboxymethyldextran surface and the Protein A when the pH was reduced. In my work lowering the pH of the Protein G solution to at or below its iso-electric point (4-4.5),[19,77] reduced the potential for unfavorable electrostatic repulsive interactions between Protein G and the surface. The increased amount of Protein G bound to the surface increased the density of antibody immobilized and therefore the amount antigen captured.

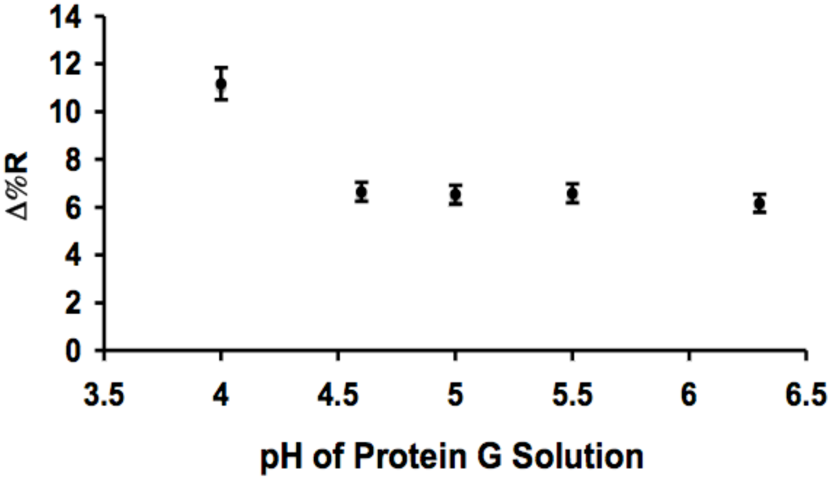

Figure 3.08. Impact of immobilization pH used to link Protein G to NHS surface on the ability of an antibody-protein G complex's ability to capture antigen from solution. Error bars represent the standard deviation of the average value reported for each spot of the array surface.

Comparison of Attachment Chemistries. The three optimized antibody immobilization methods were further evaluated and compared in relation to biological activity and stability of the adsorbed antibody layer. The activity of the immobilized antibody was determined by monitoring the signal change for antibody adsorption followed by antigen capture with SPR imaging. The ratio of these values has commonly been reported as the binding ratio and is a measure of the activity of the antibody layer.[31,37,42] The stability of the surface adsorbed antibody layer was also probed by incubating the antibody modified surfaces with pM levels of antigen and monitoring any signal changes.

The SPR chips were modified using the same protocols mentioned in the above sections. A BSA control was patterned on the functionalized SPR chips blocking half of the spots while leaving 8 spots containing amine, NHS, or NHS-protein G functionalities exposed for antibody immobilization. A 1300 nM antibody (a-rIgG) solution was then introduced to the surface, adsorbed for 30 minutes, and then rinsed with buffer. Figure 3.09 presents the SPR imaging values for antibody immobilization followed by capture of a 1650 nM rIgG antigen on the three surfaces tested. The amine and NHS surfaces captured similarly large amounts of antibody relative to the protein G surface. However, both the amine and NHS pre-functionalized antibody surfaces were significantly less efficient at capturing antigen from solution. The binding ratios are presented in Table 3.2 and are in agreement with those previously reported.[31,33,42]

The immunoassay immobilization platforms were further evaluated by collecting antigen binding curves. The antibody modified surfaces were prepared as described above and incubated with increasing amounts of rIgG, from 2 to 1650 nM. The binding curves are presented in Figure 3.10 where the antigen response has been corrected for non-specific binding and bulk refractive index using the BSA control spots. The solid lines in the plot indicate the fit obtained following least squares analysis with a four parameter logistical model (3) with the fitting parameters presented in Table 3.3. As mentioned in Chapter 2, this equation is commonly used in the analysis and fitting of antigen binding curves and simplifies to the Langmuir when the hill coefficient (b) is one.

$$\Delta\%R = \Delta\%R_{\min} + \frac{\Delta\%R_{\max} - \Delta\%R_{\min}}{1 + \left(\frac{[A]}{K_d}\right)^b} \qquad (3)$$

The differences in antigen capture, Δ%R intensity, for the three antibody immobilization chemistries were consistent with the trends observed above. Briefly, the protein G and physically adsorbed antibody layers capture similar amounts of antigen, although the protein G layer did so in a significantly more efficient manner (larger binding ratio). The reduced performance of the covalently attached layer has been attributed to the poor orientation of the antibody layer, resulting in a reduced ability to bind antigen.

The strength of antigen binding (K_{ADS}) to the antibody surfaces ranges from approximately 8.4 to 25 x 10^7 M^{-1}. The small differences in measured binding affinity suggest similar binding is occurring on all surfaces. The K_{ADS} values reported here are in good agreement with those previously determined for surface based measurements of binding affinity.[71,78] The low b values for the physically adsorbed layer and the covalently linked layer relative to the protein G layer have previously been observed and attributed to an increased heterogeneity of the antibody layers, a consequence of their random orientation.[33] However, it should be noted that extracting physical significance from these values remains speculative.[79]

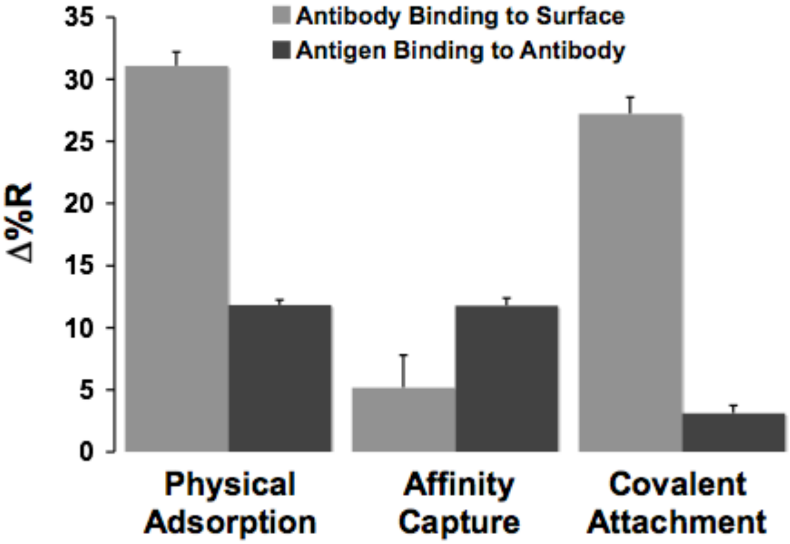

Figure 3.09. SPR Imaging values for the adsorption of the primary antibody layer followed by the signals obtained for capture of antigen by these antibody modified surfaces. The antibody was physical adsorbed to an –NH_2 surface, affinity captured by protein G immobilized at pH 4.0, and covalently attached to a directly assembled –NHS surface.

Table 3.2. Binding ratios for antibody bound via different surface chemistries. The binding ratio represents the ratio of the amount of antibody bound relative to the amount of antigen captured.

Initial Surface	Antibody Binding (Δ%R)	Antigen Binding (Δ%R)	Binding Ratio
-NH_2	31 ± 1	11.8 ± 0.4	0.38 ± 0.02
-NHS + Protein G[a]	5 ± 3	11 ± 0.6	2 ± 1
-NHS	27 ± 1	3.1 ± 0.6	0.1 ± 1.0

a. Protein G immobilized at pH 4.0

The stability of these three surfaces was also tested in an attempt to evaluate the detection limit of the antibody modified surfaces. The immobilized antigen layers were incubated for five minutes in pM levels of rIgG followed by a buffer rinse. The values obtained on the antibody spots were again corrected using the BSA control spots and are presented in the Figure 3.11. The amine and protein G antibody modified surfaces showed negative values upon incubation with pM levels of rIgG while the covalently attached antibody showed a small positive value. The negative Δ%R values indicate a loss of material from the surface, likely a result of solvent mediated desorption of the antibody. Research by Ball *et al.*[46] and Lutanie *et al.*[80] in the early 1990's has described the surface desorption of a physically adsorbed protein. Even though the equilibrium for the surface adsorption of the antibody to the amine and protein G surfaces most likely significantly favors adsorption, the reverse reaction is also possible. Therefore, the instability of these layers relative to the covalently attached antibody will not permit the probing of pM levels of antigen.

Under the conditions tested there appears to be a trade-off between sensitivity and detection limits. The physically adsorbed and protein G layers provide greater signals upon antigen binding, resulting in more sensitive measurements of antigen. However, the covalently attached layer provides a stable sensing layer that is not susceptible to solvent mediated desorption, allowing the probing of pM levels of antigen not possible with the other surfaces.

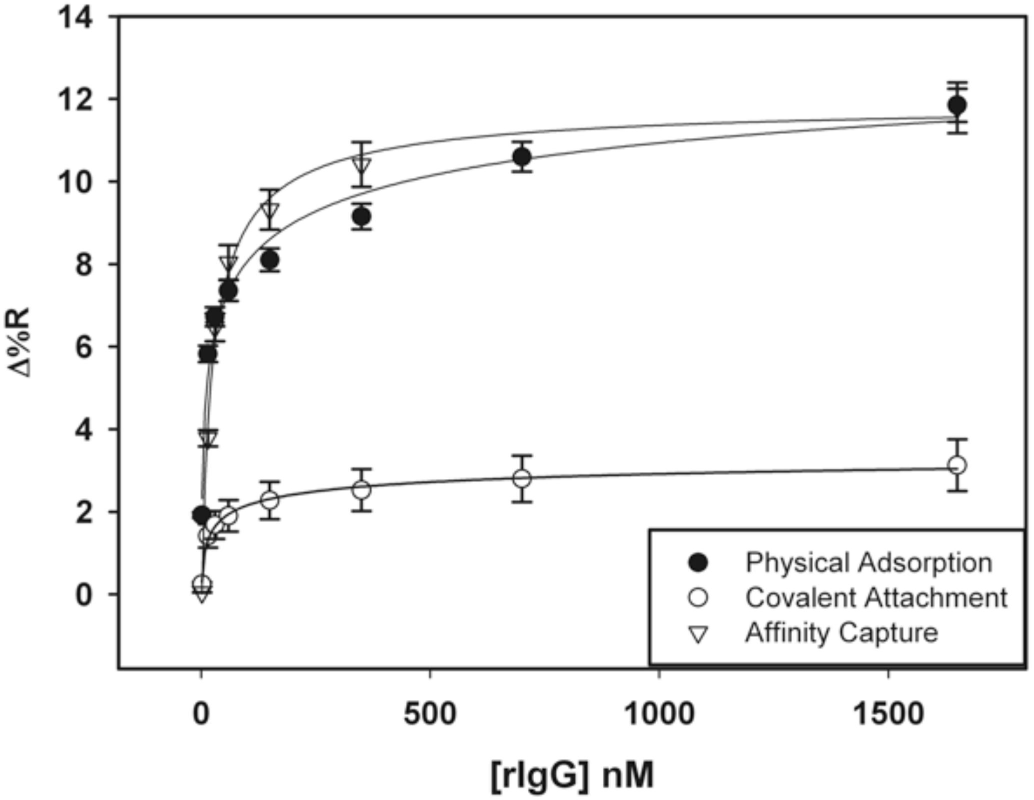

Figure 3.10. Rabbit IgG (rIgG) binding curves obtained under varying antibody immobilization chemistries. The primary antibody layer (a-rIgG) was formed by physical adsorption to an amine thiol monolayer, direct covalent attachment to an NHS monolayer, or affinity capture through a covalently bound protein G layer. Error bars represent the standard deviation of the measurement (n=8). Solid lines are the curve fits obtained using a four-parameter logistical model.

Table 3.3. Curve fitting parameters for antigen binding curves obtained on antibody modified surfaces. Errors represent the uncertainties of the derived fit.

Antibody Attachment	**R^2**	**K_{ADS} (M^{-1})**	**Min.**	**Max.**	**b**
affinity capture	0.995	4.8 ± 0.7 x 10^7	-1.8 ± 0.2	12.0 ± 0.5	-0.80 ± 0.09
physical adsorption	0.980	8 ± 12 x 10^7	-6.7 ± 0.3	16.6 ± 4.2	-0.26 ± 0.08
covalent attachment	0.994	25 ± 9 x 10^7	-2.6 ± 0.1	3.9 ± 0.3	-0.31 ± 0.04

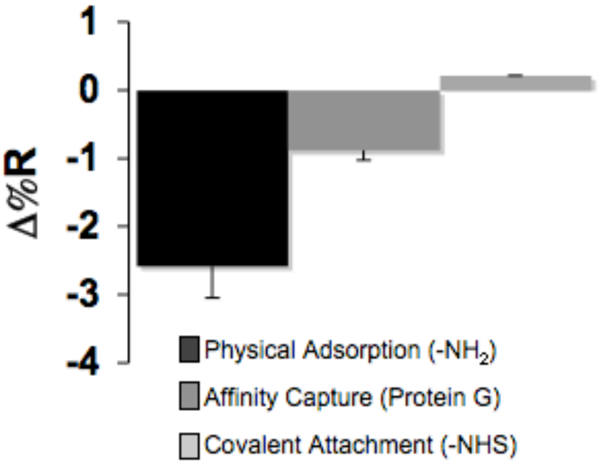

Figure 3.11. SPR imaging values following incubation of the antibody modified surfaces in 200 - 400 pM rIgG solutions. Affinity capture and covalent attachment were incubated in 200 pM and physically adsorbed layer was in 400 pM rIgG. Values were obtained following a 5 minute incubation in rIgG followed by a buffer rinse.

3.4 CONCLUSIONS

A detailed investigation on the impact of antibody immobilization chemistry on assay performance was presented. Initial screening involved the preliminary optimization of surface chemistries for physical adsorption, covalent attachment, and affinity capture of an antibody. The optimum conditions from each category of these surface chemistries was then selected for further comparisons including the activity and stability of the antibody layer. Affinity capture with protein G and physical adsorption of the antibody provided the greatest signals upon antigen capture. However, the instability of these layers, a consequence of solvent mediated desorption of the primary antibody, resulted in an inability to probe pM levels of antigen. In contrast to those layers, the covalently attached antibody layer produced a stable antibody attachment with a detection limit of 77 ± 22 pM, an order of magnitude lower than previously reported values of 1-2 nM.[72]

3.5 REFERENCES

(1) Tschmelak, J.; Proll, G.; Riedt, J.; Kaiser, J.; Kraemmer, P.; Barzaga, L.; Wilkinson, J. S.; Hua, P.; Hole, J. P.; Nudd, R.; Jackson, M.; Abuknesha, R.; Barcelo, D.; Rodriguez-Mozaz, S.; De Alda, M. J. L.; Sacher, F.; Stien, J.; Slobodnik, J.; Oswald, P.; Kozmenko, H.; Korenkova, E.; Tothova, L.; Krascsenits, Z.; Gauglitzi, G. *International J. Environ. Anal. Chem.* **2005**, *85*, 837-852.

(2) Hartmann, M.; Roeraade, J.; Stoll, D.; Templin, M.; Joos, T. *Anal. Bioanal. Chem.* **2009**, *393*, 1407-1416.

(3) Ling, M. M.; Ricks, C.; Lea, P. *Expert Review of Molecular Diagnostics* **2007**, *7*, 87-98.

(4) Wang, H.; Wang, J.; Timchalk, C.; Lin, Y. H. *Anal. Chem.* **2008**, *80*, 8477-8484.

(5) Klenkar, G.; Liedberg, B. *Anal. Bioanal. Chem.* **2008**, *391*, 1679-1688.

(6) Kim, S. J.; Gobi, K. V.; Tanaka, H.; Shoyama, Y.; Miura, N. *Sensor Actuator B Chem.* **2008**, *130*, 281-289.

(7) Taylor, A. D.; Ladd, J.; Etheridge, S.; Deeds, J.; Hall, S.; Jiang, S. Y. *Sensor Actuator B Chem.* **2008**, *130*, 120-128.

(8) Su, X. D.; Neo, S. J.; Peh, W. Y. X.; Thomsen, J. S. *Anal. Biochem.* **2008**, *376*, 137-143.

(9) Mori, T.; Inamori, K.; Inoue, Y.; Han, X.; Yamanouchi, G.; Niidome, T.; Katayama, Y. *Anal. Biochem.* **2008**, *375*, 223-231.

(10) Wang, J. L.; Lv, R. J.; Xu, J. J.; Xu, D. K.; Chen, H. Y. *Anal. Bioanal. Chem.* **2008**, *390*, 1059-1065.

(11) Haynes, C. A.; Norde, W. *Colloids and Surfaces B: Biointerfaces* **1994**, *2*, 517-566.

(12) Hlady, V.; Buijs, J. *Curr. Opin. Biotechnol.* **1996**, *7*, 72-77.

(13) Gray, J. J. *Curr. Opin. Struct. Biol.* **2004**, *14*, 110-115.

(14) Disley, D. M.; Cullen, D. C.; You, H.-X.; Lowe, C. R. *Biosensor Bioelectron.* **1998**, *13*, 1213-1225.

(15) Lundstrom, I. *Biosensor Bioelectron.* **1994**, *9*, 725-736.

(16) Carome, E. F.; Coghlan, G. A.; Sukenik, C. N.; Zull, J. E. *Sensor Actuator B Chem.* **1993**, *14*, 732-733.

(17) Lofas, S.; Johnsson, B. *J. Chem. Soc. Chem. Comm.* **1990**, 1526-1528.

(18) Hermanson, G. T. *Bioconjugate Techniques*; Second ed.; Academic Press: Amsterdam, 2008.

(19) Sauereriksson, A. E.; Kleywegt, G. J.; Uhl, M.; Jones, T. A. *Structure* **1995**, *3*, 265-278.

(20) Kato, K.; Lian, L. Y.; Barsukov, I. L.; Derrick, J. P.; Kim, H. H.; Tanaka, R.; Yoshino, A.; Shiraishi, M.; Shimada, I.; Arata, Y.; Roberts, G. C. K. *Structure* **1995**, *3*, 79-85.

(21) Sjobring, U.; Bjorck, L.; Kastern, W. *J. of Biol. Chem.* **1991**, *266*, 399-405.

(22) Stone, G. C.; Sjobring, U.; Bjorck, L.; Sjoquist, J.; Barber, C. V.; Nardella, F. A. *J. Immunol.* **1989**, *143*, 565-570.

(23) Akerstrom, B.; Bjorck, L. *J. Biol. Chem.* **1986**, *261*, 240-247.

(24) Akerstrom, B.; Brodin, T.; Reis, K.; Bjorck, L. *J. Immunol.* **1985**, *135*, 2589-2592.

(25) Cecchet, F.; Duwez, A. S.; Gabriel, S.; Jerome, C.; Jerome, R.; Glinel, K.; Demoustier-Champagne, S.; Jonas, A. M.; Nysten, B. *Anal. Chem.* **2007**, *79*, 6488-6495.

(26) Xu, H.; Zhao, X. B.; Grant, C.; Lu, J. R.; Williams, D. E.; Penfold, J. *Langmuir* **2006**, *22*, 6313-6320.

(27) Xu, H.; Williams, D. E.; Lu, J. R. *Prog. Nat. Sci.* **2005**, *15*, 139-144.

(28) Bae, Y. M.; Oh, B.-K.; Lee, W.; Lee, W. H.; Choi, J.-W. *Biosensor Bioelectron* **2005**, *21*, 103-110.

(29) Wang, H.; Castner, D. G.; Ratner, B. D.; Jiang, S. Y. *Langmuir* **2004**, *20*, 1877-1887.

(30) Zhou, J.; Chen, S. F.; Jiang, S. Y. *Langmuir* **2003**, *19*, 3472-3478.

(31) Chen, S.; Liu, L.; Zhou, J.; Jiang, S. *Langmuir* **2003**, *19*, 2859-2864.

(32) Neubert, H.; Jacoby, E. S.; Bansal, S. S.; Iles, R. K.; Cowan, D. A.; Kicman, A. T. *Anal. Chem.* **2002**, *74*, 3677-3683.

(33) Vijayendran, R. A.; Leckband, D. E. *Anal. Chem.* **2001**, *73*, 471-480.

(34) Bergkvist, M.; Carlsson, J.; Oscarsson, S. *J. Phys. Chem. B* **2001**, *105*, 2062-2069.

(35) Rao, S. V.; Anderson, K. W.; Bachas, L. G. *Mikrochimica Acta* **1998**, *128*, 127-143.

(36) Edmiston, P. L.; Lee, J. E.; Cheng, S. S.; Saavedra, S. S. *J. Am. Chem. Soc.* **1997**, *119*, 560-570.

(37) Buijs, J.; White, D. D.; Norde, W. *Colloids and Surfaces B-Biointerfaces* **1997**, *8*, 239-249.

(38) Lu, B.; Smyth, M. R.; Okennedy, R. *Analyst* **1996**, *121*, R29-R32.

(39) Klonisch, T.; Panayotou, G.; Edwards, P.; Jackson, A. M.; Berger, P.; Delves, P. J.; Lund, T.; Roitt, I. M. *Immunology* **1996**, *89*, 165-171.

(40) Godinez, L. A.; Castro, R.; Kaifer, A. E. *Langmuir* **1996**, *12*, 5087-5092.

(41) Frey, B. L.; Corn, R. M. *Anal. Chem.* **1996**, *68*, 3187-3193.

(42) Caruso, F.; Rodda, E.; Furlong, D. N. *J. Colloid Interface Sci.* **1996**, *178*, 104-115.

(43) Scouten, W. H.; Luong, J. H. T.; Brown, R. S. *Trends Biotechnol.* **1995**, *13*, 178-185.

(44) Ramsden, J. J. *Chem. Soc. Rev.* **1995**, *24*, 73-78.

(45) Buijs, J.; Lichtenbelt, J. W. T.; Norde, W.; Lyklema, J. *Colloids and Surfaces B-Biointerfaces* **1995**, *5*, 11-23.

(46) Ball, V.; Huetz, P.; Elaissari, A.; Cazenave, J.; Voegel, J.; Schaff, P. *Proc. Natl. Acad. Sci.* **1994**, *91*, 7330-7334.

(47) Lu, D. R.; Lee, S. J.; Park, K. *J. Biomater. Sci. Polymer Ed.* **1991**, *3*, 127-147.

(48) Johnsson, B.; Lofas, S.; Lindquist, G. *Anal. Biochem.* **1991**, *198*, 268-277.

(49) Katz, E. Y. *J. Electroanal. Chem.* **1990**, *291*, 257-260.

(50) Nuzzo, R. G.; Dubois, L. H.; Allara, D. L. *J. Am. Chem. Soc.* **1990**, *112*, 558-569.

(51) Bain, C. D.; Troughton, E. B.; Tao, Y. T.; Evall, J.; Whitesides, G. M.; Nuzzo, R. G. *J. Am. Chem. Soc.* **1989**, *111*, 321-335.

(52) Bain, C. D.; Biebuyck, H. A.; Whitesides, G. M. *Langmuir* **1989**, *5*.

(53) Bain, C. D.; Whitesides, G. M. *J. Am. Chem. Soc.* **1988**, *110*, 3665-3666.

(54) Porter, M. D.; Bright, T. B.; Allara, D. L.; Chidsey, C. E. D. *J. Am. Chem. Soc.* **1987**, *109*, 3559-3568.

(55) Nuzzo, R. G.; Fusco, F. A.; Allara, D. L. *J. Am. Chem. Soc.* **1987**, *109*, 2358-2368.

(56) Nuzzo, R. G.; Allara, D. L. *J. Am. Chem. Soc.* **1983**, *105*, 4481-4483.

(57) Ta, T. C.; McDermott, M. T. *Anal. Chem.* **2000**, *72*, 2627-2634.

(58) Prime, K. L.; Whitesides, G. M. *Science* **1991**, *252*, 1164-1167.

(59) Kanda, V. K. PhD, University of Alberta, 2004.

(60) Pale-Grosdemange, C.; Simon, E. S.; Prime, K. L.; Whitesides, G. M. *J. Am. Chem. Soc.* **1991**, *113*, 12-20.

(61) Xia, Y. N.; Whitesides, G. M. *Angew. Chem., Int. Ed.* **1998**, *37*, 551-575.

(62) Fears, K. P.; Creager, S. E.; Latour, R. A. *Langmuir* **2008**, *24*, 837-843.

(63) Kakiuchi, T.; Iida, M.; Imabayashi, S. i.; Niki, K. *Langmuir* **2000**, *16*, 5397-5401.

(64) Hu, K.; Bard, A. J. *Langmuir* **1997**, *13*, 5114-5119.

(65) Bain, C. D.; Whitesides, G. M. *Langmuir* **1989**, *5*, 1370-1378.

(66) Bryant, M. A.; Crooks, R. M. *Langmuir* **1993**, *9*, 385-387.

(67) Nishiyama, K.; Kubo, A.; Ueda, A.; Taniguchi, I. *Chem. Lett.* **2002**, 80-81.

(68) Disley, D. M.; Cullen, D. C.; You, H. X.; Lowe, C. R. *Biosensor Bioelectron.* **1998**, *13*, 1213-1225.

(69) Jonsson, U.; Fagerstam, L.; Ivarsson, B.; Johnsson, B.; Karlsson, R.; Lundh, K.; Lofas, S.; Persson, B.; Roos, H.; Ronnberg, I.; Sjolander, S.; Stenberg, E.; Stahlberg, R.; Urbaniczky, C.; Ostlin, H.; Malmqvist, M. *Biotechniques* **1991**, *11*, 620-&.

(70) Shang, H. PhD, University of Alberta, 2008.

(71) Kanda, V.; Kariuki, J. K.; Harrison, D. J.; McDermott, M. T. *Anal. Chem.* **2004**, *76*, 7257-7262.

(72) Cao, C.; Sim, S. J. *Biosens. Bioelectron.* **2007**, *22*, 1874-1880.

(73) Jung, Y.; Lee, J. M.; Jung, H.; Chung, B. H. *Anal. Chem.* **2007**, *79*, 6534-6541.

(74) Martin, V. S.; Sullivan, B. A.; Walker, K.; Hawk, H.; Sullivan, B. P.; Noe, L. J. *Appl. Spectros.* **2006**, *60*, 994-1003.

(75) Oh, B. K.; Chun, B. S.; Park, K. W.; Lee, W. C.; Lee, W. H.; Choi, J. W. *Mater. Sci. Eng. C* **2004**, *24*, 65-69.

(76) Lahiri, J.; Ostuni, E.; Whitesides, G. M. *Langmuir* **1999**, *15*, 2055-2060.

(77) Alexander, P.; Fahnestock, S.; Lee, T.; Orban, J.; Bryan, P. *Biochemistry* **1992**, *31*, 3597-3603.

(78) Pribyl, J.; Hepel, M.; Hal·mek, J.; Skl·dal, P. *Sensor Actuator B Chem.* **2003**, *91*, 333-341.

(79) Danson, R. E. a. M. J. *Enzyme Assays: A Practical Approach*; 2nd ed. New York, 1993.

(80) Lutanie, E.; Voegel, J.; Schaff, P.; Freund, M.; Cazenave, J.; Schmitt, A. *Proc. Natl. Acad. Sci.* **1992**, *89*, 9890-9894.

Chapter 4:

Enhanced Surface Plasmon Resonance (SPR) Imaging using Modified Gold Nanoparticles and a Sandwich Immunoassay

4.1 INTRODUCTION

Enhanced or *amplified* SPR assays were terms appearing in the early to late 1990's, not long after the first commercial SPR instrument was brought to market. As SPR assays rely on the ability to detect refractive index changes at a surface, these methods focused on increasing the refractive index shift accompanying surface adsorption. The approaches taken may be divided into two basic categories, those modifying the sensing surface (i.e. the glass underlayer or gold layer) and those modifying the molecule being detected (i.e. with conjugation to particles). Examples of modification to the sensing layer include the addition of a fluoropolymer between the glass and gold layer.[1] The presence of the polymer generates long-range surface plasmons, producing a sharper SPR curve and more sensitive Δ%R measurements. This technique provided an enhancement of only 0.2 over traditional SPR imaging signals. Others have modified the gold film with gold nanoparticles by adsorbing them at varying distances using alkanethiol spacers and SiO_2 layers.[2] The enhancement provided using an SiO_2 layer was found to increase the angle shift by 3.3x that of the control experiment. While these approaches retain the label free nature of an SPR measurement, the enhancement factors observed were significantly less than those achieved from incorporating modified nanoparticles (NPs) as reagents in the assay (e.g., antibody:nanoparticle conjugates), where enhancement factors as high as 1000-fold have been reported.[3-6]

The concept of incorporating modified particles in biological assays was an idea from the 1950's where specific antibodies were conjugated to the surface of latex micro- or nanospheres for use in latex agglutination tests (LAT).[7] Initially, SPR particle enhanced assays incorporated similar latex particles and later expanded to liposomes and certain proteins as mass tags.[6,8] In SPR-based assay, antibody:particle conjugates produce larger refractive index shifts because of the higher mass bound to the surface. Researchers have since moved away from latex and liposome particles and towards metallic nanoparticles. The shift was due to inherent problems of non-specific binding with hydrophobic particles as well as the discovery of unique amplification assays employing more bio-compatible materials such as metallic nanoparticles.

Bio-applications of gold nanoparticles date back to the medieval period where they were used as a medicine for the diagnosis of syphilis.[9] Over the last ten years the development and subsequent applications of these metallic nanoparticles has seen phenomenal growth in chemical catalysis, non-linear optics, and biosciences.[9] The rejuvenated interest dates back to the 1970's where colloidal gold was used as electron dense immunocytochemical probes for electron microscopy.[10] Since then nanoparticles have been incorporated with immunoassay studies using inductively coupled plasma – mass spectrometry (ICP-MS),[11] Raman spectroscopy[12-18] and SPR.[3,4,19-24]

A significant increase in nanoparticle applications has occurred over the last few years and is related to several factors including the improvement of methods to produce and modify these particles.[25] Not surprisingly, this has also resulted in increased availability of pre-functionalized commercially available particles. The gold nanoparticles are also biocompatible, very dense, available in various sizes, and provide the potential for electronic coupling with the planar gold film used in SPR studies.[5,26-28] Another potential advantage of incorporation of modified nanoparticles that has not been widely studied is their impact on the measured affinity constants. As the nanoparticles contain greater numbers of potential binding partners the strength of the interaction, or avidity, of an antibody modified nanoparticle would potentially be significantly greater then an antibody alone. The increased avidity may permit the study of very weakly interacting systems that could not previously be probed with SPR.

This chapter will explore and quantify several aspects of nanoparticle enhanced SPR assays and further extend the detection limits achieved in the previous chapter with the incorporation of a sandwich assay and antibody modified nanoparticles. While nanoparticle enhanced immunoassays have been reported using SPR,[19,20,22,24,29-31] these studies have not examined the impact of modified nanoparticles on the measured binding affinity in detail. Furthermore, the studies mentioned above incorporated scanning angle SPR measurements. SPR imaging has not been used to report on nanoparticle enhanced immunoassays. The focus for SPR imaging appears to have been in DNA-nanoparticle assays.[32-36] This work will incorporate both a scanning angle Biacore

SPR system and a SPR imaging system. The data presented here will evaluate the binding of an unmodified antibody, a 5 nm:antibody conjugate, and a 30nm:antibody conjugate in relation to amplification of the SPR response and the strength of the interaction of these particles with an antigen surface. The detection limits of a 30 nm antibody:nanoparticle conjugate amplified assay will be determined for comparison with the direct assay from the previous chapter. Finally the possibility for electronic coupling will be explored using UV-VIS reflection spectroscopy with values for surface coverage provided using SEM.

4.2 EXPERIMENTAL

Materials and Methods. Chemicals were obtained from the following sources: N-(3-dimethylaminopropyl)-N'-ethylcarbodiimide hydrochloride (EDC), N-hydroxysuccinimide (NHS), 11-mercapto-undecanoic acid, sodium acetate, boric acid, ethanolamine, and bovine serum albumin (BSA), were purchased from Aldrich (St. Louis, MO). Sodium phosphate monobasic monohydrate and certified A.C.S. methanol were purchased from Fisher (Fair Lawn, NJ). Sodium phosphate dibasic heptahydrate, and sodium chloride were purchased from EMD Chemicals Inc. (Darmstadt, Germany). The antibodies used in this work were polyclonal. The anti-rabbit IgG (a-rIgG), rabbit IgG (rIgG), and anti-bovine IgG (a-bIgG) were raised in goat. The bovine IgG (bIgG) was affinity purified from bovine serum. These antibodies were purchased from MP Biomedicals (Solon, OH). 11-Amino-1-undecanethiol, hydrochloride was purchased from Dojindo Laboratories (Japan). N-hydroxysuccinimidyl 12-mercaptododecanoate was purchased from ProChimia Surfaces (Poland). 1-(mercaptoundec-11-yl)tri(ethylene glycol) methyl ether was synthesized by a previous group member[37] using a published method.[38] Tridecafluoro-1,1,2,2-tetrahydrooctyl-1-trichlorosilane (United Chemical Technologies, Inc.). Anhydrous ethyl alcohol was purchased from Commercial Alcohols (Brampton, Ont.). Water used was 18 MΩ deionized water using a Nanopure filtration system. The antibody:nanoparticle conjugates were purchased from Ted Pella, Inc. (Redding, CA). The 5,5'-Dithiobis(succinimidyl-2-nitrobenzoate) (DSNB) was synthesized by a previous group member using a previously published method.[17] Acetonitrile was purchased from Caledon Laboratories Ltd. (Georgetown, Ont.).

SPR Imaging Assays. SF-10 glass substrates (Schott) were diced using a diamond touch dicing saw to 1.8 cm x 1.8 cm. A 1 nm chromium adhesion layer followed by a 45 nm gold layer were thermally evaporated through a shadow mask producing 19 gold spots 1 mm in diameter using a thermal evaporation system (Torr International, inc.). The chips were then immediately placed in a dessicator with a solution of Tridecafluoro-1,1,2,2-tetrahydrooctyl-1-trichlorosilane (United Chemical Technologies, Inc.) and allowed to assemble overnight. The chips were then removed and stored in a dessicator until use.

All imaging assays were performed on a GWC technologies SPR Imager II (Madison, WI). The instrumentation was interfaced and controlled with V++ software. Data analysis involved the averaging of 100 images and correction for non-specific adsorption. Images shown were difference images, which were obtained by subtraction of the initial image in buffer from the image taken following incubation with a protein solution and rinsing with buffer.

Surface Modification. The alkanethiolate surfaces used in the evaluation of nanoparticle modification were prepared by spotting AUT and PEG in 50% EtOH:H2O for 60 minutes. The protein solutions were then patterned by spotting 600 nL of 1.3 μM solutions of rIgG and bIgG that sat for 60 minutes. The binding of a 1.3 nM solution of the commercially available 30 nm antibody:nanoparticle conjugate in 1 mM PBS for 15 minutes was recorded followed by introduction of the lab modified particles. The nanoparticle modification procedure involved taking 1 mL of 30 nm gold nanoparticles ($2x10^{11}$ particles/mL) in water and adding 40 μL each of 50 mM borate buffer (pH 8.5) and 2.5 mM DSNB in acetonitrile. The solution was then mixed and stored for 5 hours at 4^{o}C. Following that incubation 100 μL of 1.3 μM bIgG in 10 mM PBS was added and left for 8 hours. The remaining surface was then blocked for 6 hours with the addition of 10% BSA in 2 mM borate (pH 8.5). The final solution was then centrifuged at 10,000 rpm for 7 minutes at 12^{o}C followed by re-suspension in 500 μL of 1 mM PBS. This method was slightly modified from a previously published report.[39]

The normalized SPR binding curve comparing 5 nm and 30 nm antibody modified particles with unmodified antibody and was collected on a surface modified overnight in a 1 mM 11-Amino-1-undecanethiol, hydrochloride (AUT) in ethanol. The proteins were patterned by spotting 600 nL of solution containing 1.3 μM rIgG, 1.1 μM bIgG, or a 1.5 μM BSA solution in 10 mM PBS (pH 7.4) and incubating for 60 minutes. The binding curves were created by introducing increasing concentration of antibody, 5 nm antibody:nanoparticle conjugate, and 30 nm antibody:nanoparticle conjugate and determining the binding following a 60 minute incubation and buffer wash.

The sandwich assays and limit of detection work involved the surface modification with 1 mM N-hydroxysuccinimidyl 12-mercaptododecanoate in methanol for 60 minutes. The protein solutions were then patterned as above using 6.7 μM a-rIgG and 1.5 μM BSA and let sit for 60 minutes. They were then introduced to the SPR instrument and equilibrated with 10 mM PBS for 30 minutes. The rIgG solutions containing between 200 fM to 200 pM rIgG were prepared from serial dilution of a 6.7 μM rIgG stock solution. These solutions were introduced for 5 minutes to the antibody modified surface followed by a buffer rinse and imaging analysis. For the sandwich assays a solution of either 1333 nM a-rIgG or 1.3 nM 30 nm antibody:nanoparticle conjugate (7.8×10^{11} particles/mL) was then incubated with the surface 5 minutes and again followed with a buffer rinse prior to imaging. The concentration of NPs was calculated using Avogadro's number.

Biacore Binding Assays. A Biacore 3000 system was used with Biacore C1 SPR chips, containing a carboxylic acid terminated monolayer (Biacore Inc., Piscataway, NJ). Each chip is composed on 4 channels. All the channels were activated with 0.4 M EDC and 0.1 M NHS followed by immobilization of either a 10 nM or 100 nM rIgG solution in acetate buffer (pH 4.0) in channels one through three and a 100 nM gIgG solution in the fourth channel. The surfaces were then deactivated with a 1 M ethanolamine solution (pH 8.5) followed by re-equilibration with 10 mM PBS for one hour. Solutions of a-rIgG, 5 nm antibody:nanoparticle conjugate, and 30 nm antibody:nanoparticle were then run sequentially through channels one to three respectively. During each analysis the solutions were also run through channel four as a control. Binding values were corrected for non-specific adsorption using the control channel and plotted as a function of particle concentration, where particle refers to antibody or antibody:nanoparticle conjugate.

Surface Characterization. For UV-VIS reflection and scanning electron microscopy (SEM) analysis thin films of Chromium (10nm) and gold (200nm) were thermally evaporated using a thermal evaporation system (Torr International, inc.) onto Bevel-edge microscope slides measuring 1 x 1.5". Slides were covered and stored in a dessicator then prior to use they were rinsed with 18 MΩ water and anhydrous ethanol and dried under argon gas, placed in a UVO-cleaner (Jelight Company, California) for five minutes, followed by another water and ethanol rinse and drying under argon gas. The surfaces were then immersed in 1 mM MUA for several hours followed by a 30 minute activation with an aqueous solution containing 0.4 M EDC and 0.1 M NHS. The activated surface was then incubated for 60 minutes with a 7.4 μM rIgG solution. The surface was rinsed with buffer and 18 MΩ water prior to being immersed for 30 minutes each with increasing concentrations of 30 nm a-rIgG:nanoparticle conjugates, from 0.013 nM to 1.3 nM (7.8×10^9 to 7.8×10^{11} particles/mL).

The UV-Vis reflection spectra were collected following incubation with each solution with a Perkin Elmer Lambda 35 system with a reflection accessory kit set at an angle of 60^o. A clean gold slide was used as the background. For comparison a UV-VIS absorption solution spectra was taken of the 1.3 nM 30 nm antibody:nanoparticle conjugate using a Hellma (Canada) Limited quartz glass cell with a light path of 10 mm (Concord, Ont.). A solution containing only Tris buffer was used as the blank.

The SEM images were collected on the surface following incubation with the 1.3 nM 30 nm antibody:nanoparticle conjugate following the UV-Vis analysis. The SEM images were collected on a Hitachi S4800 FE-SEM system (Hitachi Scientific Equipment, Japan) equipped with an ultrahigh resolution, low voltage 10 kV SEM inspection with advanced sample navigation package.

4.3 RESULTS AND DISCUSSION

The successful incorporation of nanoparticles (NPs) as reagents in a bio-assay relies heavily on the ability to produce a stable and specific recognition layer around the NPs. The most common modifications are the addition of an antibody recognition layer for use in immunoassays,[3,5,22] and the conjugation of DNA.[21,40,41] However, the addition of other proteins like streptavidin has been reported.[23] Ineffective modification of the NPs will likely provide sources of non-specific adsorption, resulting in reduced assay performance.

Two approaches were taken in the selection of suitable NPs for our SPR studies. The performance of commercially available, antibody modified, 30 nm gold NPs was compared with NPs modified in our labs, using previously published methods.[39] Briefly, these NPs were modified with a DSNB monolayer followed by antibody conjugation. Little information is available on the procedure involved with the modification of the commercial NPs.

To evaluate the different NPs, an SPR chip was patterned with amine and PEG terminated alkanethiolates, followed by spotting of bIgG and rIgG. The array layout is depicted in Figure 4.01(A). The SPR difference images for the binding of the commercially available NPs (a-rIgG recognition layer) and the lab modified NPs (a-bIgG recognition layer) are presented in Figure 4.01(B) and (C) respectively. The Δ%R values from the SPR images are presented in Figure 4.01(D) and show the commercial NPs (a-rIgG recognition layer) exhibit considerable specific binding to the rIgG spots with minimal cross-reactivity to the bIgG or adsorption to the PEG control spots. The lab modified NPs (a-bIgG recognition layer) produced a significantly reduced SPR response for the specific binding of it's antigen (bIgG spots), and produced a greater amount of cross-reactivity with the rabbit antigen. The reduced response for the lab modified NPs is most likely related to a reduced concentration of the modified NPs relative to the commercial NPs used. Although attempts were made to maintain similar particle concentrations, loses of the NPs during the modification process reduced the concentration of these NPs to a point where differences in the color of the commercial and lab modified NP solutions was noted. While steps could be taken to concentrate the lab modified NPs, other drawbacks, including instability in buffers containing standard salt concentrations of 150 mM and increased non-specific binding resulted in their discontinued use. Thus, the commercial antibody coated gold NPs were used for the remaining experiments.

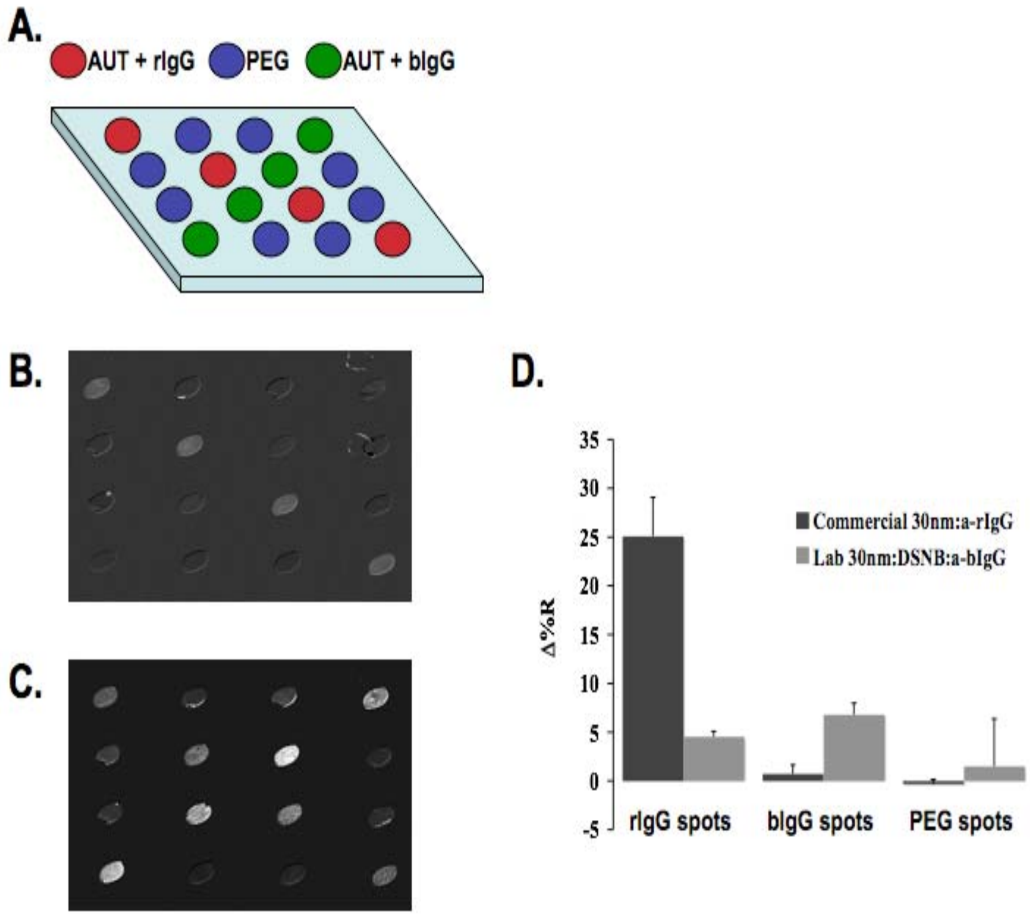

Figure 4.01. The array layout used for the SPR experiments are shown in (A) where the gold spots were modified with either AUT or PEG followed by protein immobilization. The array was then incubated with the commercially modified 30 nm a-rIgG:nanoparticle conjugates (B) and the lab modified 30 nm a-bIgG:DSNB:nanparticle conjugates (C) with the SPR difference images shown. The Δ%R for these difference images is shown in (D).

The next step following selection of the antibody:nanoparticle conjugate was an initial evaluation of the enhancement provided by incorporating these NPs into an immunoassay. The binding of unmodified antibody (a-rIgG) to surface bound antigen (rIgG) was compared to that of a 30 nm antibody:nanoparticle conjugate coated with approximately 86 a-rIgG molecules (determined by vendor). Gold arrays were modified with an amine terminated thiol layer (AUT) and rIgG was spotted on the surface along with BSA and bIgG as negative controls. Figure 4.02 presents the SPR difference images for binding of a 1300 nM a-rIgG solution (A) and a 1.3 nM 30nm:a-rIgG solution (B) with the accompanying Δ%R values (C). The concentration of NPs was calculated by converting the particles/mL value using Avogadro's number. The similar SPR responses reported in Figure 4.02 were obtained with a 1000 fold lower concentration of antibody modified NPs compared with antibody alone. Therefore, as an approximation a 1000x enhancement was ascribed to the incorporation of NPs. Further discussions on the enhancement factors achieved in this work along with literature comparisons are presented later in the chapter following more experimental investigation.

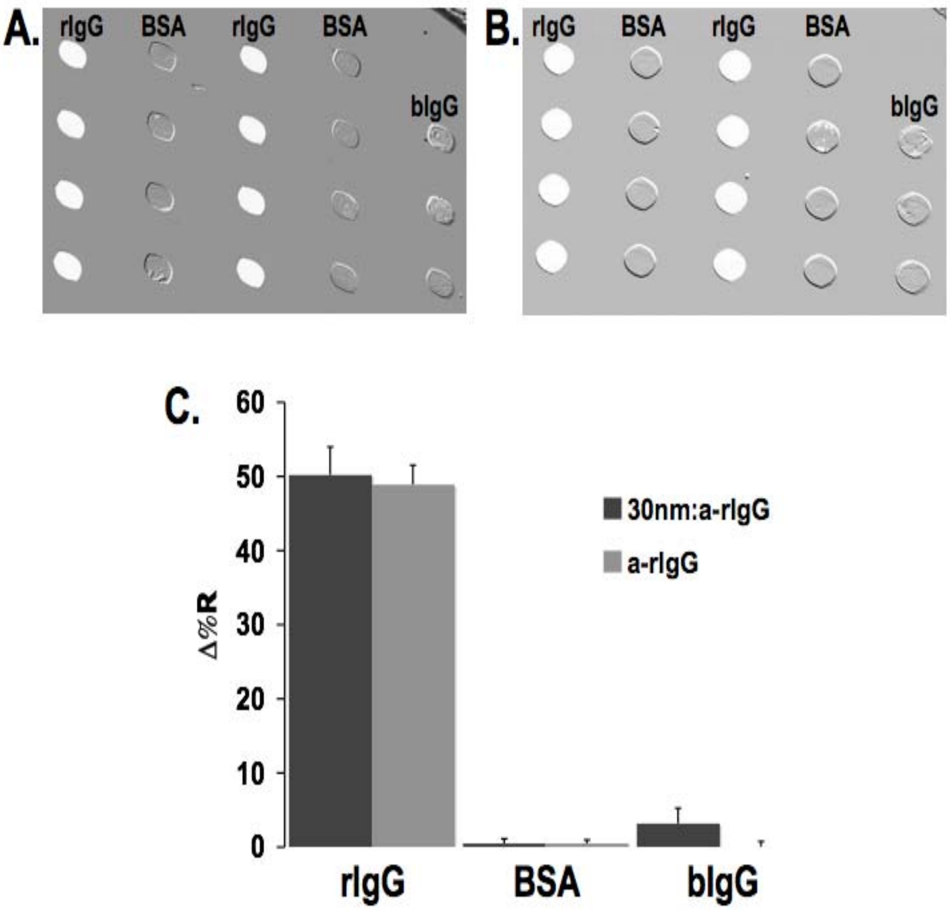

Figure 4.02. The SPR arrays were modified with AUT followed by immobilization of rIgG, BSA, and bIgG. Shown in (A) and (B) are the SPR difference images for the adsorption of a 1300 nM a-rIgG and a 1.3 nM 30 nm a-rIgG:nanoparticle conjugate to the array, respectively. The Δ%R values are also presented in the bar graph (C).

A possible source of enhancement involved in the NP SPR assay shown, is an increase in observed binding affinity for antibody:nanoparticle conjugates relative to unmodified antibody. The increased avidity of the modified NPs would increase the strength of binding between itself and the surface, leading to larger signals at lower concentrations. As each antibody contains two paratopes, the binding of an antibody to an immobilized array of antigen has a maximum valence of two. When examining the binding of a modified nanoparticle to an antigen surface, the nanoparticle has numerous antibodies per particle and therefore the potential for a greater number of interactions with an immobilized antigen layer exists. The impact of binding valence on measured binding affinities is an accepted concept reviewed by Whitesides *et al.*[42] The exploitation of multivalent interactions for enhanced NP sensing has not been examined.

To evaluate the binding affinities of the nanoparticle:antibody conjugates, antibody layers were prepared as above and incubated with increasing amounts of 5 nm and 30 nm modified nanoparticles as well as unmodified antibody. The SPR curves were normalized and are presented in Figure 4.03, where the solid line represents the line of best fit from the least squares analysis using a four parameter logistical equation (1). The fitting parameters are presented in Table 4.1.

$$\Delta\%R = \Delta\%R_{\min} + \frac{\Delta\%R_{\max} - \Delta\%R_{\min}}{1 + \left(\frac{[A]}{K_d}\right)^b} \qquad (1)$$

The parameters in equation 1 are defined in Chapter 2. The measured K_{ADS} (Where $K_{ADS} = 1/K_d$) values, a measure of the binding strength between the surface bound antigen and the antibody or antibody:nanoparticle conjugate, increased upon incorporation of the nanoparticles. The binding of a 5 nm antibody:nanoparticle conjugate showed a marginal increase in binding affinity while the 30 nm conjugate increased the measured affinity constant 280x that of the antibody alone. The 5 nm antibody:nanoparticle conjugate contains approximately 3 antibody molecules per NP and therefore it is unlikely that these NPs would allow for more than a single interaction with an antigen surface. This is consistent with the negligible differences observed in binding constants between the 5 nm NP and the antibody. The 30 nm NPs have 86 antibody molecules per NP, and the larger diameter that leads to greater numbers of antibody's also permits greater numbers of interactions between the antigen surface and the antibody's on the NP surface. It is this increase in the number of interactions that results in the increase in the measured affinity constant.

The large Δ%R values for the binding of antibody and 30 nm antibody modified NPs shown in Figure 4.02, are well out of the linear range of our SPR imaging instrument. It has been shown previously that the SPR response deviates from linearity when Δ%R values become larger than 10 to 15 %.[43] Therefore, to ensure the plateaus observed in the binding curves of Figure 4.03 are the result of surface saturation and not a deviation from linearity, similar experiments were done on an instrument with an expanded linear range. A Biacore 3000 system was used to confirm these results. The Biacore system is a scanning angle instrument that provides a larger linear range, covering a change in refractive index of 0.07 units,[44] compared with 0.04 units[45] for the imaging system. The expanded linear range of the Biacore system will ensure that the saturation values we obtain from NP binding are in fact the result of surface saturation and not an artificial response due to saturation of our instrument. As the value reported for K_{ADS} is essentially the concentration value that produces a detector response midway between the minimum and maximum values (assuming the surface is saturated), it is vital to confirm the upper end of these values to accurately determine the binding constants.

A four channel Biacore C1 chip, modified with a monolayer containing COOH terminal groups, was used for the covalent immobilization of rIgG. The four channels were activated with EDC/NHS followed by the immobilization of a 10 nM rIgG solution in three channels and a 100 nM bIgG solution in the fourth as a control. A solution of ethanolamine was then introduced to all 4 channels, deactivating the unreacted NHS groups. Increasing concentrations of antibody, 5 nm antibody:nanoparticle conjugate, and 30 nm antibody:nanoparticle conjugate were sequentially introduced into channels one through three, respectively. The results were corrected for non-specific adsorption and plotted against particle concentration in Figure 4.04, where particle refers to antibody, 5 nm antibody:nanoparticle conjugate, or 30 nm antibody:nanoparticle conjugate. The solid lines represent the lines of best fit determined by least squares regression analysis using a four-parameter logistical equation. The fitting parameters are presented in Table 4.2.

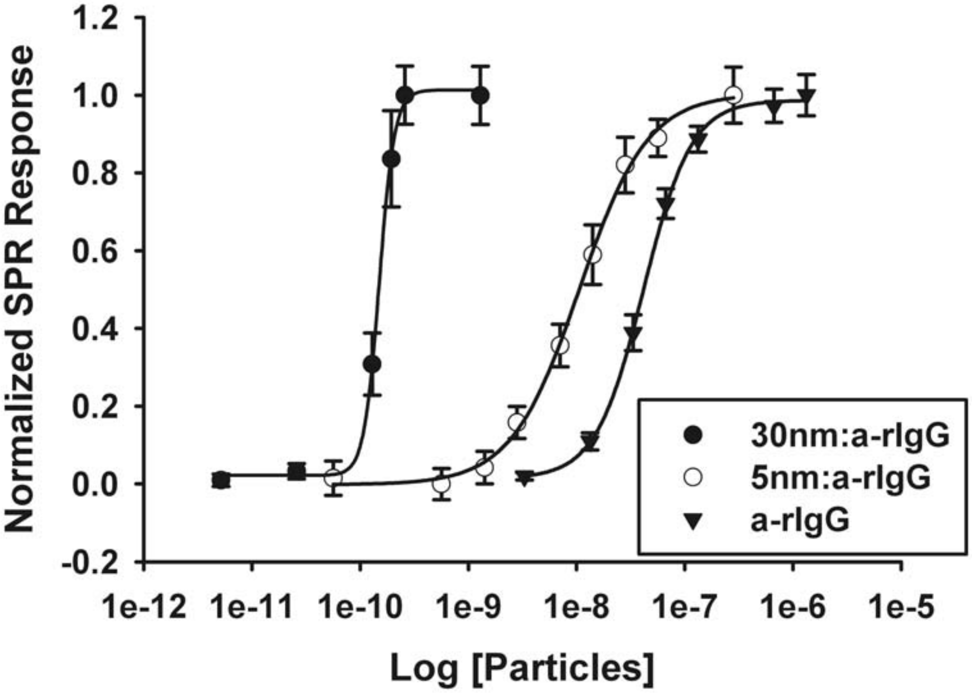

Figure 4.03. Normalized binding curves from SPR imaging experiments for the binding of a-rIgG, 5 nm a-rIgG:nanoparticle conjugate, and 30 nm a-rIgG:nanoparticle conjugate to a rIgG surface. Solid lines represent the lines of best fit from the least squares analysis using a four parameter logistical model. Error bars represent the standard deviation of spots on the SPR array.

Table 4.1. Fitting parameters from the least squares analysis using a four-parameter logistical model. Error values represent uncertainties of the derived fit.

Particle	R^2	K_{ADS} (M^{-1})	Min.	Max.	b
Antibody	0.9989	$2.4 \pm 0.1 \times 10^8$	0.014 ± 0.008	0.987 ± 0.008	-1.97 ± 0.09
5nm:antibody	0.9971	$9.4 \pm 0.6 \times 10^8$	0.00 ± 0.01	1.00 ± 0.02	-1.4 ± 0.1
30nm:antibody	0.9991	$6.7 \pm 0.1 \times 10^{10}$	0.02 ± 0.01	1.01 ± 0.02	-6.2 ± 0.5

The binding curves show that the maximum SPR response increases (RU) as the NP size increases. Also, as the NP size increased the binding curves shift to the left owing to the stronger interaction of the antibody:nanoparticle conjugates. The 30 nm antibody:nanoparticle conjugate increased the observed binding affinity by 600x, compared with 280x increase found using the imaging system. The maximum value was increased 1.8x for the 5 nm conjugate and over 7x for the 30 nm conjugate.

As a final confirmation that the interactions observed in the Biacore experiments were specific and the trends in binding reproducible, the same experiment was performed on chips where the layer of antigen (rIgG) was immobilized at a 10 fold higher concentration (100 nM). The increased antigen concentration should result in larger signals for antibody and antibody:nanoparticle conjugate binding and provide further confirmation that the binding is mediated by the specific antibody-antigen interaction. The binding curves are presented in Figure 4.05 with fitting parameters from the four-parameter logistical model in Table 4.3.

The larger responses show that the interactions were specific with the same trends in binding strength and raw signal observed. The 30 nm antibody:nanoparticle conjugate increased the observed binding affinity by 260x, agreeing very well with a 280x increase found using the SPR imaging system and a high surface density of antigen (as in this case). The maximum SPR response increased 1.2x for the 5 nm conjugate and over 6x for the 30 nm conjugate.

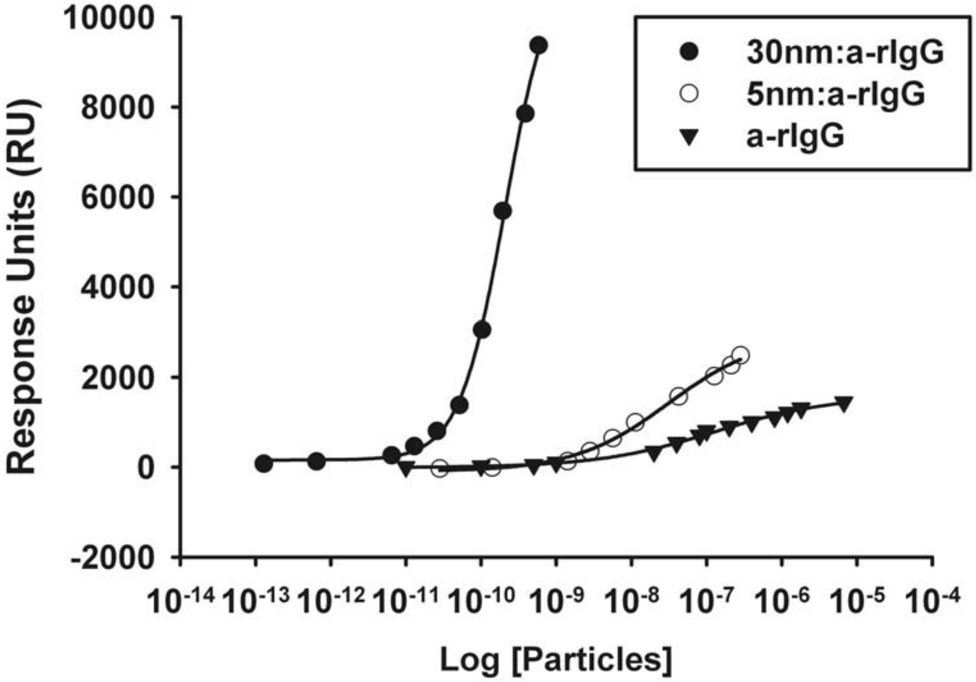

Figure 4.04. Binding curves from Biacore SPR experiments for the binding of a-rIgG, 5 nm a-rIgG:nanoparticle conjugate, and 30 nm a-rIgG:nanoparticle conjugate to a low density rIgG surface. Solid lines represent the lines of best fit from the least squares analysis using a four parameter logistical model.

Table 4.2. Fitting parameters from the least squares analysis using a four-parameter logistical model. Error values represent uncertainties of the derived fit.

Particle	**R^2**	**K_{ADS} (M^{-1})**	**Min.**	**Max.**	**b**
Antibody	0.9955	8 ± 2 x 10^6	-11 ± 20	1587 ± 82	-0.56 ± 0.06
5nm:antibody	0.9957	3 ± 1 x 10^7	-93 ± 43	2938 ± 277	-0.70 ± 0.09
30nm:antibody	0.9984	4.8 ± 0.5 x 10^9	157 ± 74	11393 ± 706	-1.4 ± 0.1

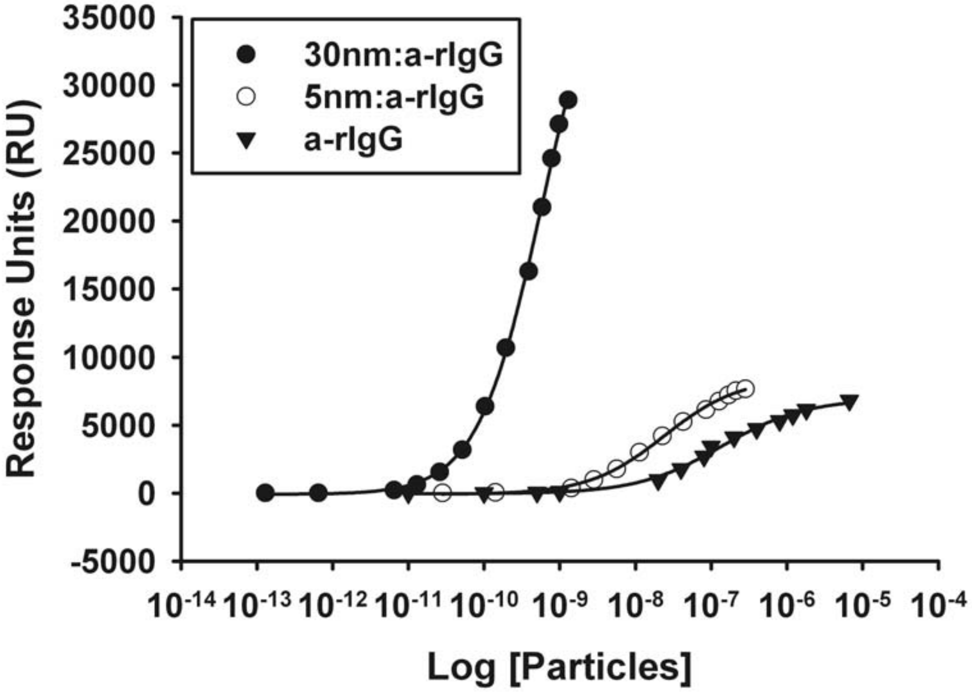

Figure 4.05. Binding curves from Biacore SPR experiments for the binding of a-rIgG, 5 nm a-rIgG:nanoparticle conjugate, and 30 nm a-rIgG:nanoparticle conjugate to a high density rIgG surface. Solid lines represent the lines of best fit from the least squares analysis using a four parameter logistical model.

Table 4.3. Fitting parameters from the least squares analysis using a four-parameter logistical model. Error values represent uncertainties of the derived fit.

Particle	R^2	K_{ADS} (M^{-1})	Min.	Max.	b
Antibody	0.9955	7 ± 1 x 10^6	-59 ± 85	6964 ± 264	-0.78 ± 0.07
5nm:antibody	0.9985	4.2 ± 0.4 x 10^7	-102 ± 71	8526 ± 253	-0.87 ± 0.05
30nm:antibody	0.9992	1.8 ± 0.2 x 10^9	-100 ± 162	42224 ± 2450	-1.02 ± 0.05

The enhancement values reported above fall within the range of those reported in the literature. However, there are several difficulties that should be noted in a direct comparison of enhancement values. There appears to be no universal definition of what the 'enhancement factor' describes. As an example, researchers have used it to describe an enhancement in angle shift where a 28x enhancement was observed for the binding of hIgG:nanoparticle conjugate to an a-hIgG surface.[5] The term has also been related to the increase in raw signal (typically RU in Biacore systems) where 100x increases were reported for the binding of anti-IgG:nanoparticle conjugate binding to an anti-glutamic acid decarboxylase antibody surface.[3] A third use for the term has been describing the enhancements in sensitivity or slopes of concentration plots where values from 100x to over 1000x have been reported.[3,4,22]

In addition to these values reporting on different forms of enhancement, experimental variables such as NP size and wavelength used in the SPR experiments have been shown to impact the enhancement observed.[26] It is clear that care must be taken when describing and comparing the aforementioned enhancement factor of nanoparticle enhanced SPR assays.

Another concern of NP enhanced assays that has not been mentioned previously, but discovered from this work, is the potential inability to achieve saturation coverage for the binding of the antibody modified NPs. Examination of the upper portion of the binding curves presented in Figure 4.04 and 4.05, particularly with the 30 nm antibody:nanoparticle conjugate, do not appear to reach a saturation value. This was investigated using scanning electron microscopy (SEM). A gold surface was modified similar to those used in the Biacore binding experiments. Figure 4.06 shows the SEM images taken from different areas on the antigen coated surface following incubation with a 1.3 nM solution of modified 30 nm NPs. The surface coverage was determined manually using several images taken from different areas on the same surface. The manual counting was performed three times on each sample to ensure accuracy of the value reported. The surface coverage was found to be 48 ± 7 particles/μm^2. The SEM images support the binding curve data, as the surface does not appear to be saturated. The four-parameter logistical fit obtained from the binding curves of the modified 30 nm NPs binding to the low and high density antigen surface indicates that a concentration of approximately 100 nM or $6x10^{13}$ particles/mL would be required to saturate the both of these surfaces. The ability to saturate the nanoparticle solution 100 fold was not attempted and deemed unlikely to be possible without causing aggregation.

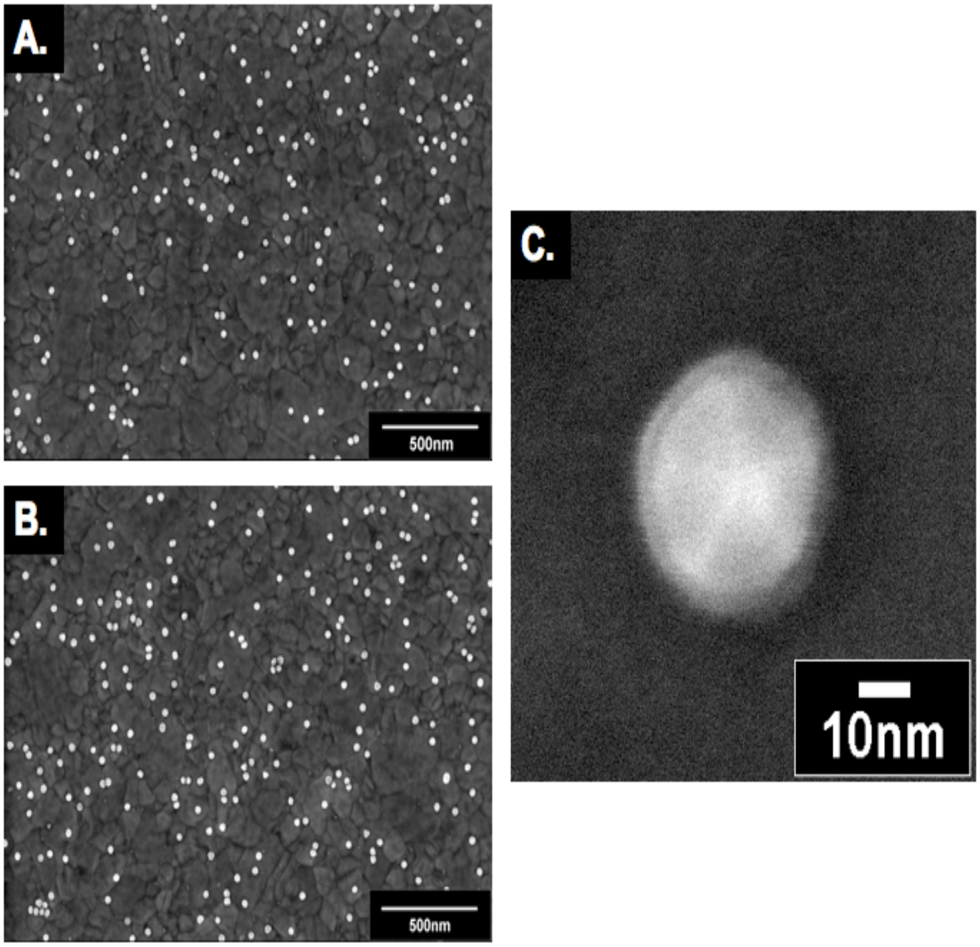

Figure 4.06. Scanning electron microscopy (SEM) images for the adsorption of a 1.3 nM 30 nm a-rIgG:nanoparticle conjugate to a rIgG surface. Images (A) and (B) were taken from random areas on the surface of the slide. Shown in (C) is a high-resolution SEM image of an individual 30 nm nanoparticle with a layer of a-rIgG that was adsorbed to the rIgG surface.

Perhaps a more practical application of the NP assays would be incorporation with a secondary antibody in a sandwich immunoassay. This concept is very similar to the extremely popular enzyme linked immunosorbent assays (ELISA) where the secondary antibody contains an enzyme that is used to detect and quantify specific antigen. The benefits of a sandwich assay include signal enhancement, particularly for the detection of low molecular weight analytes, and added specificity. To determine the enhancement and detection limits possible, pM levels of antigen (rIgG) were incubated with a covalently linked antibody surface and then detected using a normal and NP enhanced sandwich assay.

Surfaces were modified using the optimized covalent attachment of an antibody presented in Chapter 3. These surfaces were incubated with a 200 pM solution of rIgG followed by introduction of a 1300 nM a-rIgG solution or a 1.3 nM 30 nm antibody:nanoparticle conjugate. The SPR difference images shown in Figure 4.07 clearly show differences between binding of unmodified antibody (A) and the 30 nm conjugate (B). The Δ%R values are shown in the bar graph in Figure 4.07(C). The binding of 200 pM rIgG was reproducible on each chip, giving similar SPR responses with values within 3% of each other. The normal sandwich assay improved the detection by 7.5x. The NP conjugate assay improved the detection 100x over the direct assay and 11x over the normal sandwich assay. These values are slightly larger than those previously reported, which determined an enhancement of 1.5x for the sandwich assay and over 28x for the NP enhanced assay compared with the direct detection.[5] The differences in these values and ours may be partially due to the larger nanoparticles in our assay (30 nm vs. 21 nm).

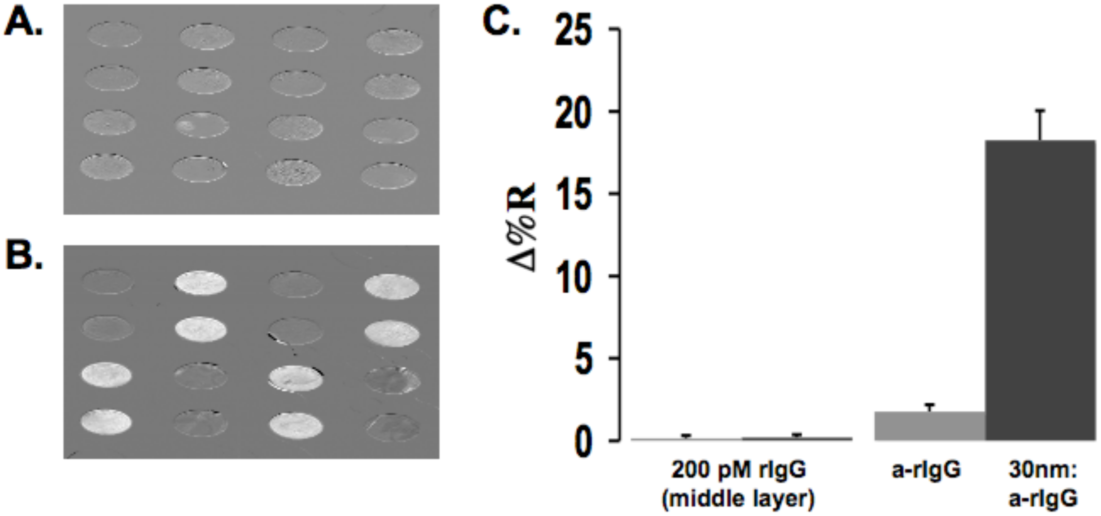

Figure 4.07. The SPR difference images for a sandwich immunoassay containing a 200 pM rIgG middle layer following incubation with 1300 nM a-rIgG (A) or 1.3 nM 30 nm a-rIgG:nanoparticle conjugate. The Δ%R values for the binding of the 200 pM rIgG and the a-rIgG and the a-rIgG conjugate are shown in (C).

The detection limits of this assay were probed with experiments similar to those in Chapter 3. The antibody was covalently linked to the surface, then rIgG solutions from 2 fM to 200 pM were used to probe the detection limits. Separate SPR chips were used for each experiment. The SPR difference images shown in Figure 4.08(A) are those following introduction of a 200 fM rIgG solution (left) and subsequent incubation with a 1.3 nM solution of 30 nm antibody:nanoparticle conjugate (right). The Δ%R values following binding of the 1.3 nM 30 nm modified NPs to the varying concentrations of rIgG (x-axis) are plotted in Figure 4.08(B). The error bars in Figure 4.08(B) represent the standard deviation of the mean signal from the eight spots of the array. The lowest antigen concentration tested (2 fM) was treated as a blank and the Δ%R values obtained were used in equation 2 to determine the limit of detection (LOD). The value obtained from equation 2 was converted to a concentration using the linear fit obtained from least squares analysis, shown in Figure 4.08.

$$LOD = 3\sigma_{blank} + blank \qquad (2)$$

The LOD for rIgG using the 30 nm antibody:nanoparticle conjugate in a sandwich assay was found to be 3.7 ± 0.4 pM. This shows an approximate 20x reduction in detection limit compared with the direct assay presented in the previous chapter (LOD = 77 pM). More recently researchers have noted similar detection limits of 15 pM for the nanoparticle enhanced sandwich assay of an anti-glutamic acid decarboxylase antibody.[3] As in Chapter 3, the detection limits achieved in our lab appear to currently be the lowest reported values.

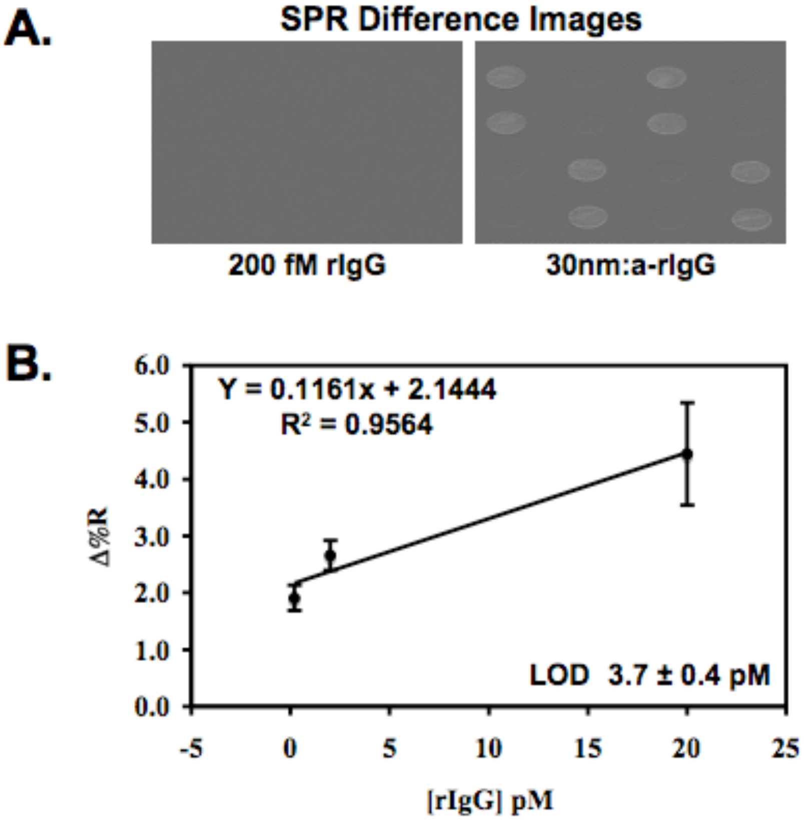

Figure 4.08. The SPR difference images following incubation of an antibody modified surface with a 200 fM rIgG solution (A) and amplification using a 1.3 nM 30 nm a-rIgG:nanoparticle conjugate (B). The plot shown in (C) was constructed by changing the rIgG concentration incubated with an antibody surface and monitoring the Δ%R values following amplification with 1.3 nM 30 nm a-rIgG:nanoparticle conjugate. The error bars represent the standard deviation of the values reported from each spot.

Electronic Coupling. Metallic NPs have the intrinsic ability to generate huge local electric field enhancements as well as strongly enhanced light absorption and scattering upon interaction with light under certain conditions.[46,47] These phenomena are generated following coupling of the optical electric field with the collective oscillation of metal-free electrons of the NP. The frequency at which this occurs depends on the metal, as well as size and shape of NP,[48-50] and inter-particle coupling.[51,52] This phenomenon has been exploited in surface enhanced raman spectroscopy,[12,13,15] metal plasmon enhanced fluorescence,[53] and in NP enhanced SPR assays.[3,5,19,20,22,24,30,31,34] SPR imaging has also been used to confirm the electronic coupling between a gold nanoparticle and a gold substrate.[54] In some cases, nanoparticle enhancement of SPR assays has been attributed to nanoparticle-substrate coupling. The coupling is sensitive to variables such as NP spacing and surface and the frequency of light. We thus performed experiments to test the extent of electronic coupling in our experimental setup.

Surfaces were prepared similar to those used in the initial SPR imaging studies above. A layer of antigen (rIgG) was covalently immobilized to an activated –COOH surface using EDC/NHS chemistry. The surface was then incubated for 30 minutes with increasing concentrations of 30 nm antibody:nanoparticle conjugates, from 0.013 to 1.3 nM. The plasmon resonance band for metal NPs is easily measured in a visible spectrum. Reflection visible spectroscopy has been used to determine the extent of electronic coupling between gold NPs and a gold substrate.[55] Visible reflection spectra were taken following incubation of antigen coated chips with each solution. The solution spectra of the 30 nm antibody:nanoparticle conjugate was also collected to determine if any shift in the absorbance wavelength occurred following surface adsorption.

The visible spectrum of the 30 nm NPs in solution, shown in Figure 4.09(A), exhibits a maximum absorbance at 532 nm. Figure 4.09(B) shows reflection spectra for adsorption of 30 nm antibody modified NPs to an antigen surface. Little absorbance was noted for the 0.013 nM solution, but the values increased with concentration. Also, shown in Figure 4.09(B) is a red-shift of 9 nm, to 541 nm following binding of these NPs to the antigen surface. The red-shift in absorbance of gold NPs has been reported following NP adsorption. When adsorbed to a 2-aminoethanethiol (AET) layer a red-shift of 70 nm was observed. The particles were then separated further from the surface using a 11-amino-1-undecanthiol (AUT) layer and the magnitude of the red-shift decreased by 30 nm. In those examples the surface separation was approximated at 1.2 and 2.3 nm for an AET and AUT layer, respectively. In our example, the separation between the surface and the NPs is occupied by two layers of IgG molecules as well as a SAM on the planar gold surface. Therefore, the distance may be between 10 to 20 nm depending on the orientation of the antibody. The reason we likely see little red-shift upon adsorption is because of the large separation between the surface and particles.

While the small red-shift in absorbance serves as confirmation of the NP surface adsorption, the wavelength at which this absorption or resonance occurs confirms that electronic coupling is not a source of enhancement in our assays. The SPR imaging system used in our studies incorporates only light with a wavelength of 814 nm.

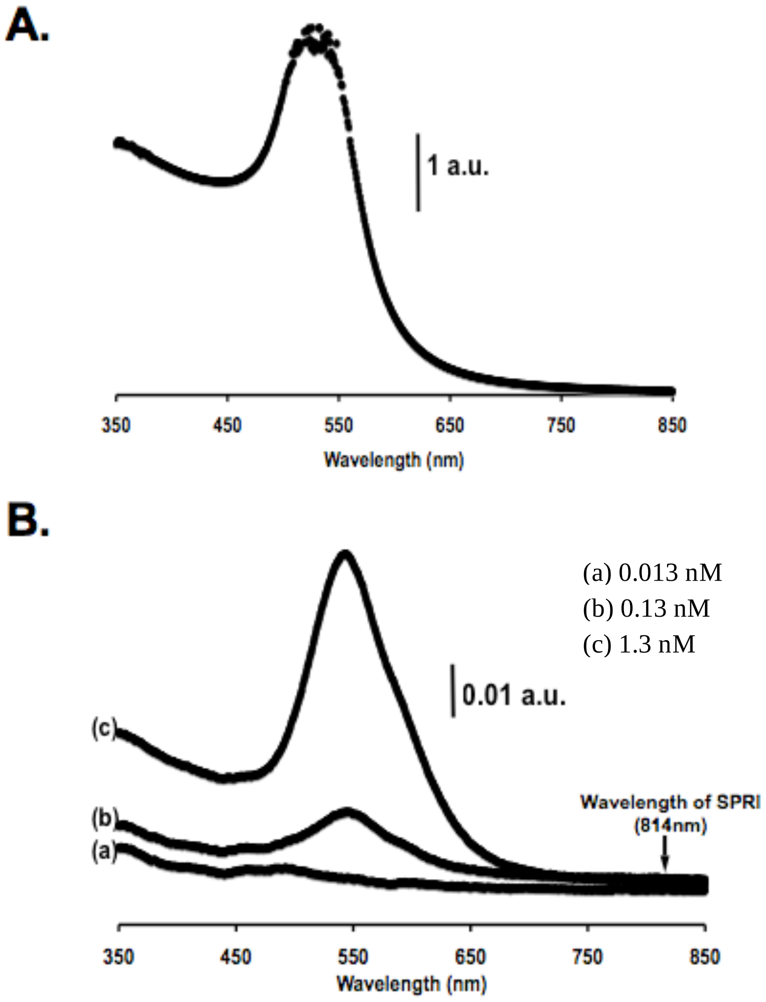

Figure 4.09. The UV-VIS absorption spectra for a 1.3 nM solution of 30 nm a-rIgGa:nanoparticle conjugate (A) and the reflection spectra following the incubation of the antibody conjugates with a rIgG surface (B).

4.4 CONCLUSIONS

This chapter presented a quantitative study on the enhancement provided from the incorporation of gold NPs in SPR immunoassays. Evaluation of several antibody modified NPs was performed to ensure acceptable performance of the antibody modified NPs. The specificity of the antibody:nanoparticle conjugate was confirmed and the binding was shown to be mediated by the antibody coating. The reproducibility of the NP enhancement factors from the SPR results were confirmed by performing several experiments on both an imaging and scanning angle instrument, with the values reported in good agreement. It was also shown that the enhancement observed is related to increased mass upon binding of the NP and not from electronic coupling, as has previously been reported. Finally, a nanoparticle sandwich immunoassay was used to improve upon the detection limits reported in the previous chapter lowering the LOD to 3.7 ± 0.4 pM rIgG.

4.5 REFERENCES

(1) Wark, A. W.; Lee, H. J.; Corn, R. M. *Anal. Chem.* **2005**, *77*, 3904-3907.

(2) He, L.; Smith, E. A.; Natan, M. J.; Keating, C. D. *J. Phys. Chem. B* **2004**, *108*, 10973-10980.

(3) Cao, C.; Sim, S. J. *Biosens. Bioelectron.* **2007**, *22*, 1874-1880.

(4) Pieper-Furst, U.; Kleuser, U.; Stocklein, W. F. M.; Warsinke, A.; Scheller, F. W. *Anal. Biochem.* **2004**, *332*, 160-167.

(5) Lyon, L. A.; Musick, M. D.; Natan, M. J. *Anal. Chem.* **1998**, *70*, 5177-5183.

(6) Kubitschko, S.; Spinke, J.; Brockner, T.; Pohl, S.; Oranth, N. *Anal. Biochem.* **1997**, *253*, 112-122.

(7) Singer, J. M.; Plotz, C. M. *Am. J. Med.* **1956**, *21*, 888-892.

(8) Wink, T.; van Zuilen, S. J.; Bult, A.; van Bennekom, W. P. *Anal. Chem.* **1998**, *70*, 827-832.

(9) Seydack, M. *Biosens. Bioelectron.* **2005**, *20*, 2454-2469.

(10) Hayatt, M. A. E. *Colloidal Gold - Principles, Methods, and Applications*; Academic Press: San Diego, 1989.

(11) Zhang, C.; Zhang, Z.; Yu, B.; Shi, J.; Zhang, X. *Anal. Chem.* **2002**, *74*, 96-99.

(12) Porter, M. D.; Lipert, R. J.; Siperko, L. M.; Wang, G.; Narayanana, R. *Chem. Soc. Rev.* **2008**, *37*, 1001-1011.

(13) Narayanan, R.; Lipert, R. J.; Porter, M. D. *Anal. Chem.* **2008**, *80*, 2265-2271.

(14) Li, T.; Guo, L. P.; Wang, Z. X. *Biosens. Bioelectron.* **2008**, *23*, 1125-1130.

(15) Manimaran, M.; Jana, N. R. *J. Raman Spectros.* **2007**, *38*, 1326-1331.

(16) Kim, J. H.; Kim, J. S.; Choi, H.; Lee, S. M.; Jun, B. H.; Yu, K. N.; Kuk, E.; Kim, Y. K.; Jeong, D. H.; Cho, M. H.; Lee, Y. S. *Anal. Chem.* **2006**, *78*, 6967-6973.

(17) Grubisha, D. S.; Lipert, R. J.; Park, H. Y.; Driskell, J.; Porter, M. D. *Anal. Chem.* **2003**, *75*, 5936-5943.

(18) Ni, J.; Lipert, R. J.; Dawson, G. B.; Porter, M. D. *Anal. Chem.* **1999**, *71*, 4903-4908.

(19) Cho, J. W.; Kang, D. Y.; Jang, Y. H.; Kim, H. H.; Min, J.; Oh, B. K. *Colloid Surface Physicochem. Eng. Aspect* **2008**, *313*, 655-659.

(20) Yuan, J.; Oliver, R.; Li, J.; Lee, J.; Aguilar, M.; Wu, Y. *Biosens. Bioelectron.* **2007**, *23*, 144-148.

(21) Yao, X.; Li, X.; Toledo, F.; Zurita-Lopez, C.; Gutova, M.; Momand, J.; Zhou, F. M. *Anal. Biochem.* **2006**, *354*, 220-228.

(22) Pieper-Furst, U.; Stocklein, W. F. M.; Warsinke, A. *Anal. Chim. Acta* **2005**, *550*, 69-76.

(23) Mitchell, J. S.; Wu, Y.; Cook, C. J.; Main, L. *Anal. Biochem.* **2005**, *343*, 125-135.

(24) Huang, L.; Reekmans, G.; Saerens, D.; Friedt, J. M.; Frederix, F.; Francis, L.; Muyldermans, S.; Campitelli, A.; Van Hoof, C. *Biosens. Bioelectron.* **2005**, *21*, 483-490.

(25) Burda, C.; Chen, X.; Narayanan, R.; El-Sayed, M. A. *Chem. Rev.* **2005**, *105*, 1025-1102.

(26) Lyon, L. A.; Pena, D. J.; Natan, M. J. *J. Phys. Chem. B* **1999**, *103*, 5826-5831.

(27) Lyon, L. A.; Musick, M. D.; Smith, P. C.; Reiss, B. D.; PeÒa, D. J.; Natan, M. J. *Sensor Actuator B Chem.* **1999**, *54*, 118-124.

(28) Leung, P. T.; Pollard-Knight, D.; Malan, G. P.; Finlan, M. F. *Sensor Actuator B Chem.* **1994**, *22*, 175-180.

(29) Zhou, Y.; Xu, H.; Dahlin, A. B.; Vallkil, J.; Borrebaeck, C. A. K.; Wingren, C.; Liedberg, B.; Hook, F. *Biointerphases* **2007**, *2*, 6-15.

(30) Lee, W.; Oh, B. K.; Kim, Y. W.; Choi, J. W. *J. Nanosci. Nanotechnol.* **2006**, *6*, 3521-3525.

(31) Mitchell, J. S.; Wu, Y. Q.; Cook, C. J.; Main, L. *Anal. Biochem.* **2005**, *343*, 125-135.

(32) Corne, C.; Fiche, J. B.; Gasparutto, D.; Cunin, V.; Suraniti, E.; Buhot, A.; Fuchs, J.; Calemczuk, R.; Livache, T.; Favier, A. *Analyst* **2008**, *133*, 1036-1045.

(33) Lockett, M. R.; Weibel, S. C.; Phillips, M. F.; Shortreed, M. R.; Sun, B.; Corn, R. M.; Hamers, R. J.; Cerrina, F.; Smith, L. M. *J. Am. Chem. Soc.* **2008**, *130*, 8611.

(34) Su, X. D.; Teh, H. F.; Aung, K. M. M.; Zong, Y.; Gao, Z. Q. *Biosens. Bioelectron.* **2008**, *23*, 1715-1720.

(35) Manera, M. G.; Spadavecchia, J.; Leone, A.; Quaranta, F.; Rella, R.; Dell'atti, D.; Minunni, M.; Mascini, M.; Siciliano, P. *Sensor Actuator B Chem.* **2008**, *130*, 82-87.

(36) Fang, S. P.; Lee, H. J.; Wark, A. W.; Corn, R. M. *J. Am. Chem. Soc.* **2006**, *128*, 14044-14046.

(37) Kanda, V. K. PhD, University of Alberta, 2004.

(38) Pale-Grosdemange, C.; Simon, E. S.; Prime, K. L.; Whitesides, G. M. *J. Am. Chem. Soc.* **1991**, *113*, 12-20.

(39) Driskell, J. D.; Kwarta, K. M.; Lipert, R. J.; Porter, M. D.; Neill, J. D.; Ridpath, J. F. *Anal. Chem.* **2005**, *77*, 6147-6154.

(40) Lee, H. J.; Wark, A. W.; Corn, R. M. *Analyst* **2008**, *133*, 596-601.

(41) He, L.; Musick, M. D.; Nicewarner, S. R.; Salinas, F. G.; Benkovic, S. J.; Natan, M. J.; Keating, C. D. *J. Am. Chem. Soc.* **2000**, *122*, 9071-9077.

(42) Mammen, M.; Choi, S. K.; Whitesides, G. M. *Angew. Chem., Int. Ed.* **1998**, *37*, 2755-2794.

(43) Smith, E. A.; Corn, R. M. *Appl. Spectros.* **2003**, *57*, 320A-332A.

(44) BIACORE 2003.

(45) Nelson, B. P.; Grimsrud, T. E.; Liles, M. R.; Goodman, R. M.; Corn, R. M. *Anal. Chem.* **2001**, *73*, 1-7.

(46) Kelly, K. L.; Coronado, E.; Zhao, L. L.; Schatz, G. C. *J. Phys. Chem. B* **2003**, *107*, 668-677.

(47) Kreibig, U.; Vollmer, M. *Optical properties of metal clusters*; Springer: New York, 1995; Vol. 25.

(48) Jain, P. K.; Lee, K. S.; El-Sayed, I. H.; El-Sayed, M. A. *J. Phys. Chem. B* **2006**, *110*, 7238-7248.

(49) El-Sayed, M. A. *Acc. Chem. Res.* **2001**, *34*, 257-264.

(50) Link, S.; El-Sayed, M. A. *Int. Rev. Phys. Chem.* **2000**, *19*, 409-453.

(51) Jain, P. K.; Qian, W.; El-Sayed, M. A. *J. Phys. Chem. B* **2006**, *110*, 136-142.

(52) Su, K. H.; Wei, Q. H.; Zhang, X.; Mock, J. J.; Smith, D. R.; Schultz, S. *Nano Lett.* **2003**, *3*, 1087-1090.

(53) Aslan, K.; Lakowicz, J. R.; Geddes, C. D. *Curr. Opin. Chem. Biol.* **2005**, *9*, 538-544.

(54) Hutter, E.; Cha, S.; Liu, J. F.; Park, J.; Yi, J.; Fendler, J. H.; Roy, D. *J. Phys. Chem. B* **2001**, *105*, 8-12.

(55) Driskell, J. D.; Lipert, R. J.; Porter, M. D. *J. Phys. Chem. B* **2006**, *110*, 17444-17451.

Chapter 5:

Mono- and Multilayered Aryl Films for Surface Plasmon Resonance (SPR) Imaging Studies

5.1 INTRODUCTION

A critical step in bioassay development is the surface modification of a solid support permitting the controlled immobilization of biomolecules. The self-assembly of alkanethiolates on gold, first published by Nuzzo and Allara in 1983,[1] has been a prominent method for surface modification. The ease of the experimental procedure, the range of surface functionalities available, and the high level of understanding of the nature of the interface formed have resulted in its widespread use of this monolayer-substrate combination.[2-11] The ability of the self-assembled monolayers (SAMs) to produce an ordered functionality at the interface is due primarily to the ability of these SAMs to self-anneal. The weaker nature of the gold-thiolate bond that permits self-annealing also results in making the bond susceptible to oxidation,[12] thermal instability,[13] and presents a limited electrochemical window in which the layer is stable.[14,15] Therefore, it may be advantageous to pursue a more robust and covalent surface modification strategy.

Interest in the modification of surfaces by the electrochemical reduction of diazonium salts has grown steadily since its first published report by Pinson in 1992.[16] His discovery marked the first report on the ability to covalently modify carbon surfaces through a reductive strategy, producing a solid and non-corrosive surface with the covalent attachment of aryl groups. This surface modification strategy has since been expanded to many other conductive and semi-conductive surfaces, including gold.[17-20] The stability of surfaces modified with these aryl films has been shown to withstand ultrasonication,[17,18] potential cycling in aqueous sulfuric acid,[20,21] and storage for several months under ambient laboratory conditions.[16] Because of the similarities in aryl film structure and stability on both carbon and gold surfaces it is believed that similar mechanisms are involved in the electrochemical surface attachment of diazonium salts.

The proposed mechanism for the reductive adsorption of diazonium salts is believed to proceed by a one-electron reduction of the diazonium cation, producing an aryl radical that is then chemically grafted to the electrode surface.[16,19] The mechanism is presented in Figure 5.01. These films have been shown to exhibit improved stability over alkanethiolate SAMs.[21] In addition to the increased stability of these layers, researchers have shown that under appropriate conditions aryl film growth resulted in multilayered aryl films.[22-24] Therefore, another potential advantage to this surface modification strategy may be an increased sensing surface area which may improve sensitivity over surfaces modified with monolayers of alkanethiolates.

Applications for surfaces modified with aryl films range from molecular electronics[25-27] to biosensors.[28-36] The wide range of para-substituted diazonium salts available has aided greatly in our ability to tailor interfacial surface chemistry and its widespread use. One of the first biosensor applications reported the covalent attachment of glucose oxidase to a carbodiimide activated 4-phenylacetic acid layer.[37] Since then other common biomolecule immobilization chemistries have been shown including the generation of maleimide,[30] amine,[28] and nitriliotriacetic (NTA)[36] surfaces capable of covalent attachment, affinity capture, and physical adsorption. These surfaces have been used to facilitate the attachment of DNA,[31,32] proteins,[29,37,38] and peptides.[21]

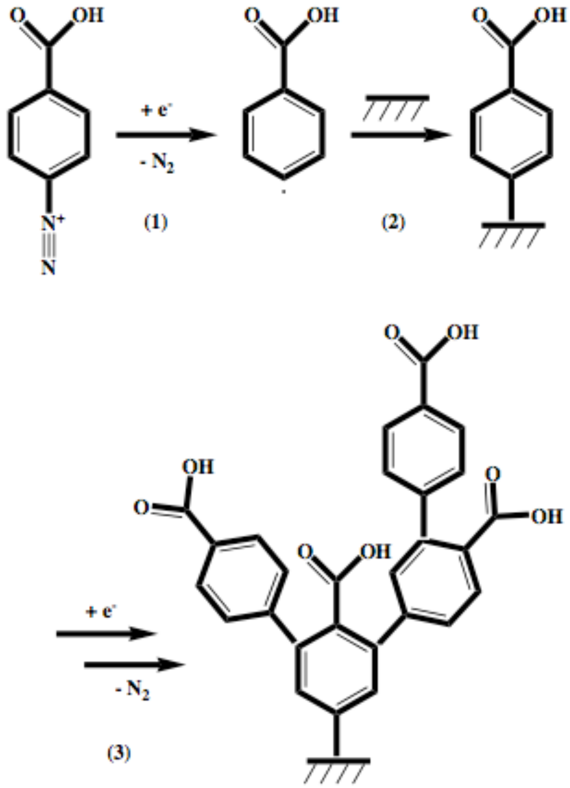

Figure 5.01. Mechanism for the surface attachment and multilayer formation of an aryl diazonium. The process involves (1) electrochemical generation of an aryl radical followed by (2) surface attachment (3) and multilayer growth.

Detection of binding events have primarily involved electrochemical methods.[29-31,35-38] However, other techniques including chemiluminescence,[32] and fluorescence detection have also been used.[34] A potential drawback of these techniques is the requirement to incorporate an electroactive, luminescent, or fluorescent probe to permit the detection of binding events. The application of these surface modification strategies for use with a label-free detection technique such as surface plasmon resonance (SPR) would alleviate labeling steps and provide the potential for efficient, parallel, and sensitive measurement of binding affinities.

The work presented in this chapter reveals the first report of a SPR imaging study using a diazonium functionalized surface for immunoassay applications. In this work a benzoic acid diazonium salt was electrochemically grafted to a gold surface using cyclic voltammetry. The ability to control surface coverage and multilayer growth was characterized using infrared reflection absorption spectroscopy (IRRAS) and atomic force microscopy (AFM). The application of these surfaces as an immunoassay support was achieved through covalent immobilization of antibodies to the activated benzoic acid surfaces. Once the antibodies were attached, antigen binding was monitored using SPR imaging. The impact of surface coverage and expansion to a multilayered surface on immunoassay performance was examined.

5.2 EXPERIMENTAL

Materials and Methods. Chemicals were obtained from the following sources: 4-mercaptobenzoic acid (4-MBA), N-(3-dimethylaminopropyl)-N'-ethylcarbodiimide hydrochloride (EDC), N-hydroxysuccinimide (NHS), ethanolamine, 4-aminobenzoic acid, tetrafluoroboric acid (48% wt in H_2O), sodium nitrite, and tetrabutylammonium tetrafluoroborate (Bu_4NBF_4) were purchased from Aldrich (St. Louis, MO). Sulfuric acid and acetonitrile were purchased from Caledon Laboratories Ltd. (Georgetown, Ont.). Hydrogen peroxide, sodium phosphate monobasic monohydrate, and polyoxyethylene 20-sorbitan monolaurate (Tween 20) were purchased from Fisher (Fair Lawn, NJ). Silver nitrate, sodium phosphate dibasic heptahydrate, hexane, and sodium chloride were purchased from EMD Chemicals Inc. (Darmstadt, Germany). Anti-rabbit IgG and rabbit IgG were purchased from MP Biomedicals (Solon, OH). Anhydrous ethyl alcohol was purchased from Commercial Alcohols (Brampton, Ont.). Water used was 18 MΩ deionized water using a Nanopure filtration system. Polydimethylsiloxane (PDMS) was made using a Sylgard 184 Silicone Elastomer Kit from Dow Corning (Midland, MI).

Diazonium Synthesis and Surface Modification. A fellow group member, using a modified version of a method first published by Starkey,[39] synthesized the benzoic acid diazonium salt. Briefly, the precursor molecule (4-aminobenzoic acid) was partially dissolved in 50% fluoroboric acid at 0°C to form a 225 mM supersaturated solution. A saturated aqueous solution of sodium nitrite at 0°C was then added dropwise in a 3:1 ratio to the 4-aminobenzoic acid, dissolving this acid. The solution was shielded from light and left to react for thirty minutes. Following this, the product was filtered and washed with anhydrous ether. The powdery white solid was then recrystallized in anhydrous acetonitrile at 0°C, filtered, and rotovaped on ice until dry. The product was stored in a dessicator at 4°C and covered from light.

Prior to surface modification the gold substrates were cleaned with a piranha solution made with 1:3 H_2O_2:H_2SO_4. Following thorough rinsing with deionized water and drying under $Ar_{(g)}$ the gold surface was placed in a 0.5 mM diazonium benzoic acid (dzBA) solution containing 0.1 M Bu_4NBF_4 in acetonitrile. The diazonium salt was electrochemically deposited by cycling the potential from 100 to -1000 mV versus a Ag/$AgNO_3$ reference electrode using a Pine bipotentiostat controlled with Pine software version 2.7.9. A platinum mesh counter electrode was also used.

Infrared Reflection Absorption Spectroscopy (IRRAS) Measurements. Bev-l-edge micro slides (Proper Manufacturing Co., Inc., Germany) were cleaned in piranha solution prior to metal deposition. Thin films of chromium (10 nm) and gold (300 nm) were thermally evaporated using a thermal evaporation system (Torr International, Inc.). IRRAS spectra were collected using a Matson Infinity FT-IR instrument equipped with a low-noise mercury-cadmium-tellurium detector cooled with liquid N_2 to 77 K. Spectra were collected from 1000 scans at a resolution of 2 cm^{-1} and a glancing angle of approximately 80^o. A freshly cleaned gold coated slide was collected for the background spectrum. Data analysis including peak height and width was determined with manual baseline correction using winfirst software.

Surface Plasmon Resonance (SPR) Imaging. Substrates used were 1.8 cm x 1.8 cm squares of SF-10 glass (Schott, ON, Canada) modified with a 1 nm chromium adhesion layer and 45 nm of gold. Following electrochemical surface modification the benzoic acid surfaces were activated with a solution of 0.4 M

EDC and 0.1 M NHS for 30 minutes. A PDMS microfluidic device was used to pattern lines of 3.3 μM polyclonal a-rIgG (goat host) solution that was incubated for 15 minutes. Channels were rinsed with buffer and the PDMS removed. The substrates were then placed into a GWC SPR Imager II and a 1 M ethanolamine solution (pH 8.5) was introduced and incubated for 30 minutes. This was followed by a 30 minute rinse with 10 mM PBST (containing 0.05% tween 20). Polyclonal rabbit IgG (goat host) solutions were prepared by dilution of a stock solution with each solution introduced continuously to the array surface for 5 minutes followed by rinsing with PBST between antigen solutions. Data analysis involved the averaging of 100 images and correction for non-specific adsorption. Images shown were difference images, which were obtained by subtraction of the initial image in buffer from the image taken following incubation in rIgG and rinsing with PBST.

Atomic Force Microscopy (AFM). A silicon wafer was coated with 1 nm thermally evaporated chromium adhesive layer followed by 45 nm of gold. Modification of gold substrates with aryl films were conducted electrochemically, as described earlier. A Multimode scanning probe microscope (SPM) equipped with a Nanoscope IIIa controller was used for ‘scratching’ and to collect topographic images of surfaces using a silicon probe cantilever (Micro Cantilever, OLYMPUS) having a spring constant of 1 N/m. The same cantilever was used throughout the entire experimental process.

‘Scratching’ of the aryl film occurred by initially imaging a 2 μm x 2 μm square in contact mode while applying a normal force of 600 nN, at a rate of 5.0

Hz. The tip was allowed to scan the area 4 consecutive times to ensure the entire aryl film was removed. The normal force was then decreased to lift the tip off the surface and 5 μm x 5 μm topographic images were collected in tapping mode at a rate of 1.0 Hz and a drive frequency in air of 62.0 kHz. The thickness of the layer was determined by comparing the z-axis peizo range inside the scratched area with that of the outside. To avoid biasing the data the average z-axis piezo range for a sample area of 0.24 μm^2 was used. This procedure was repeated three times for analysis of each of the surfaces tested.

5.3 RESULTS AND DISCUSSION

Diazonium Deposition with Cyclic Voltammetry. Gold electrodes were modified with benzoic acid from the corresponding diazonium salt using a three-electrode system. Cyclic voltammetry was used to control the electrochemical reduction and surface attachment of the diazonium salt onto the gold surface. Shown in Figure 5.02 and 5.03 are the cyclic voltammograms (CVs) from a 0.5 mM benzoic acid diazonium salt with the potential cycled at 10 mVs^{-1} and 100 mVs^{-1} from 100 to -1000 mV versus a Ag/Ag^+ electrode.

When the potential was scanned at 10 mVs^{-1} a large irreversible wave was observed at $E_{p,c}$ = -200 mV, with a small pre-wave at $E_{p,c}$ = -20 mV, vs Ag/Ag^+. When the potential was scanned at 100 mVs^{-1} a large irreversible waves were observed, $E_{p,c}$ = -270 mV, with a small pre-wave at $E_{p,c}$ = -70 mV, vs Ag/Ag^+. The large irreversible wave in Figure 5.02 and 5.03 is due to the one electron reduction of the diazonium salt. The pre-wave observed in these figures is characteristic of strong adsorption of electroactive species.[40] Recently, similar pre-waves have been observed and attributed to the adsorption of the diazonium to the electrode surface.[30] Additional potential cycles do not show reductive waves, consistent with successful electrode passivation. It should be noted however, that the significant reduction in overall current following surface passivation does not indicate inhibition of further layer growth. It has been shown, and will be confirmed here, that successive potential scanning results in continued layer growth, even in the absence of a reductive wave.[18] The mechanism by which additional cycles produce increased layer growth and no observable current will not be subject of this study and will require further work. However, one possibility is that the amount of current passed during these additional cycles is below the detection limit of cyclic voltammetry.

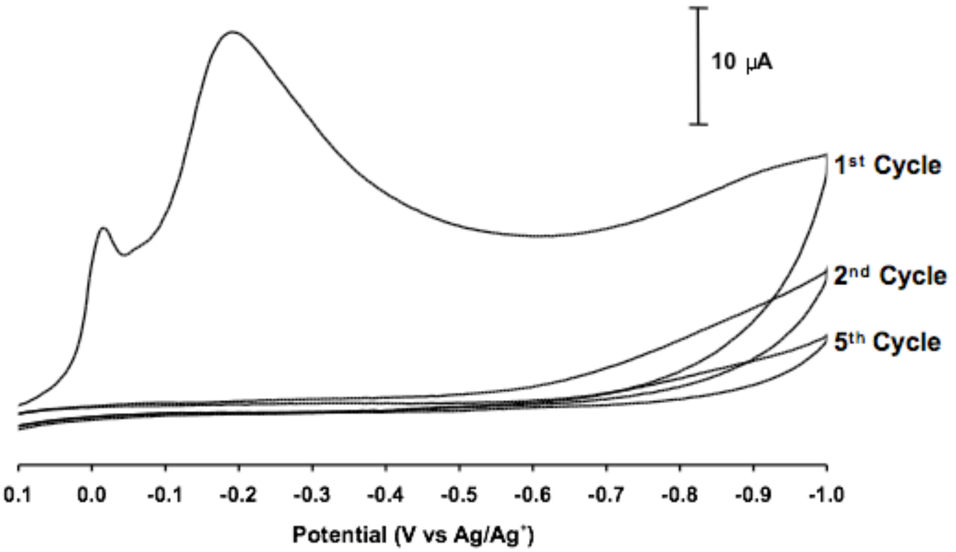

Figure 5.02. Cyclic voltammograms of a gold electrode in 0.1 M $TBABF_4$ + 0.5 mM dzBA/acetonitrile; Scan rate = 10 mVs^{-1}.

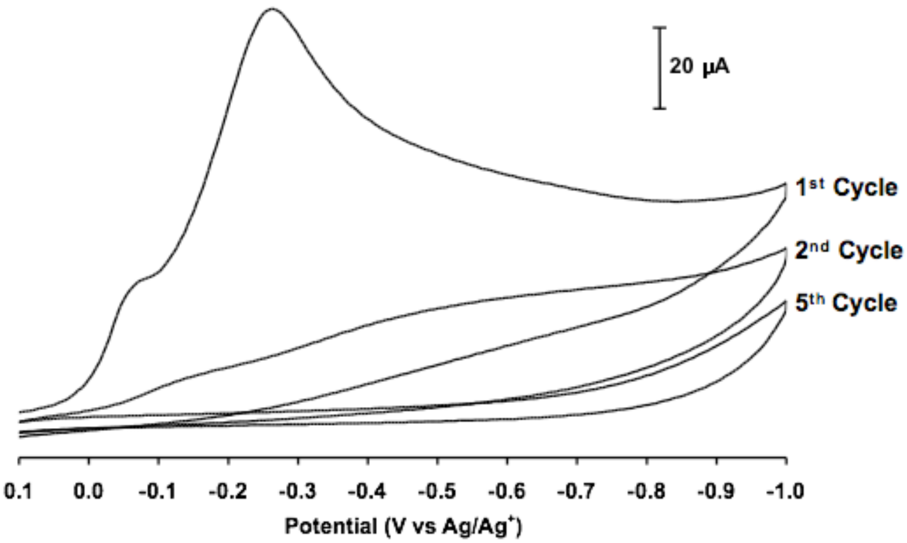

Figure 5.03. Cyclic voltammograms of a gold electrode in 0.1 M TBABF$_4$ + 0.5 mM dzBA/acetonitrile; Scan rate = 100 mVs^{-1}.

Infrared Reflection Absorption Spectroscopy (IRRAS). IRRAS was used to confirm the surface attachment of the dzBA and probe the growth of the adsorbed layer(s). Surface characterization of 4-mercaptobenzoic acid (4-MBA), the thiol analogue to dzBA, was also performed. Inclusion of the thiol analogue provided a familiar benchmark that was used to compare and draw conclusions on the type of layer(s) formed by the electrochemical reduction of dzBA. Comparison of similar IR vibrations in terms of peak position, intensity, and width provided insight into how the layers were arranged and the interface the protein encountered when introduced for immobilization. IRRAS was also used to characterize the impact of potential scan rate on the layer(s) formed.

Figure 5.04 presents the IRRAS spectra for surfaces modified with either 4-MBA or dzBA. The IRRAS spectra confirm the successful surface modification by the dzBA with vibrations observed from the carboxylic acid and the aromatic ring. Comparison with the 4-MBA spectra reveals agreement between the vibrations observed, with several differences noted in the peak position and width of the carbonyl stretch ($\nu_{c=o}$). Table 5.1 presents the band assignments.

Table 5.1. IRRAS band assignments for dzBA and 4-MBA films

Wavenumber (cm^{-1})	Band Assignment
3590	-O-H from carboxylic acid
1754 – 1710	-C=O from carboxylic acid
1612 - 1590	-C=C or –C-H from aromatic ring
1422 – 1365	-C=C or –C-H from aromatic ring
1190	unassigned
1176	unassigned

The difference in the $\nu_{c=o}$ band between the dzBA and the 4-MBA layers is believed to arise based on differences in the extent of hydrogen bonding in these films. The frequency of the observed IR vibration of a bond is related to its stretching force constant. An increase in hydrogen bonding results in a weakening of the C=O bond, lowering the stretching force constant.[41] Therefore, an increase in hydrogen bonding in the dzBA layers relative to the 4-MBA layer may be the cause of the shift in $\nu_{c=o}$ band position. Also, in relation to the dzBA films, the increase in frequency of this band with number of scans is likely related to changes in hydrogen bonding as the dzBA films grow. Figure 5.05 presents further IRRAS data supporting an increase in hydrogen bonding on the dzBA film

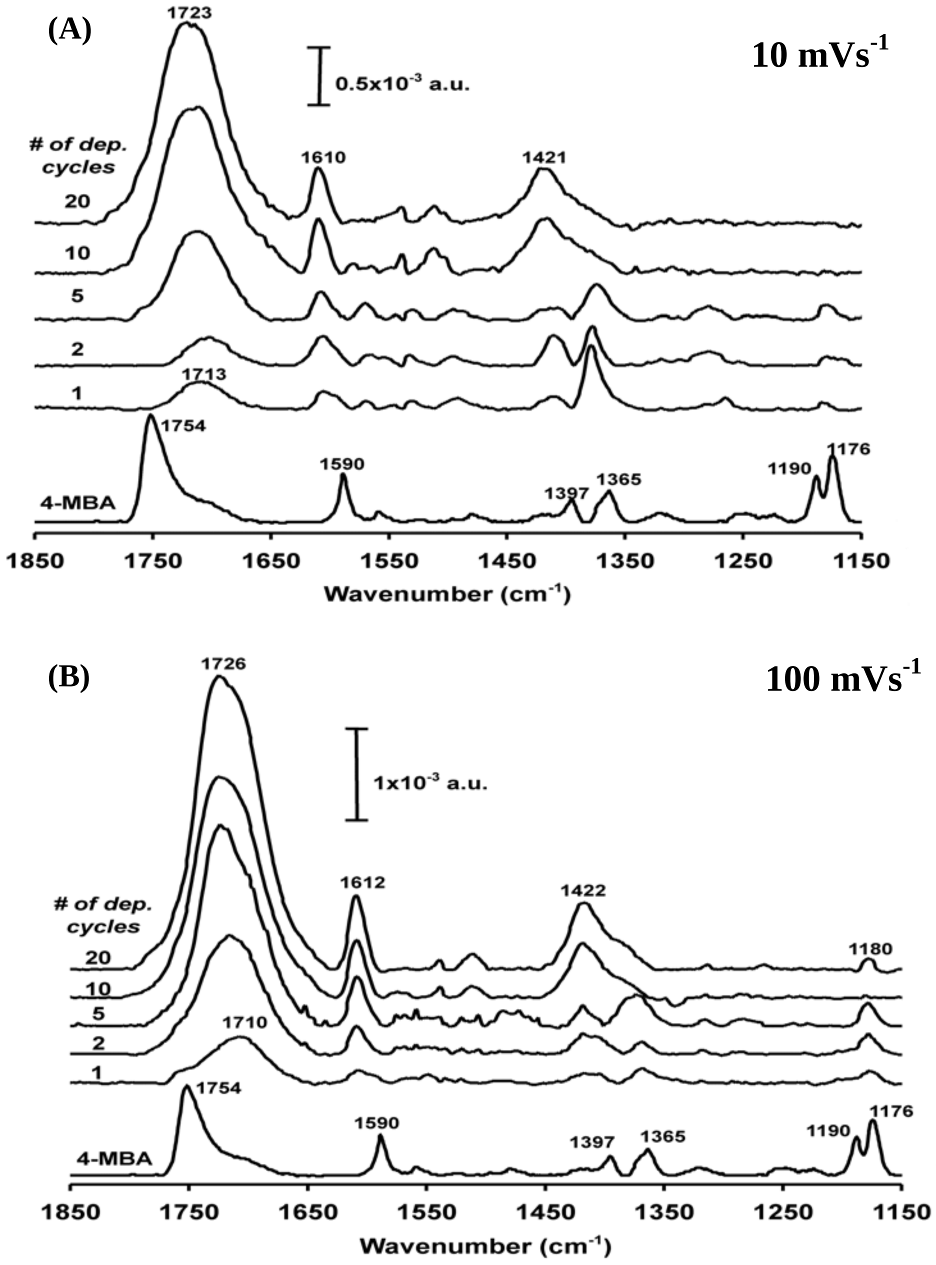

Figure 5.04. FT-IRRAS spectra for gold surfaces modified with a SAM of 4-mercaptobenzoic acid (4-MBA) or the electrochemical deposition of a 0.5 mM dzBA at 10 mVs^{-1} (A) and 100 mVs-1 (B). Surfaces were modified with 1 to 20 deposition cycles prior to analysis.

with the absence of the O-H band at 3590 cm^{-1}. The band is only observed in dilute solutions/surfaces where hydrogen bonding is unlikely.[41] Therefore, the shifting in band position and increased width of the $\nu_{c=o}$ band suggest the diazonium layers are present on the surface in a non-uniform environment with varying degrees of hydrogen bonding.

IRRAS has previously been used to track the multilayer growth of a diazonium salt.[22] For this work, IRRAS was also used to examine the growth of the dzBA layers and the impact of the potential scan rate used for the deposition. Figure 5.04 shows an increase in IR band intensity with the number of deposition cycles. In an effort to correlate layer growth with the number of deposition cycles, a plot of $\nu_{c=o}$ peak height against the number of electrochemical deposition cycles was constructed and is shown in Figure 5.06. The $\nu_{c=o}$ band was chosen as it was the most prominent band in the spectrum and the most sensitive to the deposition conditions. The films formed at both 10 mVs^{-1} and 100 mVs^{-1} show similar trends, with an initial sharp increase followed by a more gradual and continuous growth. A similar trend has previously been observed when monitoring the growth of diazonium layers on gold using an electrochemical quartz crystal microbalance (EQCM). The researchers observed a sharp increase in deposited mass on the initial scan followed by a more gradual increase with successive scanning. They concluded that the sharp increase was a result of the initial surface coverage followed by a much slower region that was attributed to multilayer growth.[18]

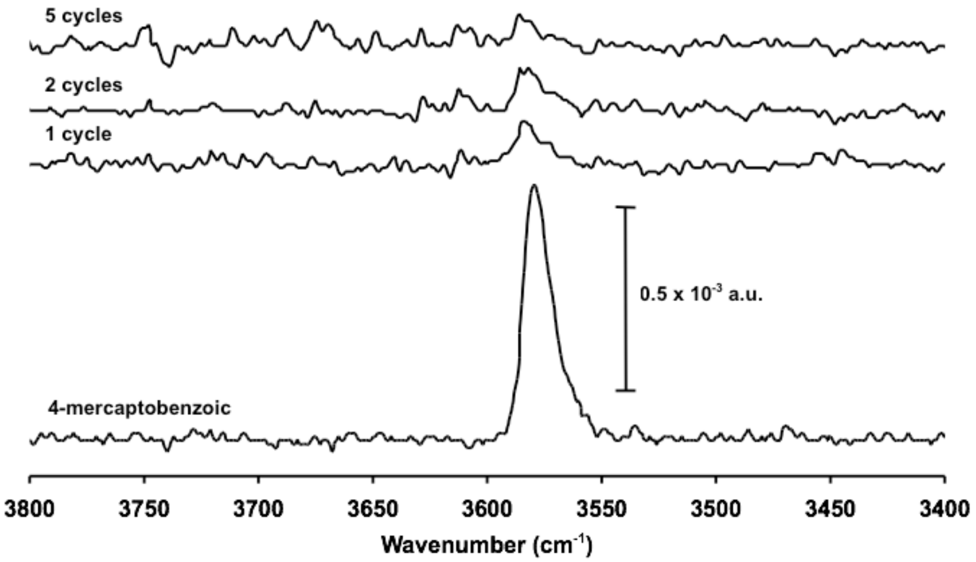

Figure 5.05. FT-IRRAS spectra for gold surfaces modified with a SAM of 4-mercaptobenzoic acid (4-MBA) or the electrochemical deposition of a 0.5 mM benzoic acid diazonium salt. The peak at 3590 cm^{-1}, from the –OH group, is characteristic of a dilute surface with limited hydrogen bonding between neighboring –OH groups. The absence of this peak in the electrochemically deposited layers suggests that the -OH groups are in closer proximity and hydrogen bonding is present.

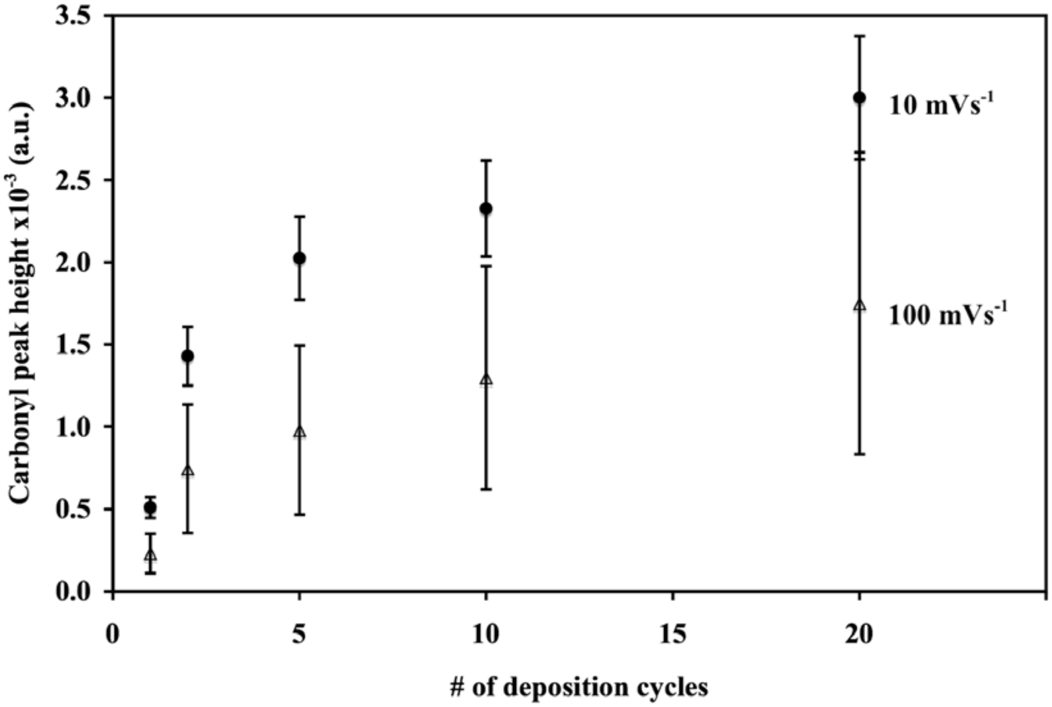

Figure 5.06. Plot of the IRRAS carbonyl peak height for gold surfaces electrochemically modified with a 0.5 mM diazonium benzoic acid solution. Error bars represent the relative standard deviation (n=3).

The IRRAS data was also used to approximate the amount of surface bound aryl groups by comparison with the thiol analogue, 4-MBA. Due to the large differences in peak widths between the $\nu_{c=o}$ bands of 4-MBA and dzBA the area, peak area was used to compare the density of the carboxylic acid groups on the surface. As there are no significant changes in the peak width as the number of depositions is increased, the trends observed are similar to those for the plot of peak height. The values are presented in Table 5.2 below. The number of dzBA layers was obtained by dividing the area from the dzBA films by the value for the

4-MBA film. Therefore, using 4-MBA as a monolayer model, the initial scans at 10 mVs^{-1} and 100 mVs^{-1} resulted in approximate monolayer and submonolayer amounts of benzoic acid respectively. Successive scanning resulted in continuous layer growth and an increase in surface density of benzoic acid. The films formed at 10 mVs^{-1} provided larger peak intensities compared to those at 100 mVs^{-1}. The surface selection rule involved with IRRAS does not permit a more conclusive statement on the differences in the films. However, AFM will provide more detailed information on film thickness and this will be discussed in conjunction with the IRRAS data in the next section.

Table 5.2. IRRAS carbonyl peak area for benzoic acid layers formed from electrochemical reduction of diazonium salt and self-assembly of 4-MBA. Experiments were repeated to obtain an estimate of the standard deviation.

# of Deposition Cycles	10 mVs^{-1}	# of Aryl Layers	100 mVs^{-1}	# of Aryl Layers	4-MBA
1	0.032	1.2 ± 0.4	0.010	0.4 ± 0.4	0.27 ± 0.008
2	0.097 ± 0.018	4 ± 1	0.046 ± 0.049	2 ± 2	
5	0.131 ± 0.002	5 ± 1	0.061 ± 0.028	2 ± 1	
10	0.162 ± 0.021	6 ± 2	0.091 ± 0.040	3 ± 2	

Atomic Force Microscopy (AFM). AFM ‘scratching’ experiments were performed to determine the thickness of the aryl films formed and determine the extent of multilayer formation. The validity of AFM ‘scratching’ experiments to determine the height of aryl layers deposited on solid surfaces has previously been shown.[23,24,42,43] Under appropriate conditions a force may be applied that is great enough to remove the adsorbed film but not damage the underlying substrate. Upon imaging a larger area of the surface, information may be obtained on the height difference between the intact adsorbed layer and the 'scratched' area where the film has been removed down to the underlying substrate.

For this work a 2 μm sided square was 'scratched' into electrochemically modified surfaces, removing the dzBA film. A 5 μm area was then imaged in tapping mode and the height difference was determined and attributed to the adsorbed aryl film. To ensure the difference recorded was a result of removal of the aryl film and not from damage to the gold substrate a control experiment using an unmodified gold surface was performed. Shown in Figure 5.07 (A) is the control image showing that the substrate was not altered with the forces applied during the 'scratching' of the aryl film. Shown in Figure 5.07 (B) is a representative image following 'scratching' of the aryl film and subsequent imaging in tapping mode. This procedure was repeated for all surfaces tested with the height difference determined at three locations on each surface. The results are listed in Table 5.3.

The height of the aryl films was used to determine the approximate number of layers present on the surface. The height of a benzoic acid molecule oriented perpendicular to the electrode surface was approximated at 0.7 nm. The data in Table 5.3 shows that the aryl film thickness increases as the number of deposition cycles increased. Furthermore, when the deposition is performed by scanning at 10 mVs^{-1}, thicker films are produced. This result is consistent with the IRRAS data showing larger band intensity for films formed at 10 mVs^{-1}. Table 5.4 provides a comparison between the approximate film thicknesses determined by IRRAS and AFM.

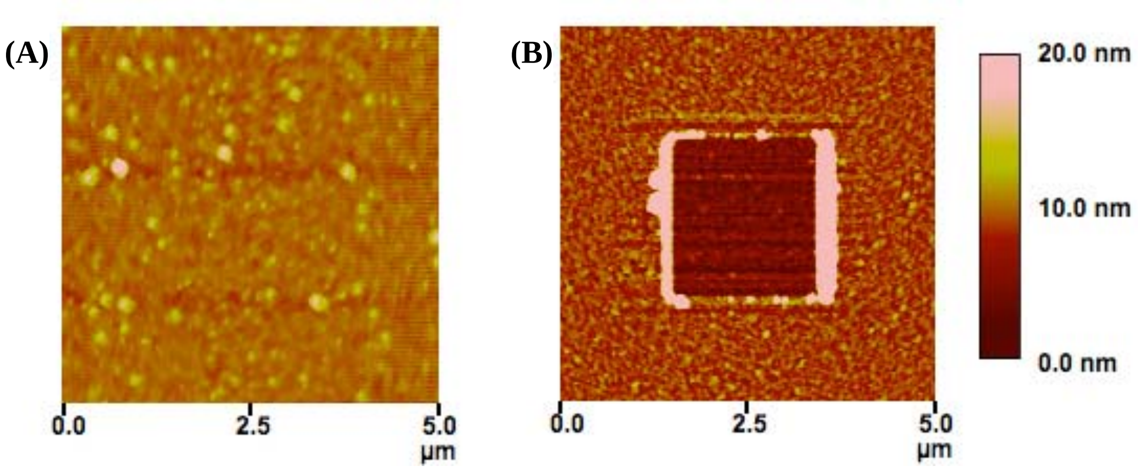

Figure 5.07. AFM tapping mode images of (A) unmodified gold surface and (B) surface modified with a 0.5 mM dzBA using 5 cycles at 10 mVs^{-1} following 'scratching' of the surfaces.

Table 5.3. Height of aryl films as determined using AFM 'scratching'.

# of Deposition Cycles	10 mVs^{-1}		100 mVs^{-1}	
	Film Height	**# of Aryl Layers**	**Film Height**	**# of Aryl Layers**
1	2.9 ± 0.1	4.1 ± 0.1	1.0 ± 0.2	1.4 ± 0.3
2	3.3 ± 0.4	4.7 ± 0.6	0.9 ± 0.4	1.3 ± 0.6
5	3.9 ± 0.2	5.6 ± 0.3	2.5 ± 0.2	3.6 ± 0.3
10	9.8 ± 0.3	14 ± 0.4	4.1 ± 0.2	5.9 ± 0.3

Table 5.4. Comparison of calculated dzBA film thickness using IRRAS and AFM.

# of Deposition Cycles	# of Layers - 10 mVs^{-1}		# of Layers - 100 mVs^{-1}	
	IRRAS[a]	AFM[b]	IRRAS[a]	AFM[b]
1	1.2 ± 0.4	4.1 ± 0.1	0.4 ± 0.4	1.4 ± 0.3
2	4 ± 1	4.7 ± 0.6	2 ± 2	1.3 ± 0.6
5	5 ± 1	5.6 ± 0.3	2 ± 1	3.6 ± 0.3
10	6 ± 2	14 ± 0.4	3 ± 2	5.9 ± 0.3

a. $\nu_{c=o}$ band area for dzBA divided by $\nu_{c=o}$ for 4-MBA

b. measured AFM film height divided by 0.7 nm (height of dzBA molecule)

Surface Plasmon Resonance (SPR) Imaging. The goal of the project was to develop and evaluate the usefulness of a surface formed by the electrochemical reduction of dzBA as a support for immunoassay studies with SPR imaging. Gold surfaces modified with mono- to multilayers of dzBA were prepared as previously noted and used for further functionalization. Also included was a surface modified with its thiol analogue (4-MBA) as a monolayer model. The surface functionalization is shown in Figure 5.08 and involved activation of the carboxylic acid groups that were then used for covalent immobilization of an antibody. The antibody solution was delivered to the surface using a four-channel PDMS microfluidic device, resulting in a surface with patterned lines of antibody. After a brief immobilization period the PDMS was removed, the array surface rinsed, and the surface deactivated with a solution of ethanolamine.

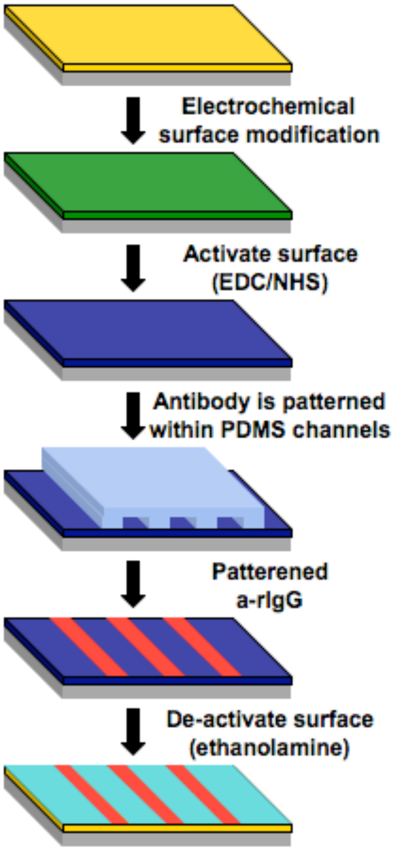

Figure 5.08. Surface preparation for antibody immobilization and subsequent surface passivation prior to introduction of antigen.

The performance of the antibody (a-rIgG) chips was evaluated by incubating them with antigen (rIgG). Shown in Figure 5.09 are difference images following the incubation of the antibody chips with an 1845 nM antigen solution. The images shown are representative of those for surfaces modified by the self-assembly of 4-MBA and the electrochemical reduction of dzBA at 10 mVs^{-1} and 100 mVs^{-1}. For all three surfaces the antigen binding was specific, with acceptable levels of non-specific binding observed to the ethanolamine de-activated surface between the channels (approximately 20% of total signal).

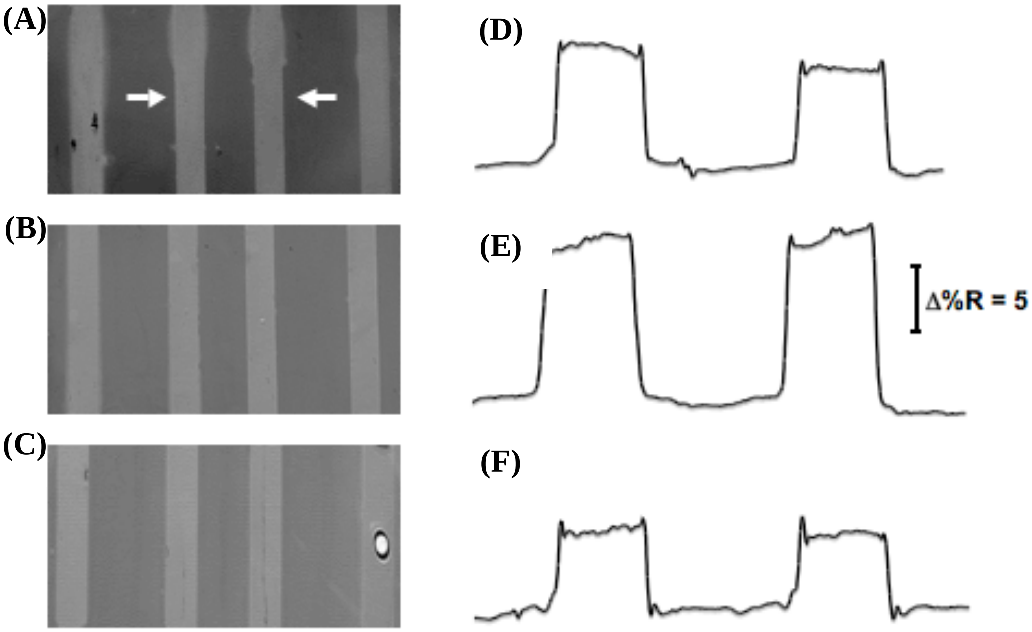

Figure 5.09. SPR difference images following incubation with an 1845 nM rIgG solution for antibody modified surfaces with an underlayer modified with a 0.5 mM dzBA at (A) 10 mVs^{-1} (B) 100 mVs^{-1} or (C) SAM of 4-MBA. Horizontal cross-sections for the surfaces are presented to the right of each image; (D) 10 mVs^{-1}, (E) 100 mVs^{-1}, (F) 4-MBA.

Binding curves were collected to investigate the impact of electrochemical deposition conditions used to pre-functionalize these antibody chips. The curves were analyzed as in other chapters using the four-parameter logistical equation (1).

$$\Delta\%R = \Delta\%R_{\min} + \frac{\Delta\%R_{\max} - \Delta\%R_{\min}}{1 + \left(\frac{[A]}{K_d}\right)^b} \qquad (1)$$

Antigen binding curves, and accompanying fitting parameters, for antibody immobilized to chips with the dzBA layers deposited at 10 mVs^{-1}, and a self-assembled 4-MBA layer, are shown in Figure 5.10 and Table 5.5. Comparison of the K_{ADS} values, a measure of the antibody-antigen interaction strength, show no significant differences, with values from 8 to 13 $x10^8$ M^{-1}. Examination of the $\Delta\%R_{max}$ values, a measure of the amount of antigen bound, does show a dependence on the underlying surface. When one electrochemical deposition cycle was used for surface modification, the antibody-dzBA chip bound approximately 1.6x less antigen than the 4-MBA-antibody chip. When the antibody was then immobilized to a surface formed with multiple dzBA deposition cycles, the amount of antigen bound increased 1.8x. These surfaces also bound 1.1x more antigen than the 4-MBA-antibody chip (monolayer model).

The antigen binding results above are likely related to the amount of benzoic acid electrochemically deposited on the surface. The addition of multiple dzBA deposition cycles increases the amount of benzoic acid deposited (IRRAS and AFM). The additional benzoic acid molecules likely increase the amount of antibody immobilized, and therefore, the amount of antigen bound. The fact that similar amounts of antigen was bound to the dzBA-antibody chips modified with two and five deposition cycles, suggest either that the additional benzoic acid molecules present in the layer formed with five cycles are not able to immobilize additional antibody or if increased antibody is present it is not able to bind antigen.

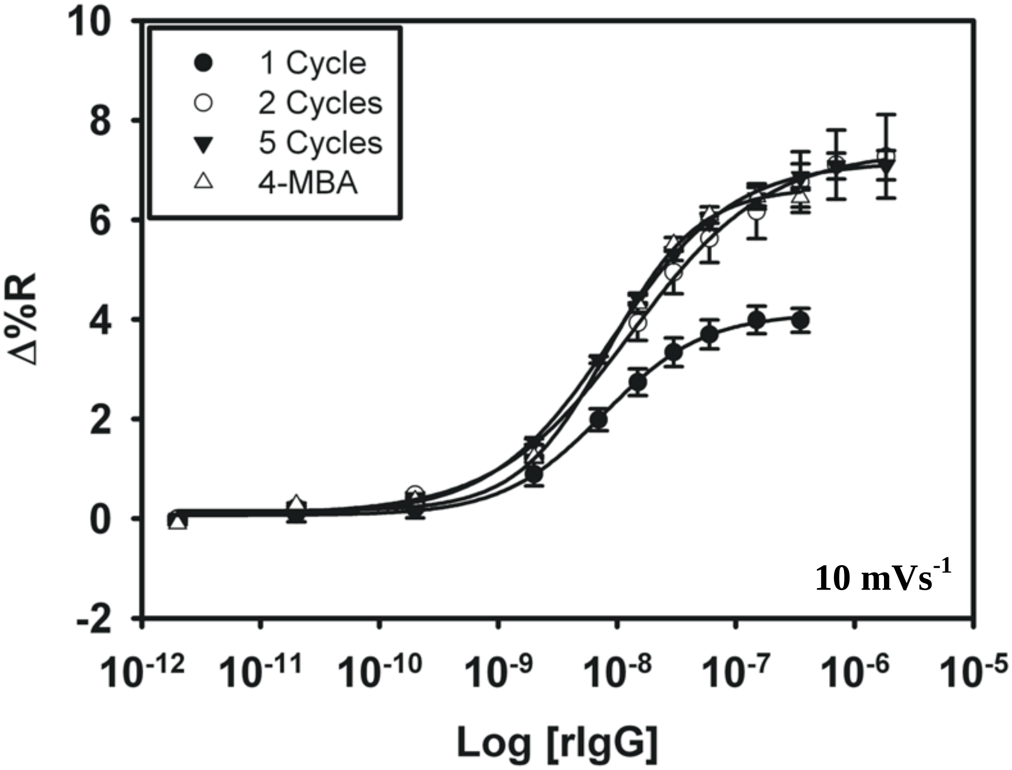

Figure 5.10. Antigen binding curves and fitting values (–) for antibody modified surfaces with an underlayer formed from the electrochemical deposition of a 0.5 mM dzBA; Scan rate = 10 mVs^{-1}. Included for comparison was an antibody modified surface with an underlayer of 4-MBA. Error bar represents the standard deviation of the measurement (n=4).

Table 5.5. Fitting parameters from least squares analysis using a four parameter logistical model. Errors represent deviations of the derived fit.

# of Cycles at 10 mVs^{-1}	R^2	K_{ADS} (M^{-1})	Min.	Max.	b
1	0.9994	13.0 ± 0.5 x10^8	-0.06 ± 0.06	4.46 ± 0.09	-0.83 ± 0.07
2	0.9987	7.5 ± 0.6 x10^8	-0.1 ± 0.2	11.0 ± 0.3	-0.62 ± 0.05
5	0.9995	10.9 ± 0.4 x10^8	0.04 ± 0.05	7.28 ± 0.07	-0.98 ± 0.05
4-MBA	0.9980	12 ± 1 x10^8	0.15 ± 0.08	6.7 ± 0.2	-1.2 ± 0.1

Studies were also performed on electrochemically deposited dzBA layers formed by scanning the potential at 100 mVs^{-1}. The antigen binding curves and fitting parameters are shown in Figure 5.11 and Table 5.6. As in the previous example, comparison of the K_{ADS} values suggests that the strength of the antibody-antigen interaction was similar on all surfaces. The amount of antigen captured on these dzBA-antibody chips, $\Delta\%R_{max}$, again showed a dependence on the number of deposition cycles used for surface modification. When one electrochemical deposition cycle was used for surface modification, the antibody-dzBA chip bound approximately 1.5x less antigen than the 4-MBA-antibody chip. The addition of a second dzBA deposition cycle prior to antibody immobilization, resulted in the binding of 2.5x more antigen, a value 1.6x larger than the 4-MBA-antibody chip. When the surface was modified with five deposition cycles, the amount of antigen captured by the dzBA-antibody chip was reduced by 1.5x relative to that of a dzBA-antibody chip formed with two deposition cycles.

Increasing the number of dzBA deposition cycles performed at 100 mVs^{-1}, from one to two, increased the amount of benzoic acid in the film. As in the results observed for films formed at 10 mVs^{-1}, the increased benzoic acid leads to greater amounts of immobilized antibody on the chip, and therefore, the antigen binding is increased. When five deposition cycles were used, the antigen binding capacity was reduced to levels observed for dzBA-antibody chips formed with multiple dzBA depositions at 10 mVs^{-1}. The decreased antigen binding, relative to that observed on the dzBA-antibody chip formed with 2 cycles at 100 mVs^{-1}, may be related to sterically hindered antigen binding. It has been shown in Chapter 2 and elsewhere,[44] that dense layers may not provide optimal binding, and that dilution of the surface immobilized probe may increase the binding capacity. Therefore, the surface density of immobilized antibody on the chip formed with two cycles at 100 mVs^{-1} may result in a more optimal density of surface immobilized antibody. This density reduces the steric hindrance, and increases the amount of antigen bound.

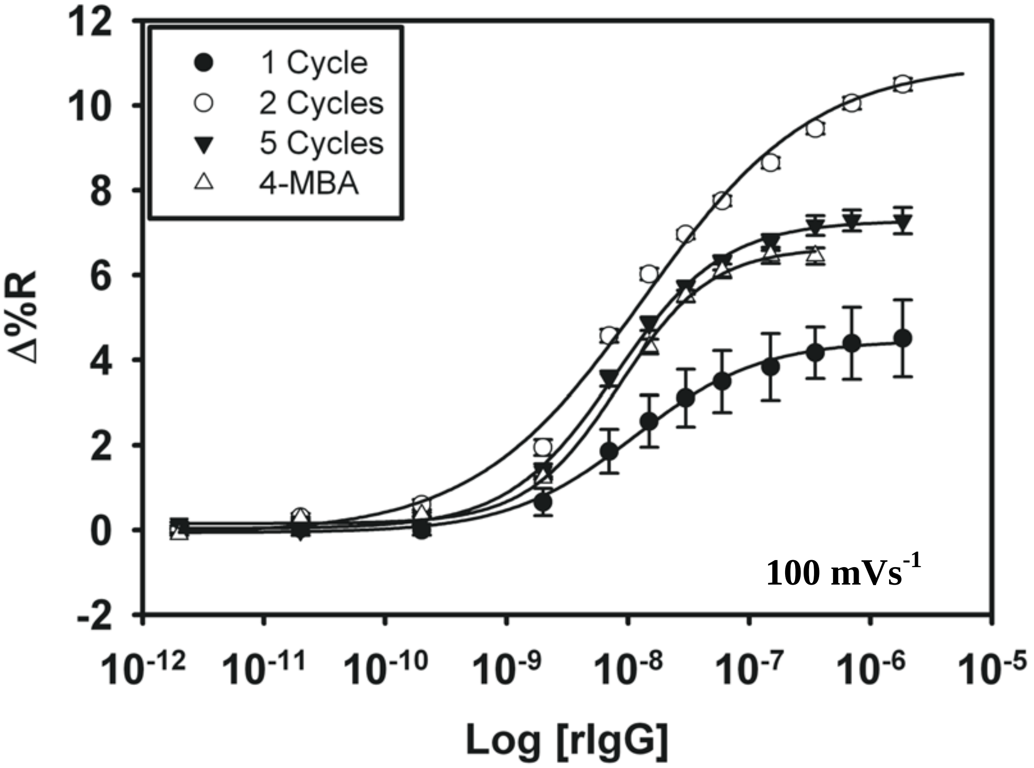

Figure 5.11. Antigen binding curves and fitting values (–) for antibody modified surfaces with an underlayer formed from the electrochemical deposition of a 0.5 mM dzBA; Scan rate = 100 mVs^{-1}. Included for comparison was an antibody modified surface with an underlayer of 4-MBA. Error bar represents the standard deviation of the measurement (n=4).

Table 5.6. Fitting parameters from least squares analysis using a four parameter logistical model. Deviations are errors from fitting parameters.

# of Cycles at 100 mVs^{-1}	**R^2**	**K$_{ADS}$ (M^{-1})**	**Min.**	**Max.**	**b**
1	0.9970	8.9 ± 0.8 x10^8	-0.06 ± 0.06	4.46 ± 0.09	-0.83 ± 0.07
2	0.9956	7 ± 1x10^8	-0.1 ± 0.2	11.0 ± 0.3	-0.62 ± 0.05
5	0.9989	12.7 ± 0.6 x10^8	0.04 ± 0.05	7.28 ± 0.07	-0.98 ± 0.05
4-MBA	0.9980	12 ± 1x10^8	0.15 ± 0.08	6.7 ± 0.2	-1.2 ± 0.1

The work presented in this chapter indicates that dzBA films provide a viable surface chemistry for antibody immobilization and as an immunoassay support. The electrochemical deposition conditions used for dzBA film formation may be used to control the density of the adsorbed films, and therefore, the antigen binding capacity.

5.4 CONCLUSIONS

The ability to electrochemically control the extent of surface coverage and multilayer formation of a dzBA film was shown. The use of these layers as immunoassay supports was evaluated through the covalent attachment of an antibody and the determination of specific and non-specific antigen binding. These surfaces were shown to exhibit large amounts of specific binding with minimal non-specific binding observed. Furthermore, the impact of surface coverage and multilayer formation of the aryl layers on immunoassay performance was evaluated. It was shown that the ideal immunoassay surface for antigen capture was an approximate monolayer of benzoic acid with covalently bound antibody.

5.5 REFERENCES

(1) Nuzzo, R. G.; Allara, D. L. *J. Am. Chem. Soc.* **1983**, *105*, 4481-4483.

(2) Ladd, J.; Taylor, A. D.; Piliarik, M.; Homola, J.; Jiang, S. *Anal. Chem.* **2008**, *80*, 4231-4236.

(3) Narayanan, R.; Lipert, R. J.; Porter, M. D. *Anal. Chem.* **2008**, *80*, 2265-2271.

(4) Shamsipur, M.; Kazemi, S. H.; Alizadeh, A.; Mousavi, M. F.; Workentin, M. S. *J. Electroanal. Chem.* **2007**, *610*, 218-226.

(5) Kanda, V.; Kitov, P.; Bundle, D. R.; McDermott, M. T. *Anal. Chem.* **2005**, *77*, 7497-7504.

(6) Kanda, V.; Kariuki, J. K.; Harrison, D. J.; McDermott, M. T. *Anal. Chem.* **2004**, *76*, 7257-7262.

(7) Twardowski, M.; Nuzzo, R. G. *Langmuir* **2003**, *19*, 9781-9791.

(8) Niki, K.; Hardy, W. R.; Hill, M. G.; Li, H.; Sprinkle, J. R.; Margoliash, E.; Fujita, K.; Tanimura, R.; Nakamura, N.; Ohno, H.; Richards, J. H.; Gray, H. B. *J. Phys. Chem. B* **2003**, *107*, 9947-9949.

(9) Huang, E.; Satjapipat, M.; Han, S. B.; Zhou, F. M. *Langmuir* **2001**, *17*, 1215-1224.

(10) Dick, L. A.; Haes, A. J.; Van Duyne, R. P. *J. Phys. Chem. B* **2000**, *104*, 11752-11762.

(11) Zamborini, F. P.; Crooks, R. M. *Langmuir* **1998**, *14*, 3279-3286.

(12) Schoenfisch, M. H.; Pemberton, J. E. *J. Am. Chem. Soc.* **1998**, *120*, 4502-4513.

(13) Delamarche, E.; Michel, B.; Kang, H.; Gerber, C. *Langmuir* **1994**, *10*, 4103-4108.

(14) Beulen, M. W. J.; Kastenberg, M. I.; van Veggel, F.; Reinhoudt, D. N. *Langmuir* **1998**, *14*, 7463-7467.

(15) Weisshaar, D. E.; Walczak, M. M.; Porter, M. D. *Langmuir* **1993**, *9*, 323-329.

(16) Delamar, M.; Hitmi, R.; Pinson, J.; Saveant, J. M. *J. Am. Chem. Soc.* **1992**, *114*, 5883-5884.

(17) Bernard, M. C.; Chausse, A.; Cabet-Deliry, E.; Chehimi, M. M.; Pinson, J.; Podvorica, F.; Vautrin-Ul, C. *Chem. Mater.* **2003**, *15*, 3450-3462.

(18) Laforgue, A.; Addou, T.; Belanger, D. *Langmuir* **2005**, *21*, 6855-6865.

(19) Pinson, J.; Podvorica, F. *Chem. Soc. Rev.* **2005**, *34*, 429-439.

(20) Paulik, M. G.; Brooksby, P. A.; Abell, A. D.; Downard, A. J. *J. Phys. Chem. C* **2007**, *111*, 7808-7815.

(21) Liu, G. Z.; Bocking, T.; Gooding, J. J. *J. Electroanal. Chem.* **2007**, *600*, 335-344.

(22) Kariuki, J. K.; McDermott, M. T. *Langmuir* **2001**, *17*, 5947-5951.

(23) Brooksby, P. A.; Downard, A. J. *Langmuir* **2004**, *20*, 5038-5045.

(24) Anariba, F.; DuVall, S. H.; McCreery, R. L. *Anal. Chem.* **2003**, *75*, 3837-3844.

(25) Tian, H.; Bergren, A. J.; McCreery, R. L. *Appl. Spectros.* **2007**, *61*, 1246-1253.

(26) Liang, H. H.; Tian, H.; McCreery, R. L. *Appl. Spectros.* **2007**, *61*, 613-620.

(27) Fave, C.; Leroux, Y.; Trippe, G.; Randriamahazaka, H.; Noel, V.; Lacroix, J. C. *J. Am. Chem. Soc.* **2007**, *129*, 1890-+.

(28) Ronen Polsky, J. C. H. D. R. W. S. M. B. *Electroanalysis* **2008**, *20*, 671-679.

(29) Polsky, R.; Harper, J. C.; Wheeler, D. R.; Dirk, S. M.; Arango, D. C.; Brozik, S. M. *Biosens. Bioelectron.* **2008**, *23*, 757-764.

(30) Harper, J. C.; Polsky, R.; Wheeler, D. R.; Brozik, S. M. *Langmuir* **2008**, *24*, 2206-2211.

(31) Harper, J. C.; Polsky, R.; Wheeler, D. R.; Dirk, S. M.; Brozik, S. M. *Langmuir* **2007**, *23*, 8285-8287.

(32) Corgier, B. P.; Li, F.; Blum, L. J.; Marquette, C. A. *Langmuir* **2007**, *23*, 8619-8623.

(33) Corgier, B. P.; Laurent, A.; Perriat, P.; Blum, L. J.; Marquette, C. A. *Angew. Chem., Int. Ed.* **2007**, *46*, 4108-4110.

(34) Shabani, A.; Mak, A. W. H.; Gerges, I.; Cuccia, L. A.; Lawrence, M. F. *Talanta* **2006**, *70*, 615-623.

(35) Liu, G. Z.; Gooding, J. J. *Langmuir* **2006**, *22*, 7421-7430.

(36) Blankespoor, R.; Limoges, B.; Schollhorn, B.; Syssa-Magale, J. L.; Yazidi, D. *Langmuir* **2005**, *21*, 3362-3375.

(37) Bourdillon, C.; Delamar, M.; Demaille, C.; Hitmi, R.; Moiroux, J.; Pinson, J. *J. Electroanal. Chem.* **1992**, *336*, 113-123.

(38) Corgier, B. P.; Marquette, C. A.; Blum, L. J. *J. Am. Chem. Soc.* **2005**, *127*, 18328-18332.

(39) Starkey, E. B. *Organic Syntheses* **1939**, *19*, 40-42.

(40) Faulkner, A. J. B. a. L. R. *Electrochemical Methods: Fundamentals and Applications*; 2nd ed.; John Wiley and Sons, Inc.: New York, 2001.

(41) Donald L. Pavia, G. M. L., and George S. Kriz *Introduction to Spectroscopy*; Third ed.; Harcourt College Publishers: Philadelphia, 2001.

(42) Cruickshank, A. C.; Tan, E. S. Q.; Brooksby, P. A.; Downard, A. J. *Electrochem. Comm.* **2007**, *9*, 1456-1462.

(43) Brooksby, P. A.; Downard, A. J. *J. Phys. Chem. B* **2005**, *109*, 8791-8798.

(44) Spinke, J.; Liley, M.; Guder, H. J.; Angermaier, L.; Knoll, W. *Langmuir* **1993**, *9*, 1821-1825.

Chapter 6:

Conclusions and Future Work

6.1 CONCLUSIONS

The body of work presented discussed the impact of probe immobilization conditions on the performance of several solid phase immunoassays. Chapter 2 examined the density of an immobilized disaccharide and its ability to specifically capture antibody. It was shown that the antibody was able to specifically recognize one of the disaccharides from the three stereoisomers arrayed. Furthermore, the maximum antibody binding occurred to a dilute and macroscopically homogenous disaccharide layer. Spectroscopic analysis of the disaccharide surfaces formed from various solution mole percentages showed the layers were macroscopically homogeneous and the addition of a diluent molecule to the immobilization solution gave reasonable control over the surface density of the immobilized disaccharide.

Chapter 3 examined the impact of antibody immobilization schemes on immunoassay performance. Three methods were selected including physical adsorption, covalent attachment, and affinity capture. Experimental conditions for each of the attachment schemes were examined in an attempt to optimize conditions of each prior to comparison. It was then shown that a covalent attachment provides the most stable antibody attachment and permitted the detection of a 77 pM antigen solution, with previous literature values reported at 1-2 nM.[1]

Chapter 4 continued to push the detection limits by incorporating the covalent attachment of antibody and using a sandwich assay format with antibody modified gold nanoparticles as an enhanced immunoassay. The detection limits were again pushed lower, to approximately 4 pM. The source of the enhancement of the nanoparticle assay was examined and it was determined the enhancement was from the increased avidity of these antibody modified gold nanoparticles for the surface and their increased density when compared with an antibody alone. Electronic coupling between the particles and the gold film was not observed.

Finally, Chapter 5 examined a novel surface chemistry for surface plasmon resonance (SPR) imaging assays. The electrochemical reduction of a diazonium salt to a thin gold film was evaluated as a surface chemistry for antibody immobilization and subsequent antigen detection. It was shown that the surface chemistry provided a suitable platform for antibody attachment and use as an antibody chip for antigen detection. Also, the electrochemical deposition conditions may be used to control the diazonium layer formed and the sensitivity of the antibody chip.

6.2 FUTURE WORK

Immunodiagnostics is a large and growing field with potential interest in the ability to generate a high throughput array that incorporates label-free detection. The realization of an immunodiagnostic microarray would greatly reduce the time required for current analysis by combining multiple clinical tests onto a single microarray. Rather than performing multiple tests on an individual sample, multiple analyses would be performed in a single experiment. The success of this array would result in reduced analysis times and improved patient care.

I propose the development of a diagnostic microarray capable of performing multiple clinically relevant diagnostic tests on a patient's blood sample. The tests incorporated on the surface of the microarray would include the forward and reverse determination of an individual's blood type as well as screening for the presence of disease. The array would be patterned onto a gold substrate to allow for the label-free reading of the array using SPR imaging.

The determination of an individual's blood type and the diagnostic screening for the presence of potentially harmful disease is a multi-billion dollar industry.[2] The ABO blood type was discovered in 1901 by Karl Landsteiner, for which he earned the Nobel Prize in medicine in 1930.[3] An individual's blood is composed of red-blood cells (RBCs), white blood cells, and platelets, which are distributed in a fluid known as plasma.[4] The plasma also contains salts and vast numbers of proteins, including antibodies. The surface of the RBC contains blood group specific antigens, which determine an individuals ABO classification.[5] There are four types including A, B, AB, and O. A further classification is for the presence of a Rhesus factor (Rh) protein, which if present or absent is indicated with a + or - after the blood type. In addition to the presence of antigens on an RBCs surface, we also carry the non-complementary blood group specific antibodies (IgM's) in our plasma.[5] For example, a type A+ individual would have the A antigen and the Rh protein on the RBC cell surface and anti-B IgM antibodies in their plasma.

The determination of an individual's blood type consists of two tests, known as a forward and reverse type. A forward type is used to determine the type of antigens present on the surface of the RBCs and a reverse type determines the type of blood group specific antibodies present in the plasma. The incorporation of both tests serves as a check to ensure agreement between the tests and reduce errors associated with incorrectly typed blood.

The adaptation of forward and reverse typing to a microarray platform would require the surface immobilization of the blood type specific IgM antibodies (anti-A, anti-B, and anti-D) and the trisaccharide antigens (A and B). The work in Chapter 3 optimizing antibody attachment will serve as a starting point for the immobilization of IgM molecules. The reverse type requires the immobilization of the A and B antigens. These antigens are similar trisaccharides with the A antigen containing an N-acetyl group compared with an –OH group for the type B antigen.[5] The experience gained in Chapter 2 would provide valuable information on the ability to tailor probe/trisaccharide density for optimal binding. The immobilization chemistry is not expected to be a major challenge in this work. In fact, SPR has been used for the detection and typing of human erythrocytes[6,7] and also for the detection of antibodies in serum[8-12] and plasma.[13] These examples provide merit to the potential for SPR as a viable detection technique. While this initial work has been done, the incorporation of an array format and the integration of multiple analyses on a single chip have not yet been attempted.

A major challenge of this project will stem from the complexity of the sample matrix. As mentioned above, blood is composed of several types of large cells and a cocktail of proteins. The RBCs to be detected in forward typing are approximately 4-6 μm wide and large enough that potential diffusion problems may exist. The flow-rate employed in the work will likely be more crucial than with other examples. However, the binding of bacteria cells using SPR imaging has been successfully done in our lab.[14] The challenge of controlling non-specific adsorption is one of great concern with many examples and potential solutions in the literature.[15-27] Diluting the blood prior to analysis will reduce the total protein concentration and assist in reducing the potential for non-specific adsorption. A consequence of this is that the analytes of interest will also be diluted. Therefore, the work improving detection limits and sensitivity in Chapter 3 and 4 will be of use. If a sandwich assay, like the ones shown in Chapter 4, is used this may further assist in reducing the non-specific binding while also provided an enhanced signal.

If initial attempts performing a parallel forward and reverse type on a single microarray using SPR imaging are successful, the next challenge will be to expand the detection from blood typing to diagnostics. The ability to perform blood typing and screen for diseases such as hepatitis B or human immunodeficiency virus (HIV) would significantly streamline current blood screening technology. These challenges would be great as serological markers for hepatitis B alone include the detection of up to six different proteins.[28]

A final hurdle to be addressed before this microarray technology will be considered for clinical testing will be the concerns over reproducibility in microarray technology. Almost fifteen years after the first microarrays began to appear there still remain concerns over the reproducibility of this technique.[29,30] Efforts are currently underway to address these issues and bring microarray technology to clinical research labs. In February of 2005 the Food and Drug Administration (FDA) led Microarray Quality Control (MAQC) project began.[29] The project is a widespread collaboration geared to assess the technical performance of microarrays and the capabilities and limitations of microarray data analysis methods. The completion of the MAQC project should bring the incorporation of microarray technology into clinical testing laboratories closer to a reality.

The development of a label-free microarray for parallel determination of blood group and diagnostic screening for the presence of disease in a blood sample will require significant efforts to complete, however, the potential rewards are equally significant. The work presented in this thesis provides a valuable starting point for the optimization of both antibodies and carbohydrates required for the surface patterning of the microarray. Also, the improved sensitivity and detection limits that were achieved may assist in detecting low levels of antibody and antigens present in a patient’s serum.

6.3 REFERENCES

(1) Cao, C.; Sim, S. J. *Biosens. Bioelectron.* **2007**, *22*, 1874-1880.

(2) www.okokok.com.cn/datareport/class151/200511/50469.html. **2005**.

(3) www.nobelprize.org/educational_games/medicine/landsteiner/readmore.html. **2001**.

(4) www.wikipedia.org/wiki/blood. **2009**.

(5) Harmening, D. M. *Modern Blood Banking and Transfusion Practices*; 5th ed.; F.A. Davis Company: Philadelphia, 2005.

(6) Li, B. X.; Chen, J.; Long, M. *Chin. Sci. Bull.* **2008**, *53*, 3634-3641.

(7) Quinn, J. G.; O'Kennedy, R.; Smyth, M.; Moulds, J.; Frame, T. *J. Immunol. Meth.* **1997**, *206*, 87-96.

(8) Mytych, D. T.; La, S.; Barger, T.; Ferbas, J.; Swanson, S. J. *J. Pharmaceut. Biomed. Anal.* **2009**, *49*, 415-426.

(9) Ladd, J.; Taylor, A. D.; Piliarik, M.; Homola, J.; Jiang, S. Y. *Anal. Bioanal. Chem.* **2009**, *393*, 1157-1163.

(10) Su, F.; Xu, C.; Taya, M.; Murayama, K.; Shinohara, Y.; Nishimura, S. I. *Sensors* **2008**, *8*, 4282-4295.

(11) de Boer, A. R.; Hokke, C. H.; Deelder, A. M.; Wuhrer, M. *Glycoconjugate J* **2008**, *25*, 75-84.

(12) Carlsson, J.; Gullstrand, C.; Westermark, G. T.; Ludvigsson, J.; Enander, K.; Liedberg, B. *Biosens. Bioelectron.* **2008**, *24*, 876-881.

(13) Vaisocherova, H.; Yang, W.; Zhang, Z.; Cao, Z. Q.; Cheng, G.; Piliarik, M.; Homola, J.; Jiang, S. Y. *Anal. Chem.* **2008**, *80*, 7894-7901.

(14) Shang, H. PhD, University of Alberta, 2008.

(15) Charles, P. T.; Stubbs, V. R.; Soto, C. M.; Martin, B. D.; White, B. J.; Taitt, C. R. *Sensors* **2009**, *9*, 645-655.

(16) Fernandez, C. A.; Wiacek, R. J.; Nachimuthu, P.; Fryxell, G. E.; Pierson, A. M.; Warner, C. L.; Warner, M. G.; Addleman, R. S. *J. Nanosci. Nanotechnol.* **2008**, *8*, 5781-5786.

(17) Kim, W. S.; Nishizawa, T.; Yoshimizu, M. *Diseases of Aquatic Organisms* **2007**, *78*, 55-59.

(18) Zuo, G. M.; Li, X. X.; Zhang, Z. X.; Yang, T. T.; Wang, Y. L.; Cheng, Z. X.; Feng, S. L. *Nanotechnology* **2007**, *18*.

(19) Matsuura, K.; Ohno, K.; Kagaya, S.; Kitano, H. *Macromol. Chem. Phys.* **2007**, *208*, 862-873.

(20) Cole, M. A.; Thissen, H.; Losic, D.; Voelcker, N. H. *Surf. Sci.* **2007**, *601*, 1716-1725.

(21) Kitano, H.; Gemmei-Ide, M.; Anraku, Y.; Saruwatari, Y. *Colloids and Surfaces B-Biointerfaces* **2007**, *56*, 188-196.

(22) Beyer, M.; Felgenhauer, T.; Bischoff, F. R.; Breitling, F.; Stadler, V. *Biomaterials* **2006**, *27*, 3505-3514.

(23) Kurita, R.; Hirata, Y.; Yabuki, S.; Kato, D.; Sato, Y.; Mizutani, F.; Niwa, O. *Electrochemistry* **2006**, *74*, 121-124.

(24) Hoffmann, C.; Tovar, G. E. M. *J. Colloid Interface Sci.* **2006**, *295*, 427-435.

(25) Rebeski, D. E.; Winger, E. M.; Shin, Y. K.; Lelenta, M.; Robinson, M. M.; Varecka, R.; Crowther, J. R. *J. Immunol. Meth.* **1999**, *226*, 85-92.

(26) Zhang, P.; Wu, J. T. *Clin. Chem.* **1997**, *43*, 604-604.

(27) Ahluwalia, A.; Giusto, G.; DeRossi, D. *Mater. Sci. Eng. C* **1995**, *3*, 267-271.

(28) www.cdc.gov/hepatitis/HBV/HBVfaq.htm#overview. **2008**.

(29) Shi, L.; Perkins, R. G.; Fang, H.; Tong, W. *Curr. Opin. Biotechnol.* **2008**, *19*, 10-18.

(30) Draghici, S.; Khatri, P.; Eklund, A.; Szallasi, Z. *TRENDS in Genetics* **2006**, *22*, 101-109.